

**Closed-loop experiments
to investigate spatial contrast
integration in the retina**

DISSERTATION

DER FAKULTÄT FÜR BIOLOGIE
DER LUDWIG-MAXIMILIANS-UNIVERSITÄT
MÜNCHEN
ZUR ERLANGUNG DES AKADEMISCHEN GRADES
DOCTOR RERUM NATURALIUM
(DR. RER. NAT)

ANGEFERTIGT AM
MAX-PLANCK-INSTITUT FÜR NEUROBIOLOGIE
UND AM
BERNSTEIN CENTER FOR COMPUTATIONAL NEUROSCIENCE
MÜNCHEN

vorgelegt von

Herrn Dipl.-Phys. Daniel Bölinger

geboren am 30. Mai 1983 in Trier

München, im November 2011

<i>Betreuer:</i>	Herr Prof. Dr. Tim Gollisch
<i>Erster Gutachter:</i>	Herr Prof. Dr. Alexander Borst
<i>Zweiter Gutachter:</i>	Herr Prof. Dr. Rainer Uhl
<i>Eingereicht am:</i>	24. November 2011
<i>Tag der mündlichen Prüfung:</i>	31. Januar 2012

*Sometimes these eyes
Forget the face they're peering from
When the face they peer upon
Well, you know
That face as I do
And how in the return of the gaze
She can return you the face
That you are staring from*

Franz Ferdinand (Jacqueline)

CONTENTS

Overview	1
1 The Vertebrate Retina	5
1.1 Biological and Functional Description	5
1.2 Receptive Fields and Center-Surround Antagonism	10
1.3 Retinal Adaptation	12
1.4 Spatial Nonlinearities in Ganglion Cell Receptive Fields	13
1.5 Computational Models	15
2 Experimental Procedures	19
2.1 Tissue Preparation and Sustainment	19
2.2 Electrophysiology	20
2.3 Visual Stimulation	22
2.4 Closed-Loop Experiments	23
3 Methods for Assessing Nonlinearities in RGC	27
3.1 X- and Y- cell Analysis	29
3.2 Spike-Triggered Systems Analysis	31
3.3 The Iso-Response Method	36
3.4 Closed-Loop Determination of Iso-response Stimuli	42
4 Integration in the Receptive Field Center	47

4.1	Spatial Integration Is Nonlinear	48
4.2	Spatial Scale of Nonlinearities	52
4.3	Spike Patterns along Iso-Response Curves	56
4.4	Mechanisms of Local Gain Control	58
4.5	Functional Consequences for Stimulus Integration	63
4.6	Spatial Integration in Different Cell Types and Species	64
4.7	Iso-Response Results in Higher Dimensions	66
5	Center-Surround Integration	69
5.1	Center-Surround Integration is Nonlinear	72
5.2	Spike Patterns along Iso-Rate Curves	78
5.3	Computational Models of Center-Surround Integration	80
5.4	Surround Antagonism is Mediated by Inhibitory Neurotransmitters	83
5.5	Center-Surround Structure of Homogeneity Detectors	83
6	Summary & Discussion	85
6.1	Benefits of Iso-Response Measurements	86
6.2	Nonlinear Spatial Integration in the Receptive Field Center	89
6.3	Nonlinear Center-Surround Integration	91
6.4	Temporal Information in RGC Responses	94
	Outlook	95
	Appendices	99
A	Horizontal Cell Inherited Surround Antagonism	99
B	Eigenvalues of the STC Matrix	101
C	STC Analysis of a Model Neuron	102
D	Scale Invariance of Iso-Response Curves	104

E	Simulation of Response Linearization	106
F	Synaptic Depression Model	108
G	Shunting Inhibition of Narrow-Field Amacrine Cells	111
H	Divisive or Subtractive Inhibition Leads to Identical Iso-Response Curves . . .	113
I	Linearity of Center-Surround Iso-Rate Curves	115
J	Supplementary Methods	116

Bibliography	123
---------------------	------------

Figure Acknowledgments	137
-------------------------------	------------

ACKNOWLEDGMENTS

I am truly grateful to the many people who supported me while I was working on this dissertation. First of all I want to thank Tim Gollisch for giving me the possibility to work in his group. He taught me about the fascinating world of neuroscience and always patiently answered my scientific and non-scientific questions. Besides, he encouraged me to visit summer schools and conferences around the world, and definitely enhanced my presentation skills.

Special thanks to every single member of the Visual Coding Group, both at the Max Planck Institute of Neurobiology and at the University Medical Center Göttingen. Christian Mendl was always helpful with all mathematical and programming problems. Vidhyasankar Krishnamoorthy happily shared his knowledge about the retina and the newest literature. I discussed many things in and around science with Mona Garvert. Fernando Rozenblit, Garrett Greene, Jian Liu, Michael Weick, and Norma Kühn supported me in the last few weeks of thesis writing and provided invaluable feedback on my work. For the same reason I am grateful to Daisuke Takeshita, who also supplied me with the best tips on where to eat Ramen.

Moreover, I want to thank Alexander Borst for the formal supervision of my dissertation and the insightful discussions on various retreats and in his office. In the same vein, I want to thank Günther Zeck and Jan Benda, the two members of my Thesis Advisory Committee for their supporting ideas regarding my research.

A special thank goes to Andreas Herz. This is not only for providing me office space in his research group during the last six month of my PhD, but in particular for being the driving force behind the Bernstein Center for Computational Neuroscience München.

Last but not least, I want to thank all the people who shared the ups and downs of my private life during the last three years. Many thanks to my parents for their ongoing support, and of course to my brother and my sister. I am very grateful to my girlfriend Ines Voth who was always patient, helpful, and indispensable for keeping me motivated. Finally, I want to thank Sandro Casagrande for proofreading and Jan Klemmer for Käsefondue.

OVERVIEW

The fundamental goal of all neuronal processing is to make optimal decisions, and thereby to generate optimal behavior. To this end, the brain performs at each point in time millions of parallel computations. Right now, your brain might weigh thoroughly if it is worth to continue reading this thesis or not. In the end however, weighing is not enough: a decision has to be made. Such a decision is an intrinsically nonlinear process. If two possibilities are nearly equally evaluated, a small change in your considerations might lead to the acceptance of one alternative, and the rejection of the other. Furthermore, not all considerations have to contribute linearly to the decision. For example, a lack of time might certainly keep you from reading this thesis, while having excess spare time might still not make you read it. Such a nonlinear weighing of considerations does not only occur on the conscious level, but all the time in the individual neuronal circuits of the brain. Each neuron can be interpreted as a decision unit, computing whether to spike or not. It typically receives multiple parallel streams of information, and based on these generates its own neuronal output. The inputs resemble the considerations taken into account, while the output conveys the decision to subsequent circuits. How the decision is made is therefore determined by the way the inputs are combined into the neuronal output. In particular, individual inputs might contribute either linearly or nonlinearly to the decision. Thus, in order to understand which role a neuron plays in information processing, we have to assess the nonlinearities involved in the integration of different neuronal inputs.

In this thesis, we study this ubiquitous signal integration in the output neurons of the amphibian retina, the retinal ganglion cells. Thereby we hope to gain a better understanding of the general mechanisms underlying signal integration in the circuits of the brain. This will also help us elucidate the functions of the retina in particular. Because of the high similarity of the retinas among all vertebrates (Dowling and Dubin 2011), by studying the amphibian retina we also learn to better understand human vision.

The amphibian retina is particularly suited to study the nonlinear integration of neuronal signals, because each single ganglion cell receives distinct inputs originating from tens to hundreds of photoreceptors (Wässle 2004, Gollisch and Meister 2010). Indeed, ganglion cells do

not just linearly average these inputs, but combine them in a nonlinear fashion (Enroth-Cugell and Robson 1966). It turned out that it is precisely this nonlinearity which allows specific ganglion cells to *decide* whether particular features were present in their visual input (Gollisch and Meister 2010, Ölveczky et al. 2003, Ishikane et al. 2005, Münch et al. 2009). Hence, an understanding of how the retina encodes images into neuronal activity requires an understanding of how the spatially distinct light stimuli, that each cell experiences, are combined into the output of this very cell. This is the question of *spatial integration* which we address in the following.

Many facts about this question are already available on a cellular level. Today we know which cell types mediate the signals from the photoreceptors to the ganglion cell, and we know much about the connections between the involved cells (Wässle 2004). Furthermore, in recent studies the transmission functions of some of the involved circuit elements (Singer 2007) were measured. In particular, it turned out that many of the processing steps are highly nonlinear. Although all these details are known, a detailed phenomenological description of spatial integration is still lacking (Schwartz and Rieke 2011). Most current models assume a linear integration (Field and Chichilnisky 2007), and thereby simply neglect the nonlinearities occurring on the cellular level. In this thesis, we attempt to fill the gap and strive for a functional characterization of spatial integration, and in particular of the involved nonlinearities.

We pursued the investigation by performing electrophysiological experiments on retinal ganglion cells. In particular, we measured the neuronal output with an array of electrodes (Meister et al. 1994). While measuring, we presented videos containing well-defined light stimuli to the retina. We performed the experiments in a closed-loop approach which allowed us to assess the neuronal response online and use the results to determine the subsequently shown stimuli.

The visual area, over which a ganglion cell pools its input, is called the receptive field of the cell. It has been known for almost 60 years that the receptive fields of many ganglion cells are organized in a center-surround structure (Kuffler 1953). In the receptive field center, the cell is most sensitive to visual stimulation. Depending on the cell, it preferentially responds to either a brightening (ON cell) or a darkening (OFF cell) of the image. In contrast, the response in the receptive field surround is weaker, and it is of opposite sign than the center response. Taking this structural segregation of the receptive field into account, we divided our experiments into two parts. First, we determined how different stimuli are combined within the receptive field center. Afterwards, we focused on the integration of stimuli in the center and the surround.

Throughout this thesis, we used a specific approach to study spatial integration. This approach is the measurement of so-called iso-response stimuli (Gollisch et al. 2002, Gollisch and Herz 2005, Benda et al. 2007). Instead of showing predefined stimuli and measuring the neuronal outputs, we did the experiments the other way round: we predefined the output, and then

searched for those stimuli which yielded the chosen response. The result of such a measurement was a set of stimuli which all triggered the same neuronal response in a given ganglion cell. Thereby, the cell's response was either defined as the number of elicited spikes (iso-rate stimuli), or the first-spike latency (iso-latency stimuli). Iso-response stimuli allowed us to directly assess the nonlinearities involved in signal integration in retinal ganglion cells.

The thesis is organized in six chapters.

The *first chapter* summarizes the important facts and figures about the vertebrate retina. At the beginning, the morphology is described; all the cell types are briefly discussed. Afterwards, we describe the center-surround structure of retinal ganglion cells in more detail and the pathways which are involved in generating it. Then the mechanisms of retinal adaptation are discussed. This lays the foundation for the results in chapter four, where we report the finding of a novel mechanism that rapidly adjusts the gain of local contrasts. Furthermore, we give an overview on what is already known about the nonlinearities underlying spatial integration. At the end of the chapter, the commonly used computational models of retinal processing are introduced.

The electrophysiological experiments are described in *chapter two*. We will explain in detail how the retina preparation was performed and how we recorded from ganglion cells while simultaneously showing visual stimuli. Importantly, the closed-loop setup is introduced. This experimental setup allowed us to measure iso-response stimuli in an automated fashion.

In the *third chapter*, different methods for the investigation of spatial integration are introduced. We start historically with the experiments that led to the discovery of linear and nonlinear integrating cells in the cat retina. Afterwards, we introduce the techniques of spike-triggered systems analysis. Because both methods suffer from certain disadvantages, we will then introduce the iso-response approach. We will explain how this method can be used to investigate the nonlinear processing in ganglion cell receptive fields, and which benefits the method has. Finally, we will describe how the closed-loop experiments were applied to measure iso-response stimuli.

Chapter four is the first results chapter of this thesis. Data from salamander and frog OFF ganglion cells are presented. We here attempt to determine a functional description of spatial integration in the receptive field center. The underlying hypothesis was that the receptive field center comprises multiple spatially distinct subunits which linearly pool their respective inputs. Subsequently, the subunits may perform a nonlinear signal transformation on their individual outputs before the latter are summed by the ganglion cell. The goal was to determine this subunit nonlinearity and to measure the receptive field sizes of the subunits. It turned out that the cells' responses could indeed be very well described in this model. We found evidence that subunits correspond to individual bipolar cells, which impose roughly rectifying-

quadratic nonlinearities on their output. Functionally, this nonlinearity rendered the majority of cells sensitive to small high-contrast stimuli within the receptive field center. Surprisingly, we found one ganglion cell type which displayed a particular sensitivity to large low-contrast stimuli. Apparently, different types of retinal ganglion cells perform the integration of spatial signals differently, even in an opposite fashion. Thereby they provide complementary information about the stimulus for the brain. The iso-response method proved to be very suited to disentangle these two types of nonlinear integration and also allowed us to study the underlying neuronal circuit: we discovered that the cells that are sensitive to large low-contrast stimuli had an additional mechanism which dynamically down-regulated the gain of strong local signals. Thus, the number of generated spikes was reduced while the latency remained unaffected. Furthermore, we could show that this gain control crucially depends on inhibitory neurotransmitters and is most likely mediated by narrow-field amacrine cells.

In *chapter five*, we investigated how stimuli in the receptive field surround affected stimuli shown simultaneously in the center. We hypothesized that the signals in both center and surround are nonlinearly transformed and subsequently integrated. Indeed this holds true: the surround signals appeared to be derived by roughly the same nonlinearity which determined the signal transformation in the center. Interestingly, the latency response was affected by the surround in an opposite fashion than the spike count: the latency was determined by excitatory signals from the surround. Hence, no suppressive center-surround structure exists in terms of latency. In contrast, the number of spikes was determined by inhibitory signals generated in the surround. The result was a strong response suppression if the surround was stimulated with dark contrasts. However, if the stimulation became strong enough, the surround unexpectedly enhanced its capability to generate action potentials. This led to responses which had a distinguished double-peaked temporal profile. The data seemed to be most congruent to a model in which rectifying-quadratic bipolar cells in center and surround excite the ganglion cell as well as linear amacrine cells. The latter in turn inhibit the ganglion cell. If we include an additional rebound excitation mechanism, the model can robustly explain the measured effects.

In *chapter six*, we summarize and discuss the obtained results. Especially, the advantages of the iso-response method will be presented.

Many more studies which could be performed using closed-loop experiments and the iso-response approach are proposed in the *outlook*. We believe that this method can lead to interesting results in a vast number of systems. In the *appendices* we discuss some additional results which are of minor relevance for the overall story of the thesis, and some technical details are presented.

Parts of the text and figures in this thesis will also be published (Bölinger and Gollisch 2011a,b).

1. THE VERTEBRATE RETINA

In this introductory chapter, we will provide the basis for the research performed for my PhD thesis project. The most important morphological and functional aspects of the vertebrate retina will be summarized. A detailed overview is given about the aspects of center-surround antagonism, retinal adaptation and spatial integration. These will be the topics that are addressed in chapter 4 and 5 of this thesis. Furthermore, the standard computational models of retinal processing are introduced.

1.1 BIOLOGICAL AND FUNCTIONAL DESCRIPTION

Visual perception is the dominant sensory cue for many creatures. Interestingly, the involved visual system of the brain has evolved to a comparable structure in a broad variety of species, ranging from flies to humans (Sanes and Zipursky 2010, Borst and Euler 2011). Among vertebrates, the anatomy of the eye is very similar (Fig. 1.1). Incoming light is focused by a lens and projected onto the backside of the eye. There it passes through the mostly transparent retina, in which it is detected and translated into a neuronal signal. The photoreceptor layer of the retina, where light-detection takes place, is attached to the pigment epithelium. The output signals generated by the retina are transmitted to subsequent visual areas via the optic nerve. Today we know that these output signals are much more than a spatially discretized representation of the visual input. The retina performs sophisticated computations, such as a dissection of background and object motion (Ölveczky et al. 2003), or a detection of approaching "predators" (Ishikane et al. 2005, Münch et al. 2009). Hence, the output signals consist of *features* of the input image, rather than of the raw data. By this feature extraction, the retinal network reduces redundancies in the input and thus performs a data compression. Such a compression is crucial because the optic nerve provides only a very limited bandwidth, much less than necessary to transmit the output of each present photoreceptor individually.

To perform such processing of the visual input, the retina consists of a neural network which comprises six major cell classes (Fig. 1.2) which are arranged in a layered structure (Masland 2001, Wässle 2004). In the outer layer, the light-receiving photoreceptors are located. Two

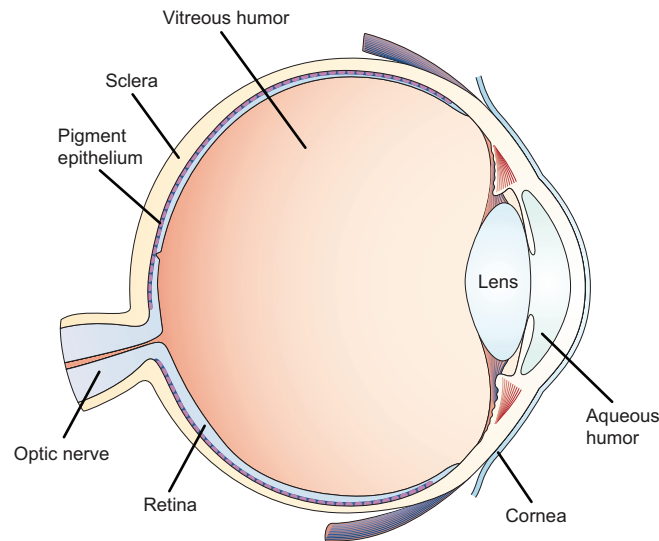


Figure 1.1: The eye in cross section. Adapted from Martinez-Conde et al. (2004).

types can be distinguished: cones (1), providing the visual function during daylight conditions, and rods (2), responsible for vision during night-time. The latter ones constitute the vast majority of photoreceptors and have the capability to detect even single photons. Cones can be further classified based on the spectral frequency band they are sensitive to (Masland 2001).

In the so-called outer plexiform layer (OPL), the photoreceptors make synaptic contact to horizontal cells (3) and bipolar cells (4). The neurotransmitter released by rods and cones is glutamate. Because photoreceptors respond to light with a graded hyperpolarization, the transmitter release is *reduced* by a light stimulus.

Bipolar cells have their cell bodies in the inner nucleus layer (INL). They can be classified into three major categories. Rod ON bipolar cells are connected to rods and gradually hyperpolarize in response to glutamatergic input. Thus they are excited by bright stimuli. Cone ON bipolar cells are the equivalent cells which are connected to cones. In contrast, cone OFF bipolar cells are excited by dark stimuli because they gradually depolarize in response to glutamatergic input from cones. Rod OFF bipolar cells do not exist in the vertebrate retina. Depolarizing stimuli are also called preferred stimuli, i.e. bright stimuli for ON cells and dark stimuli for OFF cells. In the inner plexiform layer (IPL), bipolar cell terminals make contacts with amacrine cells (5) and ganglion cells (6) via glutamatergic synapses (Masland 2001, Wässle 2004). Depending on the category of the bipolar cell, the synapses are formed in different sublayers of the IPL: while OFF bipolar cells establish synapses close to the border to the INL, ON bipolar cells stratify close to the ganglion cell layer (GCL).

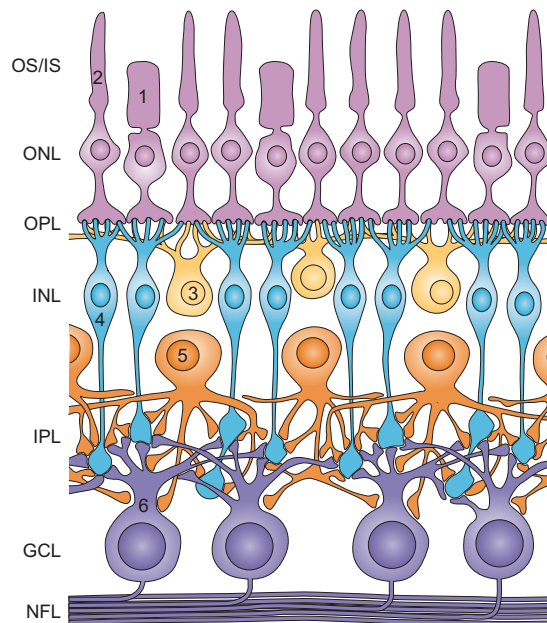


Figure 1.2: The retina in cross section. Adapted from Wässle (2004). OS/IS: Outer and inner segments of photoreceptors. Cones (1) mediate daylight vision, while rods (2) are responsible for vision during nighttime. ONL: Outer nucleus layer, where the photoreceptor cell bodies are located. OPL: Outer plexiform layer, which comprises the synapses between photoreceptors, bipolar cells (4) and horizontal cells (3). INL: Inner nucleus layer containing horizontal cell and bipolar cell bodies. IPL: Inner plexiform layer, which comprises the synapses between bipolar cells, amacrine cells (5) and ganglion cells (6). The different types of bipolar cells stratify in distinguished sublayers of IPL. GCL: Ganglion cell layer. NFL: Optic nerve fiber layer, which is the collection of ganglion cell axons.

Retinal ganglion cells (RGC) constitute the output cells of the retina. Their axons form the optic nerve which projects into higher visual areas of the brain. They can be also classified into ON and OFF type, depending on which type of cone bipolar cell they are connected to. OFF ganglion cells, which are excited by a decrease in light intensity, are the most abundant type in the amphibian retina (Burkhardt et al. 1998, Geffen et al. 2007, Segev et al. 2006). Interestingly, rod ON bipolar cells are not directly connected to ganglion cells. They make contact only to AII amacrine cells which then forward the signal to ganglion cells (Fig. 1.3).

Under photopic conditions, the rod pathway saturates and does not contribute to the retinal light response. Hence, the major signal pathway comprises cones, bipolar cells and ganglion cells, only involving glutamatergic synapses. This so-called vertical pathway is characterized by a pronounced signal convergence. Each bipolar cell receives input from 5 to 10 photoreceptors (Wässle 2004), and each ganglion cell pools signals of about 10 to 100 bipolar cells (Gollisch and Meister 2010).

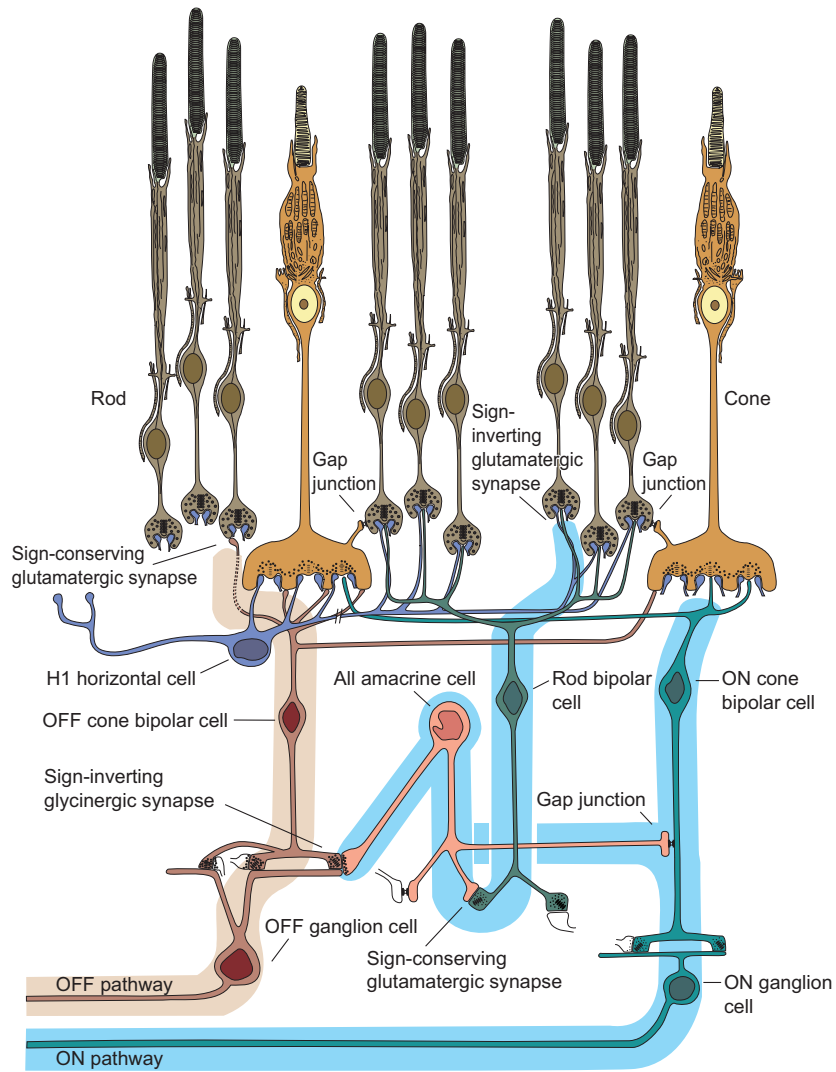


Figure 1.3: ON and OFF pathways in the retina. Indicated are the most important synapses. Adapted from Sharpe and Stockman (1999).

Additionally, a lateral signal flow is present in the network. It is mainly mediated by horizontal cells and amacrine cells. Horizontal cells are connected to each other via electrical synapses, so-called gap junctions, and thus form large electrically coupled networks (Baldrige et al. 1998). They provide negative feedback to photoreceptors which is classically thought to be GABAergic, although several different hypotheses exist and are supported by data (Wu 1994, 2010). Evidence increases that they also provide inhibitory input to bipolar cells (Duebel et al. 2006). Also amacrine cells can form gap junctions, either among each other or onto different cell types, as for example bipolar cells (Famiglietti and Kolb 1975, Nelson 1982, Sharpe and Stockman 1999). Amacrine cells are the morphologically most diverse cell type in the retina, forming all kinds of connections. A rough separation can be made into narrow-field and wide-field amacrine cells, which describes the area over which they collect input. Amacrine cells are mostly inhibitory; they release either glycine or GABA. Some types, however, have been shown to release glutamate (Johnson et al. 2004, Haverkamp and Wässle 2004), dopamine (Kolb et al. 1981, 1992) or acetylcholine (Famiglietti 1983, Masland and Tauchi 1986); and more are suspected.

A specialty of the retinas of some mammalian species is the fovea. This is a spot of retina with a particularly high density of cones and no rods. In this region, each ganglion cell receives input from only a single cone (Dowling and Boycott 1969, Banks et al. 1987, Schein 1988). Hence, the convergence of information is abolished in this region. To allow the light to be transmitted to the cones with minimal refraction, the ganglion cells are horizontally displaced. Notably, the fovea does not exist in the amphibian retina. Here the cell distribution is approximately homogeneous over the retina.

Besides neurons various glial cells exist in the retina. They are not directly involved in the information processing, but they support the neurons of the retina. One particularly interesting glial cell type are the so-called Müller cells. It has been shown that they serve as optical fibers, guiding the light through the retinal tissue to the photoreceptors (Franze et al. 2007).

Most of the cells in the retina respond to inputs with graded potentials. Only ganglion cells and some amacrine cells generate action potentials¹. Spikes of ganglion cells constitute the only output signals of the retina. This makes the retina a particularly nice system to study neuronal processing. The visual input can be easily controlled and the output can be accessed via the optic nerve axons or directly via the easy to access ganglion cells. Furthermore, there is only very little feedback from the brain to the retina (e.g. Lindstrom et al. (2009)).

¹A recent study presents evidence that also bipolar cells generate action potentials (Dreosti et al. 2011).

1.2 RECEPTIVE FIELDS AND CENTER-SURROUND ANTAGONISM

An important concept is the notion of the receptive field of a cell. This is simply the area over which it collects input. In particular, the receptive field of a retinal ganglion cell corresponds to the specific patch of retina in which light stimulation leads to a response of this cell. If the retina is light-stimulated via a monitor, each part of the monitor will be projected onto a specific part of the retina. Thus, the definition of the receptive field can be extended to describe the area on the monitor which can trigger a spiking response in the ganglion cell.

Furthermore, the definition of the receptive field is often generalized not only to describe the spatial extent of the cell's responsiveness, but also the local stimulus-response dependency. As an example, a ganglion cell is typically more strongly excited by stimuli focused on the center of its receptive field rather than on the periphery. This is because central photoreceptors and subsequent bipolar cells are thought to have a stronger weighted synaptic connection than cells further away from the center (Kier et al. 1995). Thus, the receptive field would be described by a function which has its maximum at the position of the ganglion cell and declines with increasing distance until zero.

However, in most ganglion cells, exposing the receptive field surround to a certain light intensity even leads to an opposite response than central exposition (Kuffler 1953, Barlow 1953). In OFF cells, dark stimuli in the center act depolarizing while dark stimuli in the surround have a hyperpolarizing effect. The opposite can be found in ON cells. Because this surround-triggered hyperpolarization reduces spiking, the receptive field surround is said to be *suppressive*.

In cat retinas, Kuffler (1953) found that bright stimuli in the surround of OFF center cells can trigger action potentials in ganglion cells. Thus, the cells respond to surround stimuli of opposite polarity than stimuli preferred by the center; leading to the term *responsive* surround. Barlow, on the other hand, reported a purely suppressive effect of the surround in frogs (Barlow 1953), although this notion was questioned several times (Keating and Gaze 1970, Morrison 1975b,a, Donner and Grönholm 1984). Both effects, suppression of responses upon equipolar stimulation of the surround, and generation of responses upon antipolar surround stimulation, are condensed into the notion of the so-called antagonistic surround. It is generally not straight forward to disentangle experimentally if this antagonism indeed corresponds to a suppressive surround, a responsive surround, or both.

Furthermore, this antagonistic receptive field organization is not only found in ganglion cells, but also in bipolar cells.

In the following, we give a summary about what is already known about the pathways and mechanisms or the receptive field surround. These facts will be the foundation for our investi-

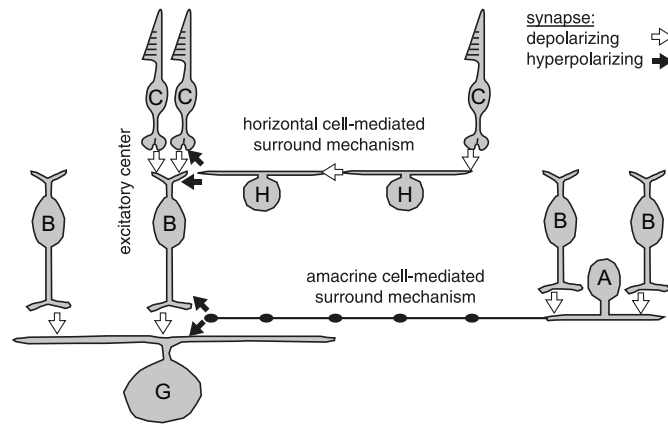


Figure 1.4: Circuitry for receptive field center-surround mechanisms. Adapted from Zaghloul et al. (2007). Lateral inhibition from the surround is mediated in the outer plexiform layer via horizontal cells, and in the inner plexiform layer via amacrine cells. The latter generate either pre- or postsynaptic inhibition.

gation of center-surround integration in chapter 5.

Classically, horizontal cells are thought to mediate the antagonistic surround of bipolar cells (Fig. 1.4, Werblin (1974), Werblin and Dowling (1969), Werblin (1972), Thibos and Werblin (1978)) via a feedback mechanism to the photoreceptor cones (Mangel 1991, Wu 1991). However, recent studies suggest that several mechanisms might play a role in generating this bipolar cell antagonistic surround, including inhibitory feedback from amacrine cells and feedforward inhibition directly from horizontal cells to bipolar cells (Roska et al. 2000, Duebel et al. 2006, Zhang and Wu 2009).

The origin of the center-surround antagonism in ganglion cells is even more controversial. The simplest possibility is that the surround is inherited from bipolar cells. One would expect that this would result in a weak ganglion cell surround of the same size of the surround of an individual bipolar cell (see Appendix A for discussion). This notion is supported by studies demonstrating that indeed the ganglion cell surround antagonism critically depends on horizontal cell signaling (Mangel 1991, McMahon et al. 2004). In contrast, other studies suggest that the antagonistic surround is mainly mediated by amacrine cells (Fig. 1.4, Cook and McReynolds (1998), Zaghloul et al. (2007)) either by pre- or postsynaptic inhibition. Furthermore, it was shown in rabbits that GABA is responsible for a major component of surround antagonism (Flores-Herr et al. 2001), while a study in primates comes to the conclusion that non-GABAergic pathways primarily mediate the receptive field surround (McMahon et al. 2004). Indeed, several pathways seem to play a role (Ichinose and Lukasiewicz 2005), and it is not clear yet to what extents the different mechanisms contribute.

1.3 RETINAL ADAPTATION

To guarantee adequate visual function during all light conditions, the eye provides various adaptation mechanisms to align the neuronal output range to the environmental input range. The first step to achieve this is luminance adaptation, in which the eye adjusts to the mean light level. There are mechanical contributions, i.e. the well known pupil contraction in response to bright light, as well as neuronal mechanisms provided by the retina (Shapley and Enroth-Cugell 1984). Retinal luminance adaptation already starts in the photoreceptors, where the gain in the phototransduction cascade is regulated by several molecular mechanisms (Pugh et al. 1999). This early adaptation is accompanied by several postreceptoral mechanisms (Barlow and Levick 1969, Enroth-Cugell and Lennie 1975).

The second step is an adaptation to the variance of the visual input, i.e. the contrast (Shapley and Victor 1978). Two types of contrasts can be distinguished: temporal contrast denotes the variance in time of a stimulus at a certain location. On the other hand, spatial contrast denotes the stimulus variance at a certain time point across different spatial areas. Temporal contrast adaptation is largely independent of luminance adaptation (Mante et al. 2005). It occurs on at least two different time scales: the fast component decreases the sensitivity of retinal ganglion cells and increases the cells' kinetics in response to a contrast increase within 100 ms or less (Victor and Shapley 1987, Baccus and Meister 2002, Gollisch and Meister 2010, Demb 2008). This is generally referred to as contrast gain control. The second, slower component operates on a time scale of several seconds. It further decreases the cells' sensitivity while leaving the kinetics unaltered (Smirnakis et al. 1997, Baccus and Meister 2002, Manookin and Demb 2006).

In chapter 4, we will report the finding of a novel implementation of a gain control mechanism in the amphibian retina. Therefore we will now briefly summarize what is known so far about the cellular basis of contrast gain control. In contrast to luminance adaptation, it has been shown that transmitter release from photoreceptors is unaltered by contrast changes. Also horizontal cells do not seem to adapt (Rieke 2001, Baccus and Meister 2002, Beaudoin et al. 2007). However, bipolar cells are speculated to feature two sites of fast contrast adaptation. First, an unknown mechanism in the bipolar cell dendrites induces a sensitivity change as well as a change in kinetics (Rieke 2001, Baccus and Meister 2002, Demb 2008). Second, the bipolar cell synaptic terminals appear to contribute to the gain control effects measurable in ganglion cells via a synaptic depression mechanism (Demb 2008, Manookin and Demb 2006, Burrone and Lagnado 2000, Singer and Diamond 2006).

Synaptic depression refers to a weakening of the synaptic transmission during prolonged neurotransmitter release. The general idea is that each presynaptic terminal has a limited ready-

releasable pool of transmitter-filled vesicles. If the cell's excitation is big enough, these vesicles are released faster than the pool refills. Therefore, it depletes over time, and its capability of transmitting synaptic currents is weakened. It has been shown in rats that the synapses between bipolar cells and AII amacrine cells deplete with a rapid time scale of about 4 ms (Singer and Diamond 2006, Oesch and Diamond 2011).

Furthermore, in recent experiments it was shown that amacrine cells do not contribute to the gain control mechanism in the guinea pig retina (Beaudoin et al. 2007). Neither blocking pre- nor postsynaptic inhibition affected the gain modulation significantly. However, other studies suggested that adaptive signals can arise from peripheral regions of the receptive field (Shapley and Victor 1979, Enroth-Cugell and Jakiela 1980). This would require wide-field signals as mediated by amacrine cells. Thus, there might be additional amacrine cell dependent mechanisms which only contribute under certain stimulus conditions.

Finally, also the retinal ganglion cell itself has been shown to adjust the gain of its spike generation mechanism in a contrast dependent fashion (Zaghloul et al. 2005, Kim and Rieke 2001). In these studies, an increased adaptation in the spiking response compared to the subthreshold response has been reported. Thus, so-called spike-frequency adaptation seems to be involved, which modulates the cell's firing probability depending on the amount of previous spikes.

1.4 SPATIAL NONLINEARITIES IN RECEPTIVE FIELDS

Amphibian ganglion cells pool signals evoked by visual stimuli in their rather large receptive fields. These areas are as big as about ten degrees of arc. By comparison, a fly in ten centimeters distance covers only five degrees of arc. Each individual ganglion cell apparently *sees* a considerable part of the visual scene, and thus experiences many different light intensities, colors, or contrasts. The key question in this work is how these spatially distinct stimuli within the receptive field of a single ganglion cell are combined and encoded into the cell's spiking response.

So far, research on spatial integration of visual stimuli *within the receptive field center* has focused on distinguishing linear (X-type) and nonlinear (Y-type) integration by ganglion cells, respectively (Enroth-Cugell and Robson 1966, Hochstein and Shapley 1976). Parameterized model fits have suggested that Y-cell characteristics may result from half-wave rectification in spatial subfields (Baccus et al. 2008, Hochstein and Shapley 1976, Victor 1988, Victor and Shapley 1979), but detailed investigations of these functional nonlinearities are still lacking. If nonlinearities have been assessed previously in more detail, it was only on the level of individual circuit elements. In particular, Demb et al. (2001) reported that OFF bipolar cells feature

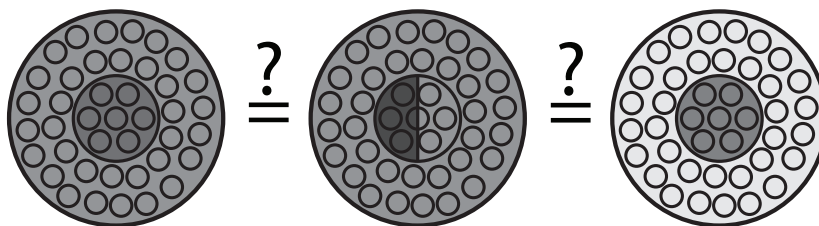


Figure 1.5: How are different stimuli within the receptive field of a ganglion cell combined? Do all these three patterns of stimulation lead to the same response? Shown are three ganglion cell receptive fields with their center-surround structure. The little circles correspond to individual photoreceptors which receive different inputs, indicated by the gray level. In all three cases, the integrated light intensity over the receptive field is equal.

a superlinear dependence of the transmitter release on depolarizing membrane potentials. Because the transmitter release was essentially zero at rest, hyperpolarizing membrane potentials did not further decrease neurotransmitter release and thus were not conveyed by the synapse (Demb et al. 2001).

The spatial integration of signals *in the receptive field center and its surround* is commonly described in the so-called linear-nonlinear model (see section 1.5), in which the spatial receptive field is usually approximated by the difference of two Gaussians (Grüsser and Grüsser-Cornehls 1973, Enroth-Cugell and Robson 1966, Dayan and Abbott 2001). This implies that the contributions of the center and the surround are integrated linearly with opposite sign, thus featuring both a suppressive and a responsive surround. Only little is known about the extent to which this linearity holds true. While some scientists report data that support this hypothesis (Enroth-Cugell and Lennie 1975), more recent studies suggest a nonlinear interaction of subunits which each have individual center-surround structures (Enroth-Cugell and Freeman 1987). Also a divisive effect of the antagonistic surround (Merwine et al. 1995) has been proposed.

A precise understanding of the nonlinearities underlying spatial integration in retinal ganglion cells is important to verify or falsify the already described models and to further elucidate retinal computations (Gollisch and Meister 2008, 2010, Münch et al. 2009, Ölveczky et al. 2003). Therefore, we study spatial integration in the receptive field center in-depth in chapter 4, applying the method of iso-response measurements. In chapter 5, we study the spatial integration of stimuli in the cell's receptive field center and its surround.

1.5 COMPUTATIONAL MODELS

Neural systems can be computationally modeled on various spatial scales spanning multiple orders of magnitudes (Herz et al. 2006). They range from models of individual ion properties (e.g. Santamaria et al. (2006)), over complete neuron models (e.g. de Schutter and Bower (1994)), up to network models of the entire retina (e.g. Saglam et al. (2009)) or a whole cortical column (e.g. in the Blue Brain Project). Biophysical models try to take into account the physiological circumstances as exactly as possible. This works fine on small spatial scales, where there are few free parameters and the computational effort is feasible. The larger the modeled structures become, the more details have to be replaced by abstract mechanisms. Ultimately, this can lead to phenomenological models that follow the *black box*-approach. They aim at reproducing the system output by a pure mathematical description without taking biophysics into account. This heavily simplifies the computations and is still appropriate to study system properties. These models are used in this work to describe the dependence of the spiking output of a retinal ganglion cell on the visual input projected onto the photoreceptor layer.

One of the most important phenomenological models of retinal ganglion cells is the linear-nonlinear (LN) cascade model (Fig. 1.6 A, Korenberg and Hunter (1986), Chichilnisky (2001), Dayan and Abbott (2001)). It comprises two processing steps. First, the stimuli $s(x, y, t)$ projected onto a certain position (x, y) on the retina at time t are integrated by a linear filter $f(x, y, t)$ to produce the so-called generator signal $g(t)$,

$$g(t) = \int_{R^2} dx dy \int_0^t d\tau f(x, y, \tau) \cdot s(x, y, t - \tau) \equiv f \star s.$$

This can be thought to resemble the current influx to the retinal ganglion cell. The filter describes stimulus properties the cell is sensitive to. It is zero for locations outside the ganglion cell receptive field. It also drops to zero for large t , mimicking the limited memory of a cell.

Second, the ganglion cell output $r(t)$ is computed from the generator signal by a nonlinear transformation,

$$r(t) = N(g(t)).$$

The nonlinearity N models the spike-generation mechanism in the ganglion cell, mostly comprising a threshold and saturation level. Thus, the output $r(t)$ can be considered as instantaneous firing rate of the cell. If necessary, a spike train can be generated from $r(t)$ by a Poisson process.

With this model, ganglion cell responses to simple stimuli can be reliably predicted. It is accurate enough even to be deployed in recently introduced retinal implants (Pandarinath and Nirenberg 2010). Importantly, all its components are directly assessable in the experiment (see

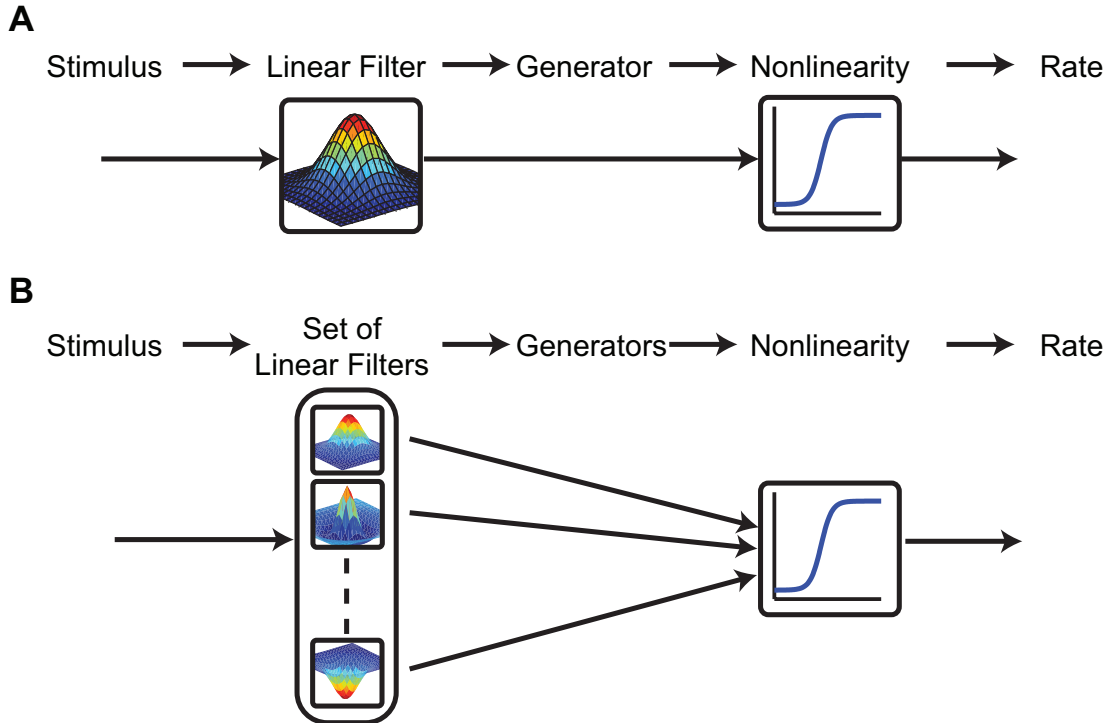


Figure 1.6: Retinal cascade models. **(A)** LN cascade model. The high-dimensional input is mapped onto a one-dimensional generator signal by a linear filter. Subsequently, the firing rate is derived by a nonlinear transformation. **(B)** Generalized LN model. Multiple linear filters map the visual input onto multiple generator signals. A high-dimensional nonlinearity (depicted here as one-dimensional nonlinearity) calculates the firing rate from these generator signals.

chapter 3.2). However, a strong limitation of the model is the assumption that the cell only responds to stimulus features that can be described by a single linear filter. This restriction is dropped in generalized LN models² which take into account several linear filters (Fig. 1.6 **B**). In these, the cell output is described by

$$r(t) = N(f_1 \star s, f_2 \star s, \dots, f_n \star s).$$

Also the components involved here, the filters f_i , and to a certain degree the nonlinearity N , can be determined experimentally. This, however, requires much longer measurements to gather enough statistics.

These models provide the framework for the computational description of retinal ganglion cells in this work. The black box approach, in which only input and output are considered, very

²Please note that what we refer to as generalized LN model does not correspond to the generalized linear model introduced in Pillow et al. (2008).

much corresponds to our experimental setting. We visually stimulate the retina and measure spikes from retinal ganglion cells. However, we do not have access to anything happening *in between*. In the next chapter, we will describe the experimental methods we used throughout this work to perform such measurements of spiking signals of retinal ganglion cells during visual stimulation.

2. EXPERIMENTAL PROCEDURES

The key aspect of this work was the performance of electrophysiological experiments to probe the mechanisms of stimulus integration in the retina. In this chapter, we will explain how the preparation of the retina was performed, how we stimulated the retina using a cathode ray tube monitor, and how we measured neuronal responses using multi-electrode arrays. In particular, the technical setup used to perform closed-loop experiments is described.

2.1 TISSUE PREPARATION AND SUSTAINMENT

We studied the retinas of adult axolotl salamander (*Ambystoma mexicanum*, Fig. 2.1 **A**) and frogs (*Xenopus laevis*, Fig. 2.1 **B**) of either sex. These systems were chosen because they provide a very robust retinal preparation. For this reason, amphibians have a long tradition in retina research, especially due to the work of H. B. Barlow, who started to work on frogs more than 60 years ago (Barlow 1950). Hence, a lot of previous knowledge is available in the literature which lays the foundation for this work.

Before starting the preparation, the animals were dark-adapted and chilled in an ice-water mixture for approximately 30 - 45 minutes. Then, they were sacrificed by decapitation, and the eyes were enucleated. The eye diameters ranged from about 3 mm (salamander) to 6 mm (frog). Both eyes were immediately submerged in oxygenated Ringer's solution (110 mM *NaCl*, 2.5 mM *KCl*, 1.6 mM *MgCl₂*, 1.0 mM *CaCl₂*, 22 mM *NaHCO₃*, 10 mM D-glucose, equilibrated with 95% O₂ and 5% CO₂).

The frontal part of both eyes was removed, and the posterior part cut in half. Then retina halves were isolated from the eye cup using glass rods with fire-polished tips. One retina half was used for immediate recording, while the other retina pieces were stored in cooled Ringer's solution for later recording. The whole preparation was performed with infrared illumination under a microscope equipped with night-vision goggles.

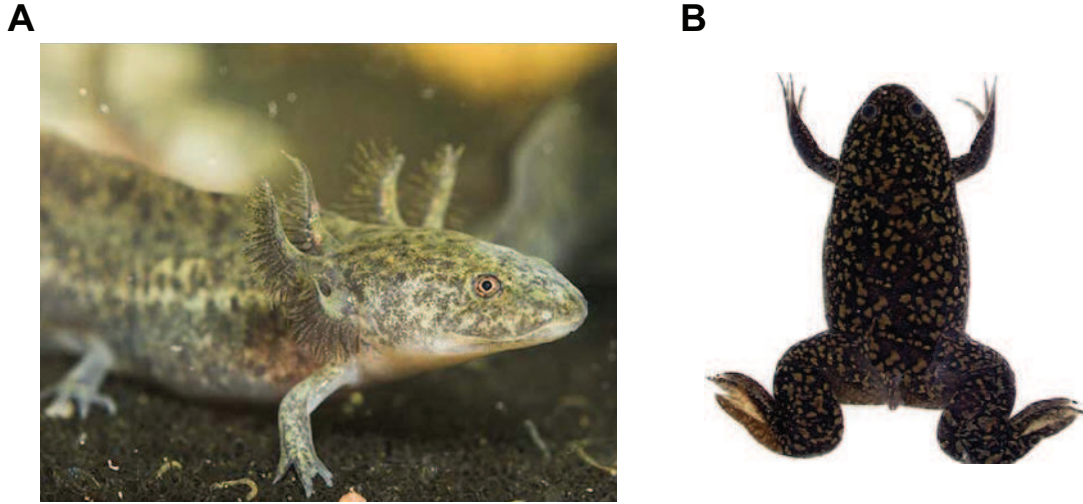


Figure 2.1: Model systems. (A) Axolotl salamander (*Ambystoma mexicanum*). (B) African clawed frog (*Xenopus laevis*).

2.2 ELECTROPHYSIOLOGY WITH MULTI-ELECTRODE ARRAYS

The electrophysiological recording of retinal ganglion cell action potentials was done using a multi-electrode array (Meister et al. 1994). We placed the isolated retina piece ganglion-cell-side down on a glass plate with 60 incorporated electrodes (Multichannel Systems, Fig. 2.2). To this end, the ganglion cell side was inferred from the curvature of the retina. Only the electrode tips were non-insulated, and thus able to make electrical contact. The tip size was 10 μm , roughly corresponding to the soma size of a ganglion cell. The spacing between electrode tips was 100 μm .

During recordings, retinas were continuously perfused with Ringer's solution at room temperature (20°C-22°C). For experiments with a pharmacological block of inhibition (Fig. 4.11 and 5.9), we added strychnine (5 μM), picrotoxin (150 μM) and bicuculline (20 μM) to the Ringer's solution and waited 20 minutes before resuming measurements (Rieke 2001, Ichinose and Lukasiewicz 2005). To block ON path contributions (Fig. 4.13), we used 200 μM 2-amino-4-phosphonobutyric acid (APB) (Slaughter and Miller 1981, Nakajima et al. 1993).

The measured voltage signals were amplified, band-pass filtered between 200 Hz and 5 kHz, and digitized at a sampling frequency of 25 kHz. If an off-line analysis of the recorded data was performed, we extracted spike timings from the voltage signal by using a Gaussian mixture model and an expectation-maximization algorithm for spike sorting (Pouzat et al. 2002). Online data analysis is described in section 2.4.

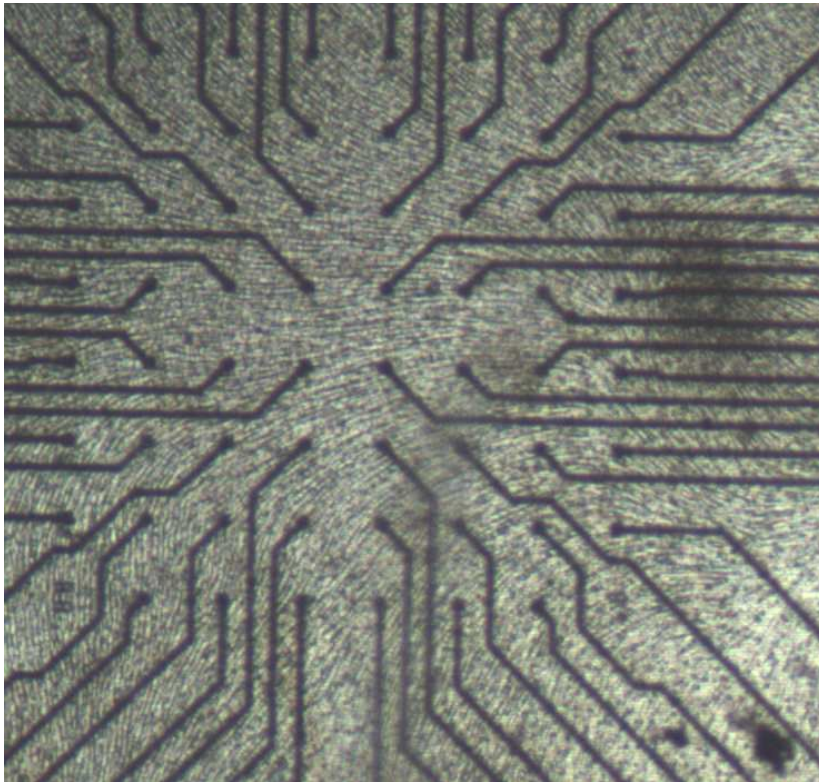


Figure 2.2: Multi-electrode array with salamander retina. The black traces are the electrode wires, the circular terminals the non-insulated electrode tips (10 μm). The photoreceptors are flattened by the applied pressure from the MEA glass plate and a holding membrane and are visible as a corn field-like structure. Irregular black patches are tissue leftovers from the pigment epithelium.

As mentioned earlier, ganglion cells are not the only spiking cell type in the retina. Certain types of amacrine cells also have the capability to fire action potentials. Fortunately, the somata of most of these cells are not in the ganglion cell layer. Thus, the spatial distance between electrodes and amacrine cell bodies is increased and spikes cannot be detected. There are, however, some displaced amacrine cells in the ganglion cell layer. One generally assumes that the probability of these cells firing detectable action potentials is very low. Therefore we presume throughout this thesis that all spikes detected by the planar multi-electrode array originate from retinal ganglion cells.

The benefit of using the multi-electrode array technique is that the extracellular recordings are very robust. They induce minimal stress to the retina and allow recordings over several hours. Importantly, a whole population of retinal ganglion cells can be assessed simultaneously.

2.3 VISUAL STIMULATION

In our experiments, the visual stimulation is performed using a γ -corrected cathode ray tube monitor. For this work, we only consider gray-level stimuli. This means that red, green and blue phosphors on the screen are homogeneously excited and the emitted light stimulates all photoreceptors approximately equally strong. The temporal image refresh frequency is 100 Hz; a new image is projected onto the retina every 10 ms. Experimental evidence lets us assume that this is fast enough to be considered as continuous by the retina (compare with Fig. 3.3). The image is projected from above onto the photoreceptor layer using standard optics. Each pixel on the monitor screen had a width of approximately $6 \mu\text{m}$ on the retina. The stimuli were controlled through custom-made software, based on Visual C++ and OpenGL.

In chapters 4 and 5 we use local step-like stimuli to assess the spatial integration of retinal ganglion cells. These stimuli were presented on a gray background with a light intensity of either $5.1 \text{ mW}/\text{m}^2$ (monitor 1) or $9.1 \text{ mW}/\text{m}^2$ (monitor 2) with no difference in results. We estimated the corresponding isomerization rates based on the measured spectrum of the light source and the photopigment spectral sensitivities (Makino et al. 1991) as well as the collecting areas (Perry and McNaughton 1991, Yang and Wu 1997) of rods and cones in the tiger salamander (*Ambystoma tigrinum*), which is closely related to the axolotl salamander. For the three major photoreceptor types (red-sensitive rod, L cone, S cone), we obtained the following values in isomerizations per receptor cell per second for the two different background light intensities: $2.5 \cdot 10^5$ (rod), $4.9 \cdot 10^3$ (L cone), $3.2 \cdot 10^3$ (S cone) and $4.4 \cdot 10^5$ (rod), $8.8 \cdot 10^3$ (L cone), $5.7 \cdot 10^3$ (S cone), respectively. At these isomerization rates, the rod pathway is saturated (Yang and Wu 1997), and thus is assumed not to contribute significantly to the neuronal responses.

To acquire precise information on the timing of the images shown on the monitor in relation to the recorded voltage traces, we displayed light pulses in one corner of the screen every time the monitor image was refreshed. These pulses either had a high or a low amplitude (Fig. 2.3). They were not visible to the retina, but were only detected by a photodiode which was attached to the monitor. The photo current was digitized and recorded together with the voltage traces from the multi-electrode array. During the image sequence of the stimulus, the pulses comprised a predefined sequence of high and low amplitudes. Hence, by keeping track of the control pulses, we could determine at which time point of the recording each frame was displayed on the monitor.

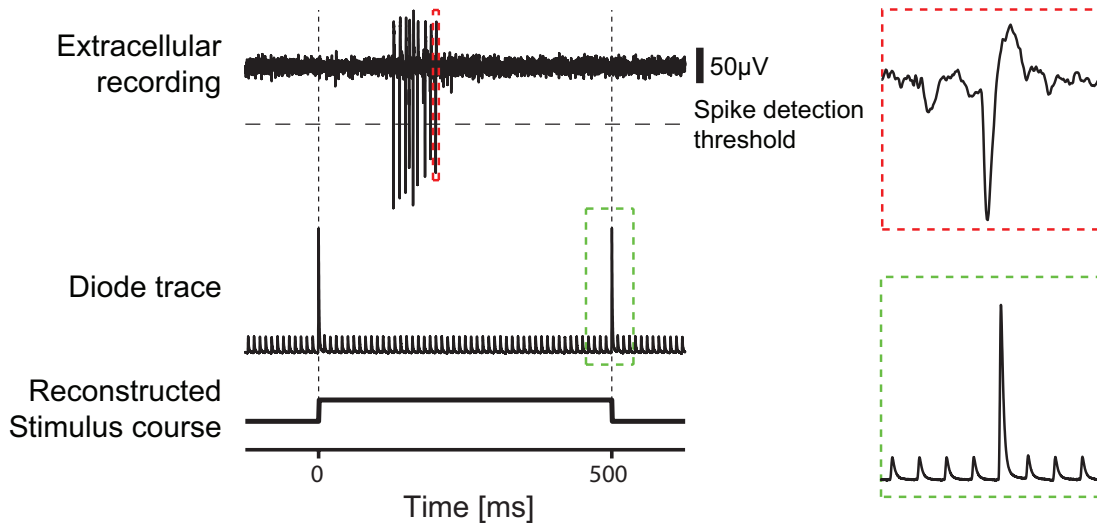


Figure 2.3: Sample voltage trace (top), stimulus-control diode signal (middle), and the stimulus timing which was reconstructed from the pulse times (bottom). Insets show a magnified spike (red box) and a zoom into the diode signal (green box).

2.4 CLOSED-LOOP EXPERIMENTS

The key experiments in this thesis, i.e. the measurements of iso-response stimuli, are performed using the so-called closed-loop approach. This means that the voltage trace of a distinguished channel of the multi-electrode array is analyzed during recording. Hence, spikes elicited by a certain ganglion cell, triggered by a certain stimulus, are detected online. The results can then be used to calculate the parameters of the stimulus that is shown next (Fig. 2.4).

So far we have described how we visually stimulate the retina, and how the elicited voltage signals are filtered, digitized and stored on a hard disk. These two processes are usually independent of each other; performed on different computers. They are manually controlled, i.e. recording and stimulation are started and stopped by hand. The closed-loop system connects these two processes. It automates the stimulation, recording, and data analysis. Furthermore, it allows the recording and stimulation computers to communicate; thus enabling us to tune the shown stimuli depending on the previous responses of a ganglion cell.

On the recording computer, data analysis was controlled by custom-made software, written in Visual C++. Incoming data were stored for off-line analysis as well as directly processed in an online fashion. At the beginning of each experiment, the voltage signals of all available channels were visually inspected. One channel was selected that displayed large, homogeneous spike shapes. For this channel, an amplitude threshold was determined, based on a one-minute

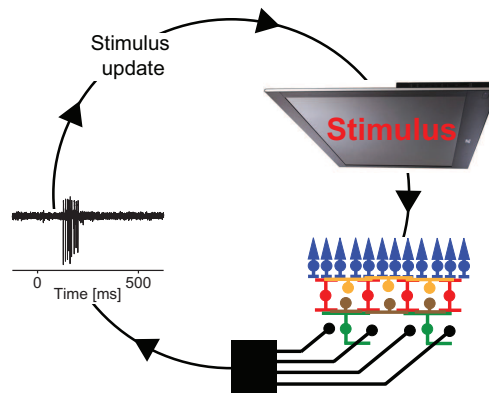


Figure 2.4: Schematic of a closed-loop experiment. The visually evoked action potentials of a retinal ganglion cell are detected online. The statistics of this spiking response are then used to determine the parameters for the stimulus that is shown next.

recording under stimulation with broad-band flickering light intensity, to separate spikes from background noise (Fig. 2.3). Only units whose spike amplitudes were well separated from the noise and that showed a clear refractory period were used for further investigation. To verify that the simple online spike detection and sorting worked well, we performed additional off-line analysis of spike shapes. This confirmed the results obtained directly from the online analysis. When pharmacological blockers were used, we first re-determined the threshold criterion of spike detection for the online analysis and verified that spikes could still be reliably detected.

Besides the extracellular potentials, the photodiode signal was recorded and analyzed online. This allowed us to verify that each stimulus had been displayed as intended¹. Second, we could reliably relate the spike timing to the stimulus timing.

After the spikes elicited by a certain stimulus had been detected, we could perform immediate data analysis. This allowed us for example to look at the temporal filter of the assessed ganglion cell before continuing the measurements. Most importantly, we could use the obtained spike statistics to compute the stimulus parameters of the stimulus that was shown next. If closed-loop experiments were running, these parameters were automatically sent to the stimulation computer. The communication protocol used the serial port to transfer the parameter set. The software on the stimulation computer was rewritten to accept the incoming parameters and automatically start and stop the stimulus sequence.

A typical closed-loop cycle of the iso-response experiments (chapters 4 and 5) took about 2200

¹Situations occurred where the computer was not fast enough in rendering the next image frame. Thus, the current frame was displayed longer than intended. The data analysis software either corrected for these frame drops or initiated a repetition of the whole stimulus.

ms. This time includes a 500 ms stimulation and recording interval, a 200 ms processing interval, and an additional 1500 ms resting period. During the processing interval, the response statistics are determined, and the new stimulus parameters are computed and communicated to the stimulus computer. During both the processing interval and the resting period, the retina is exposed to the gray background stimulus.

Now we have all the tools at hand to stimulate the retina and record the elicited neuronal responses. Data analysis can be performed either off-line, after the experiment, or online, to perform experiments in a closed-loop fashion. In the next chapter, we will introduce different experimental approaches for the analysis of spatial integration in the retinal network. They all rely on the data obtained in the experimental procedures described here.

3. METHODS FOR ASSESSING NONLINEARITIES IN RETINAL GANGLION CELLS

In this chapter we will discuss different experiments for the investigation of spatial integration in retinal ganglion cells. The aim is to find out how spatially distinct light stimuli within a single ganglion cell's receptive field are mapped onto the low-dimensional output of that cell. Speaking in mathematical terms, the goal is to assess if this mapping is linear, or, if not, which nonlinearities play a role. First we review the analysis used by Enroth-Cugell and Robson (1966). They were the first to distinguish linear from nonlinear integrating cells in the cat retina. Here, we discuss their approach on the basis of results from amphibian ganglion cells. Then the methods of spike-triggered systems analysis are introduced. Their role is twofold in this thesis. First, we apply them on spatial integration and discuss their benefits and limitations. Second, they allow us to perform a basic cell classification which we will commonly use to characterize the cells under investigation. Subsequently, we will motivate the measurement of iso-response stimuli to address the question of spatial integration and explain how these can be determined in a closed-loop approach.

All the methods in this chapter will be discussed in the framework of a subunit model. The underlying hypothesis in this model is that the retinal ganglion cell receptive field consists of independent spatial subunits. Each individual subunit linearly pools its inputs. The output of subunit i is generated from the input by a nonlinear function $N_i(\cdot)$. All subunit outputs then provide parallel feedforward signals to the ganglion cell. There they are summed and, via an additional nonlinear process $G(\cdot)$, converted into a response $r(\cdot)$ (Fig. 3.1),

$$r(s_1 \dots s_n) = G \left(\sum_{i=1}^n N_i(s_i) \right). \quad (3.1)$$

Thereby, $s_1 \dots s_n$ denote the subunit inputs. For clarity, we do not include a linear filter stage in this model. Neither do we take an explicit time dependence of the inputs into account.

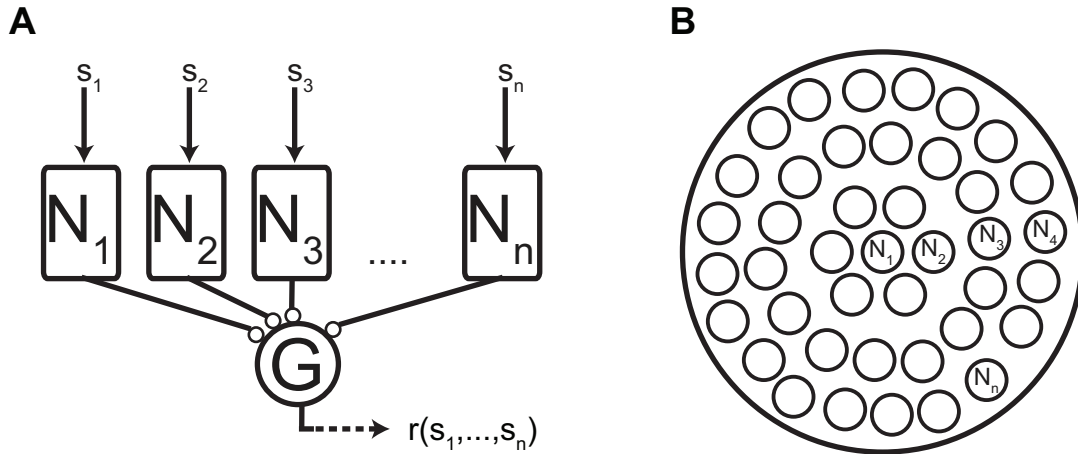


Figure 3.1: Hypothesized subunit model underlying the investigation of spatial integration. We assume that the ganglion cell receptive field consists of independent spatial subunits. These subunits pool their respective inputs linearly and consequently derive their output by a nonlinear transformation. The ganglion cell subsequently sums of all subunit outputs. (A) Side view. (B) Top view.

Lateral information exchange between the subunits is assumed to be negligible. This model evolves as a subtype from generalized LN models (chapter 1.5), and it is close to the retinal physiology: parallel subunits occur on different levels, e.g. photoreceptors or bipolar cells. Also the combined effect of photoreceptors, bipolar cells and narrow-field amacrine cells might be effectively described by a single isolated subunit. Even a wide-field amacrine cell can be captured in this framework if its response can be decomposed into functions which depend only on one input,

$$A(s_1 \dots s_n) = \sum_{i=1}^n A_i(s_i).$$

$A_i(\cdot)$ can be an arbitrary nonlinear function.

The key players in this model are the subunit nonlinearities $N_i(\cdot)$. They determine if spatial integration of signals from different subunits occurs in a linear or nonlinear fashion. Although this model is commonly used in the literature to capture nonlinear effects of retinal subunits (Gollisch and Meister 2008, 2010, Münch et al. 2009, Ölveczky et al. 2003), these important nonlinearities have never been determined in detail. Hence, this will be the goal for the methods introduced in the following.

3.1 X- AND Y- CELL ANALYSIS

We start our investigation by applying the method that led to the discovery of subpopulations of ganglion cells in the cat retina that have either spatially linear (X-cells) or nonlinear (Y-cells) response properties (Enroth-Cugell and Robson 1966).

Enroth-Cugell and coworkers stimulated the receptive field of a cat's ganglion cell with a stripe pattern. Neighboring stripes were of opposite contrast, calculated with respect to the integrated mean intensity. The width of each individual stripe was chosen to match the receptive field size. The grating was inverted every 0.5 seconds and spiking responses of ganglion cells were recorded in the cat's optic tract. Furthermore, the spatial phase of the grating was varied.

In the simplest case, the phase is set such that the receptive field of the cell is completely covered by a single stripe. Thus, it is uniformly illuminated and experiences a fullfield contrast reversal. From this stimulus, one can determine if a cell preferentially responds to bright or dark contrasts, viz. if it is an ON or OFF cell.

The most interesting case corresponds to the phase for which the receptive field is equally stimulated by two stripes, each of which covers one half of the receptive field. Because neighboring stripes have opposite contrasts, the integrated intensity over the receptive field will be zero. Therefore, a linear integrating cell would not show any response. In contrast, a nonlinear cell with a nonlinearity involving any kind of rectification would still respond to stimulus on- as well as offset.

In their measurements, Enroth-Cugell and Robson found both linearly and nonlinearly integrating cells. In linearly integrating cells, the opposite contrasts of two stripes were indeed averaged out and nullified the response. In nonlinear cells, on the other hand, no stimulus condition was found for which no response was elicited.

We adapted this method to characterize ganglion cells from frog and salamander. Therefore, we presented a spatial stripe grating with a bar width of 620 μm , chosen to correspond roughly to the extent of a receptive field of an amphibian retinal ganglion cell. Stripe intensities altered between black and white either in a square-wave or a sinusoidal fashion. Every 560 ms, the grating was either periodically inverted or switched on or off. This was repeated 30 times before the spatial phase of the grating was increased by 45 degrees, thus shifting the whole stimulus in space. Thereby, the receptive field was gradually exposed to different stimulus segments. The spatial and temporal mean intensity corresponded to an average gray which was defined to be the cells' null stimulus.

A typical result from a salamander OFF retinal ganglion cell is shown in Fig. 3.2. It was

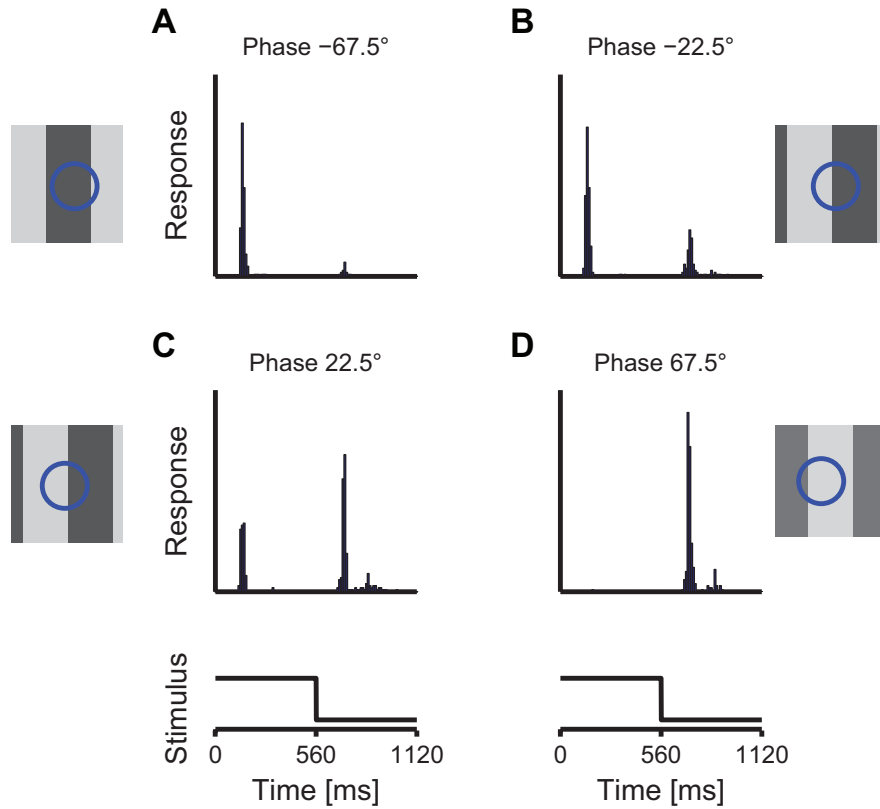


Figure 3.2: Stripe grating analysis. **(A)** Cell responds mostly to stimulus onset. **(B)** Cell responds to both stimulus on- and offset, but mainly to the former. **(C)** Cell responds to both stimulus on- and offset, but mainly to the latter. **(D)** Cell responds only to stimulus offset. In the bottom row, the reversal of the grating is indicated. The spatial phase at which the receptive field would be equally divided into two halves by the grating is set to be approximately at zero degree. That the cell responds to all shown stimuli indicates a nonlinear stimulus integration (Y-type).

measured with an inverting sinusoidal grating. One can clearly see that the cell responded under all stimulus conditions either at stimulus on- or offset, or both. Onset and offset thereby refer to even and odd reversals of the grating, respectively. As an example, let us discuss Fig. 3.2 **B** in more detail. There, the receptive field was covered to about two thirds by one stripe, and to about one third by the neighboring stripe of opposite contrast. Hence, the average contrast experienced by the cell was positive at one grating reversal, and negative at the other. Nevertheless, the cell responded to both reversals with an increase of its firing rate. Apparently, the response was not determined by the *linear* contrast average. This characterizes a Y-cell. In terms of the model of equation (3.1), the results can be best explained by assuming a half-wave rectifying nonlinearity $N(\cdot) = N(|\cdot|_+)$. Compared to the cat, one generally does not observe a decrease in firing rate for non-preferred stimuli in amphibians because of the lack of

maintained activity.

In a population analysis of 20 amphibian ganglion cells from multiple retinas, no indications for X-cells have been found.

Although Hochstein, Victor, and Shapley (Hochstein and Shapley 1976, Victor and Shapley 1979, Victor 1988) refined this approach to enable parameterized model fits, it is with this method generally not possible to get direct experimental access to more details of the involved nonlinearities. Also the spike-triggered analysis, introduced in the next section, will suffer from this disadvantage, but provide complementary information on the cells' stimulus integration.

3.2 SPIKE-TRIGGERED SYSTEMS ANALYSIS

In this chapter, we introduce the techniques of spike-triggered systems analysis and their application to investigate spatial integration. We will also describe how other response properties can be characterized using these methods, thus providing a basic cell classification.

All the methods presented here will rely on one basic principle. First, a set of random stimuli is presented to the retina and the spiking output is measured. Then, from all the stimuli presented, only those are picked out, which made the cell elicit one or more action potentials. This so-called spike-triggered stimulus ensemble is then investigated with statistical methods such as calculating averages (spike-triggered average, STA) or covariances (spike-triggered covariance, STC). The aim is to find out which stimulus features the cell responded to.

More specifically, the stimuli used for spike-triggered analysis typically consist of temporal or spatio-temporal Gaussian white noise. This has the advantage of spanning a wide range of possible inputs and being well suited to simultaneous measurements from multiple neurons (Chichilnisky 2001). In the case of temporal white noise, the whole retina is stimulated with a single intensity which is drawn randomly from a Gaussian distribution at each time step¹, therefore constituting a so-called fullfield flicker stimulus. In case of spatio-temporal white noise, the visual field is in addition subdivided into distinct areas, either in one (stripes) or in two dimensions (squares). A random intensity is then assigned independently to each subfield at each time step.

One assumes that the probability of a neuron eliciting a spike is governed by the white noise episode of a certain temporal length directly preceding the spike (Schwartz et al. 2006). The considered length thereby corresponds to the memory of the cell. The episode is characterized by the intensity values within each subfield; collected at each time step within the memory

¹Each time step typically consists of one or two refresh cycles of the CRT monitor.

interval. To have a handy representation, one accumulates all values of the stimulus episode preceding spike i within a single vector s_i . The collection of all vectors preceding a spike constitutes the spike-triggered ensemble. In contrast, the collection of all stimuli, no matter if they led to a spike or not, is called raw ensemble.

3.2.1 SPIKE-TRIGGERED AVERAGE

The simplest analysis is the computation of the STA. Therefore, we just average over all vectors within the spike-triggered ensemble,

$$\mathbf{A} = \frac{1}{N} \sum_{i=1}^N \mathbf{s}_i.$$

N is the total number of spikes, and s_i the vector representation of the stimulus preceding spike i . The underlying idea is that all uninteresting parts of the stimuli average out, if the ensemble is big enough. The resulting average will only consist of the one stimulus property the cell is really interested in. Indeed, it can be shown mathematically that if the cell can be described in the LN model (see section 1.5), the resulting STA estimates the linear filter in an unbiased way (Chichilnisky 2001).

In this thesis, the STA is used for several purposes. Most importantly, the temporal STA was measured for each ganglion cell to distinguish between ON and OFF cells. To do so, a temporal white noise stimulus was presented². The STA thus contained the particular temporal sequence of intensities which on average triggered spikes in the neurons (Fig. 3.3).

The classification into ON and OFF cells is then based on the extrema of the temporal STA. If an intensity minimum was preceding a spike on average, the cell was classified as OFF cell, otherwise as ON cell. Some OFF-cell STAs displayed a pronounced intensity maximum before the dominant minimum. This biphasic shape might arise from additional ON input which would render the cell an ON-OFF cell. In this thesis, no distinction is made between OFF and ON-OFF cells. This is because for the local stimuli applied in chapter 4, usually no ON responses could be observed.

Furthermore, for some cells we measured spatio-temporal STAs using a stimulus with 10x10 pixel wide square subfields³. Instead of displaying Gaussian white noise, the subfield intensities were randomly drawn as being either black or white (Fig. 3.4 A). This stimulus has the capability to drive the cell more strongly compared to Gaussian stimulation. Therefore, it trig-

²5 minutes recording time; 20 ms duration of one time step.

³around 20 minutes recording time; 20 ms duration of one time step. 10x10 pixel correspond to about 60x60 μm on the retina.

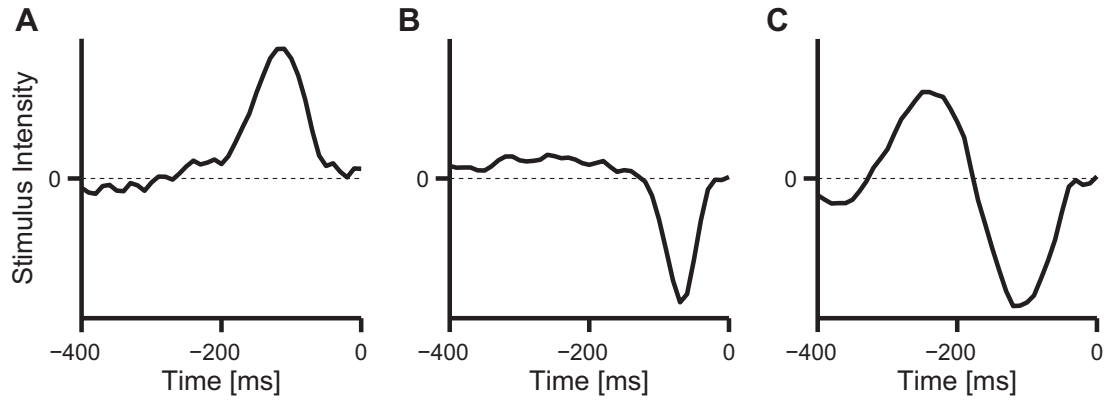


Figure 3.3: Temporal STA. Negative intensity values refer to dark stimuli, positive values to bright stimuli. (A) ON cell. (B) OFF cell. (C) Biphasic OFF cell.

gered more spikes within the recorded interval, and led to a bigger spike-triggered ensemble and a more reliable average. The result can be represented as a video. Each frame corresponds to a time step before a spike, and each pixel corresponds to the intensity value which the average spike-triggering stimulus had at that moment. From such a measurement, one gets both information: where the cell's receptive field lies in the visual space, and which dynamics the cell responds to, i.e. if it is an ON or an OFF cell.

A snapshot from such a video, measured from a typical OFF cell, is shown in Fig. 3.4 B. One can well recognize the cell's receptive field. Interestingly, although measurements with other methods indicate the presence of an antagonistic receptive field surround, it is not possible to resolve it in this measurement. This is presumably because the effect of the surround per area is typically much smaller than the effect of the center. Hence, a longer recording would be required to reduce statistical noise. This already indicates that white noise based systems analysis is problematic when attempting to investigate center-surround integration, for example.

After having determined the STA, which in the LN model corresponds to the cell's linear filter, it is now possible to determine the subsequent nonlinearity. This nonlinearity measures how strong the stimulus feature as described by the STA has to be present in the stimulus to trigger a spike. To this end, the scalar product of stimulus and STA is computed, yielding the so-called generator signal g ,

$$g_k = \mathbf{s}_k \cdot \mathbf{A}.$$

\mathbf{s}_k can be every stimulus from the raw ensemble and k denotes an arbitrary time step during recording. The generator signal g_k is then compared to the number of spikes r_k elicited in time step k . Subsequently, the data points (g_k, r_k) can be binned or fitted to approximate the model's nonlinearity.

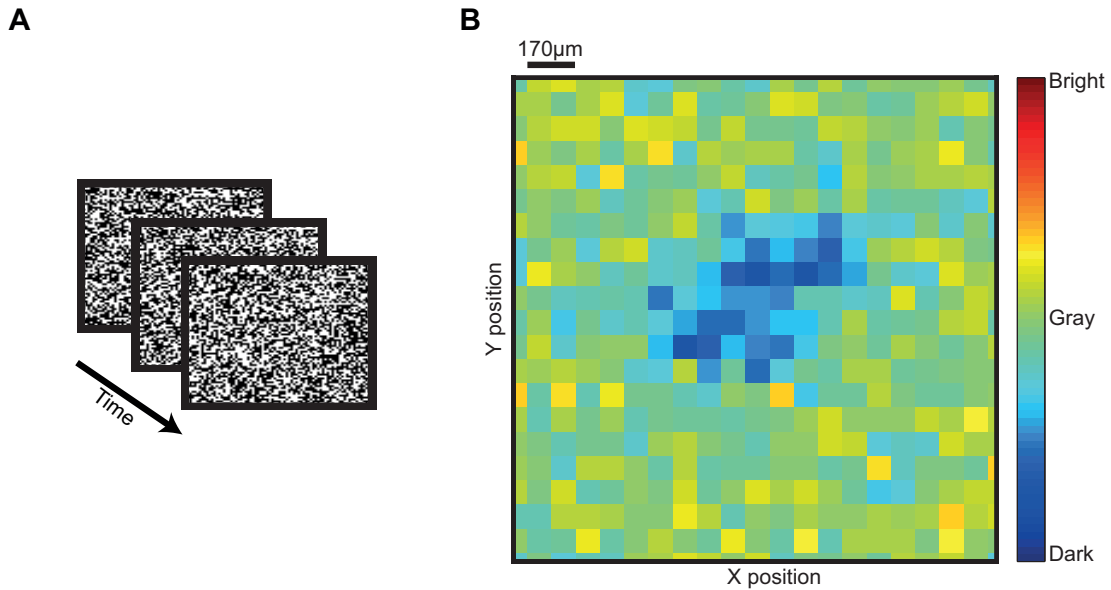


Figure 3.4: Spatio-temporal STA. (A) Checkerboard stimulus. Each square of the checkerboard was randomly set to either black or white each 20 ms. In the illustration, three typical screen shots of the stimulation monitor are shown. (B) The measurement was able to resolve the cell’s receptive field center, but not the antagonistic surround.

3.2.2 SPIKE-TRIGGERED COVARIANCE

In general, a neuron can respond to more than one single stimulus feature, as can be described for example in the generalized LN model (Fig. 1.6). The goal of the STC analysis is to determine all the filters which represent these features. For example, a neuron could respond to two stimulus features which are represented by opposite vectors in stimulus space. The STA would then be zero, but the STC analysis would still be able to recover the correct filters.

This is achieved by seeking directions in stimulus space in which the variance of the spike-triggered ensemble differs from that of the raw ensemble (Schwartz et al. 2006). To do so, the spike-triggered covariance matrix is computed,

$$\hat{C} = \frac{1}{N-1} \sum_{i=1}^N (\mathbf{s}_i - \mathbf{A})(\mathbf{s}_i - \mathbf{A})^T.$$

It is easy to prove (see Appendix B) that the directions with the biggest and smallest variances of the spike-triggered ensemble in stimulus space correspond to the eigenvectors of the covariance matrix with the biggest and smallest eigenvalues, respectively. The raw stimuli, on the other hand, have the same variance in all directions due to their spherical distribution. Therefore, we look at the eigenvectors of \hat{C} with significantly increased or decreased eigenvalues

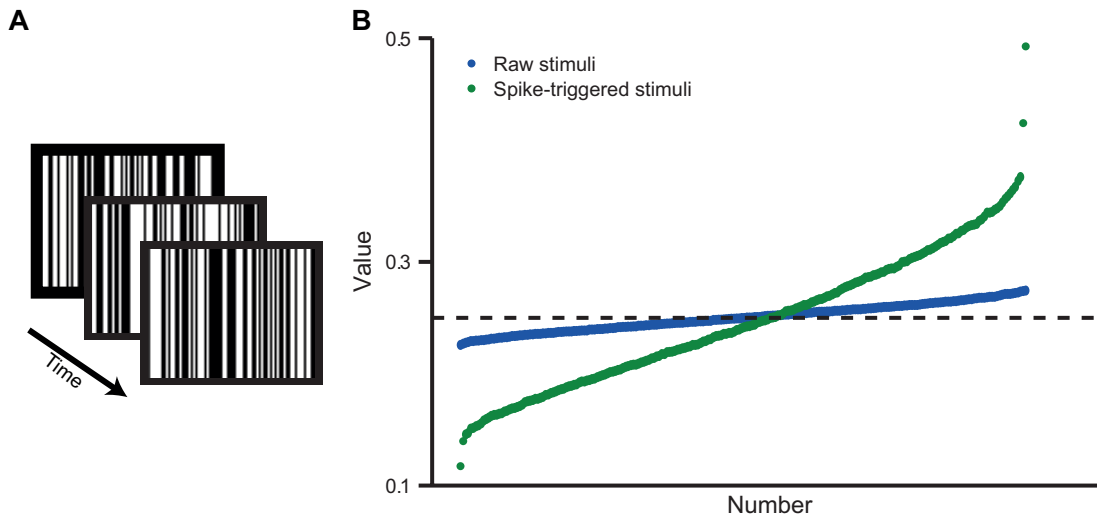


Figure 3.5: STC eigenvalues. **(A)** Stripe stimulus. Each stripe of $120\ \mu\text{m}$ width was randomly set to either black or white each 20 ms. In the illustration, three typical screen shots of the stimulation monitor are shown. **(B)** The dashed black line indicates the variance of the stimulus distribution. This corresponds to the asymptotic value of the eigenvalues of the raw stimuli for infinite measurement time. The smallest eigenvalue of the spike-triggered stimuli corresponds to the STA, the two biggest eigenvalues correspond to the eigenvectors with u-shaped nonlinearity that are shown in Fig. 3.6 **B** and **C**.

compared to the eigenvalues of the raw stimuli. They mark those directions in stimulus space, or stimulus filters, which are involved in triggering an action potential.

For each filter a nonlinearity can be computed separately, using the same procedure as described above for the STA by just exchanging the STA with the filter of interest.

We used this method to find further indications for a deviation of the cells' spatial integration from linearity. To do so, we used a spatio-temporal flickering stimulus. The spatial subareas constituted a stripe pattern with a bar width of $120\ \mu\text{m}$ (Fig. 3.5 **A**). The temporal step length was 20 ms, and typically we recorded for about 20 minutes. Random intensities were either drawn from a Gaussian distribution, or, as explained for the spatio-temporal STA, from a black and white distribution.

For a cell with linear spatial integration, one would expect the analysis to yield a single filter which represents the preferred stimulus of the cell. The recovery of several filters would by itself point toward a deviation from a simple LN type integration, and can for example indicate the presence of spatial subunits.

A typical measurement result is discussed in the following. The eigenvalue spectrum of the

spike-triggered stimuli of the assessed OFF cell (Fig. 3.5 **B**) shows two significantly increased eigenvalues as well as one significantly decreased eigenvalue. The deviation of the intermediate eigenvalues as well as the eigenvalues of the raw stimuli from the set stimulus variance (dashed line) were due to limited measurement time and therefrom emerging statistical fluctuations.

The eigenvector belonging to the significantly decreased eigenvalue corresponds to the STA of the cell (Fig 3.6 **A**). It has an increasing exponential-type nonlinearity and indicates the OFF characteristics of the cell. The eigenvectors belonging to the two biggest eigenvalues (Fig. 3.6 **B** and **C**) are spike-triggering stimuli orthogonal to the STA. In a linearly integrating cell, stimuli like these would induce a null generator signal and therefore not produce any action potentials. The eigenvector in Fig. 3.6 **B** indicates that preferred stimulation of half the receptive field alone could trigger spikes even if the other half was exposed to the non-preferred stimulus. This indicates the presence of a full- or half-wave rectifying nonlinearity in the receptive field subunits. The u-shaped nonlinearity of the measured filter indicates that it did not matter which side was stimulated with the preferred stimulus. The eigenvector in Fig. 3.6 **C** even subdivides the receptive field into three such subunits.

Unfortunately, the STC approach is very restricted by statistical limitations. Possible smaller subunits might not show up because the probability for them alone to trigger spikes is too small. Although it was recently shown in monkeys (Field et al. 2010) that it is possible to recover subunits of the scale of single photoreceptors in an STA analysis, it is yet another challenge to perform STC analysis on this data in order to estimate how these subunits are integrated. Furthermore, the obtained filters and nonlinearities do not directly correspond to the spatial subunits and their subsequent nonlinearities $N_i(\cdot)$. Although the model in equation (3.1) can be mapped to a model as shown in Fig. 1.6, the resulting filters of the STC analysis will typically correspond to arbitrary linear combinations of the filters and nonlinearities of individual subunits (see Appendix C for an example). Thus, determination of the latter is not possible without further model assumptions.

To overcome the problems of the analysis discussed so far, we introduce the method of iso-response stimuli in the following. It has the capability to directly measure nonlinearities in spatial integration and is less prone to statistical fluctuations.

3.3 THE ISO-RESPONSE METHOD

The method described in this section was first introduced in the auditory system. It was used to investigate the integration of frequencies in pure tones (Gollisch et al. 2002) and the integration of click stimuli (Gollisch and Herz 2005). The specific strength of this approach is the

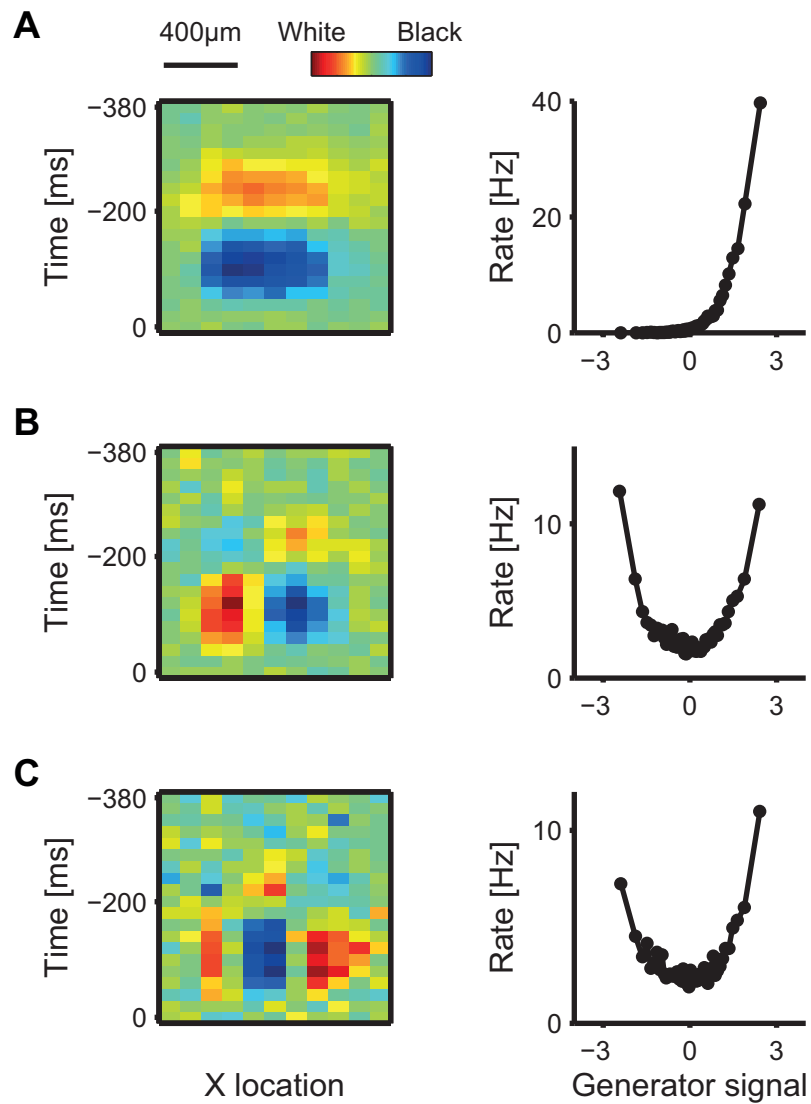


Figure 3.6: STC analysis using a stripe-pattern stimulus. At each time step, each stripe was randomly drawn to be either black or white. **(A)** STA with corresponding nonlinearity. **(B)** Biggest Eigenvector with corresponding nonlinearity. **(C)** Second biggest Eigenvector with corresponding nonlinearity.

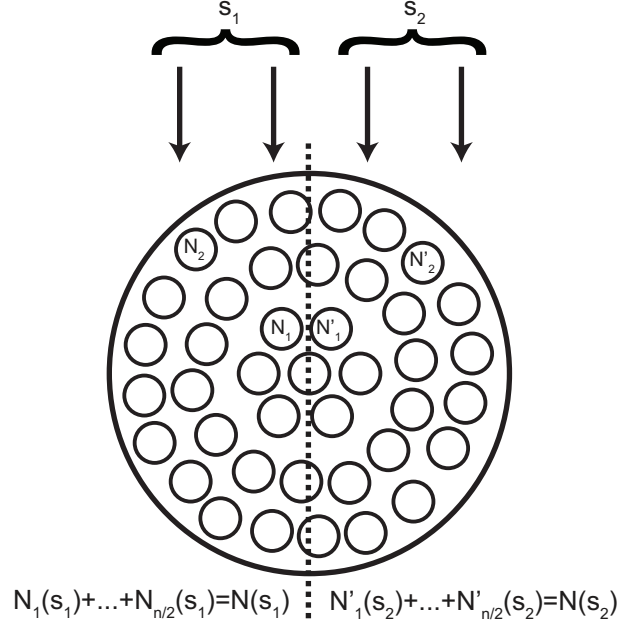


Figure 3.7: Simplified subunit model. Subunits in the left half of the receptive field receive an input s_1 , subunits in the right half an input s_2 .

assessment of the involved nonlinearities (Benda et al. 2007).

To explain the iso-response approach and at the same time work out its benefits, we discuss the responses of the subunit model (described in equation (3.1)) to a stimulus that divides the receptive field into halves and stimulates the subunits in each respective half equally (Fig. 3.7).

We assume that the ganglion cell receptive field is assembled from identical subunits, $N_i(\cdot) \equiv N_1(\cdot)$. Thus, the model can be rewritten to the simple form

$$r(s_1, s_2) = G \left(\sum_{i \in \text{left subunits}} N_i(s_1) + \sum_{i \in \text{right subunits}} N_i(s_2) \right) = G(N(s_1) + N(s_2)), \quad (3.2)$$

where $N(\cdot) \propto N_1(\cdot)$ indicates the effective subunit nonlinearity.

We now compare two hypothetical models with either linear ($N(s_i) = s_i$) subunits (Fig. 3.8 A) or rectifying-quadratic ($N(s_i) = |s_i|_+^2$) subunits (Fig. 3.8 B). The spike-generation nonlinearity $G(\cdot)$ is set to be

$$G(x) = \frac{1}{1 + \exp\left(-\frac{x-0.75}{0.5}\right)} \quad \text{or} \quad G(x) = \frac{1}{1 + \exp\left(-\frac{\sqrt{x}-0.75}{0.5}\right)} \quad \forall x \geq 0,$$

respectively. $G(x)$ is zero for $x < 0$. These functions are chosen to yield identical outputs

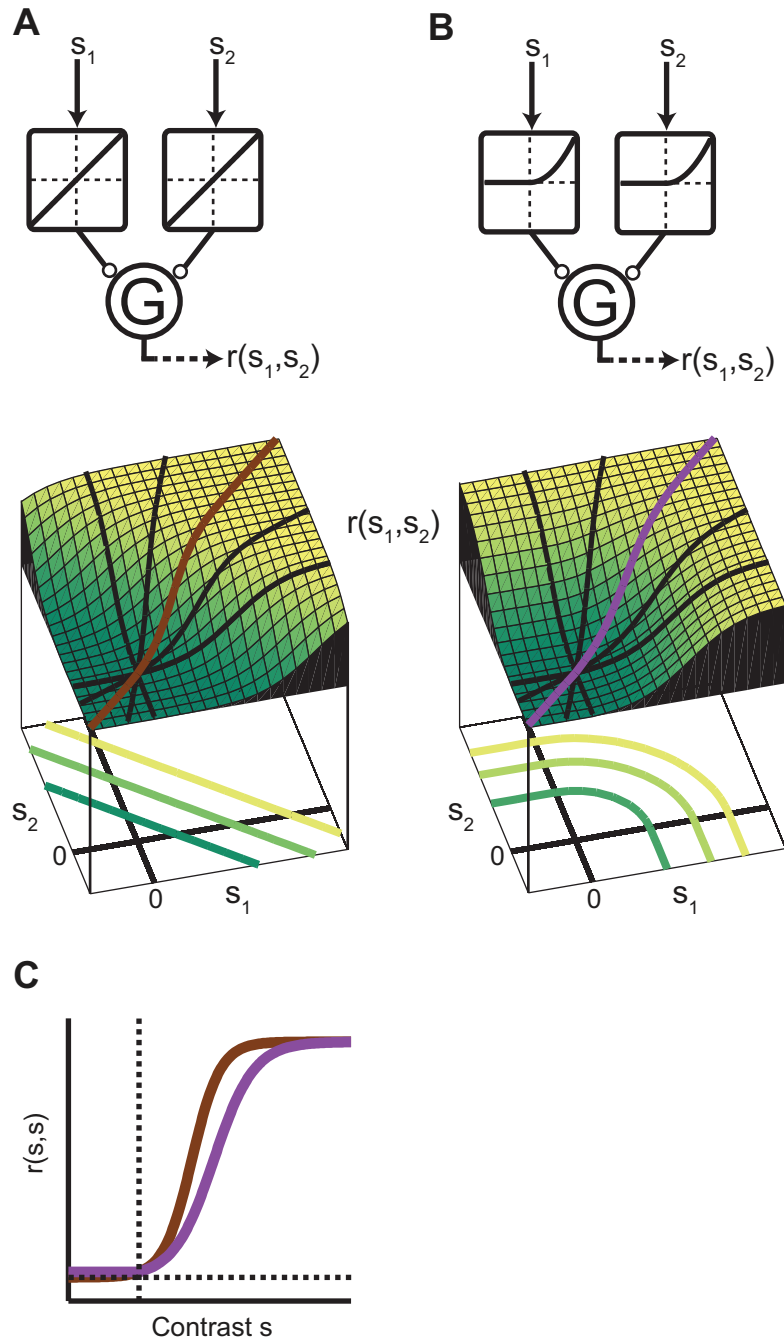


Figure 3.8: Model discrimination by iso-response curves. (A and B) Two fundamentally different subunit models together with their input-output relations. The model in A has linear subunits, while the model in B features rectifying-quadratic subunits. (C) Results of classical input-output measurements for both models for stimuli with $s \equiv s_1 = s_2$.

in case of stimulation of only one receptive field half. In a biophysical interpretation, they resemble an intracellular threshold and response saturation.

The ultimate experimental characterization of these models would be the measurement of the full input-output relation (Fig. 3.8, 3d plots). Although the stimulus space is just two-dimensional, to perform such a measurement with sufficient repetitions would require a substantial amount of measurement time. Most likely, it would still result in a coarse grained and noisy representation of the theoretical result shown in Fig. 3.8. Too much noise, however, easily obstructs the discrimination between the two models. The reason becomes apparent when comparing the plots from Fig. 3.8 **A** and **B**. Although the underlying nonlinearities $N(\cdot)$ are fundamentally different, the resulting 3d plots look very similar. This originates from the spike generation nonlinearity $G(\cdot)$ which dominates the resulting responses. When performing measurements in radial directions, e.g. along the brown and purple lines, one obtains input-output relations as shown in Fig. 3.8 **C**. Hence, such a measurement would lead to very similar results, and any signature of the underlying subunit nonlinearity is lost.

In contrast, the nonlinearity $N(\cdot)$ can be elaborated much better by looking at single iso-response curves, i.e. all stimuli (s_1, s_2) which lead to the same response (Fig. 3.8 contour lines). In case of the linear subunits, the curves are described by the equation

$$G(s_1 + s_2) = const \Rightarrow s_1 + s_2 = const,$$

in case of the rectifying-quadratic subunits by

$$G(|s_1|_+^2 + |s_2|_+^2) = const \Rightarrow |s_1|_+^2 + |s_2|_+^2 = const,$$

or in general by

$$N(s_1) + N(s_2) = const. \quad (3.3)$$

This formula is the implicit equation of a curve in two dimensions. The shape of the curve is determined by $N(\cdot)$. Thus, from the shape of the iso-response curves one can draw direct conclusions on the type of the subunit nonlinearity $N(\cdot)$ without any *a priori* assumptions. Moreover, each iso-response curve is independent of the output nonlinearity $G(\cdot)$.

Hence, the approach chosen in this thesis to investigate spatial integration in the retinal ganglion cell center is the experimental determination of iso-response curves (chapter 4). We do this, following the discussion in this section, by presenting two individual contrast steps to the different halves of the receptive field center (Fig. 3.9 **A**). To this end, the light intensities I_1 and I_2 in each receptive field half are simultaneously increased or decreased with respect to the gray background. Thus, the contrast is defined as the relative intensity difference before and after the stimulus is switched on,

$$s_i = \frac{I_i - I_{background}}{I_{background}}.$$

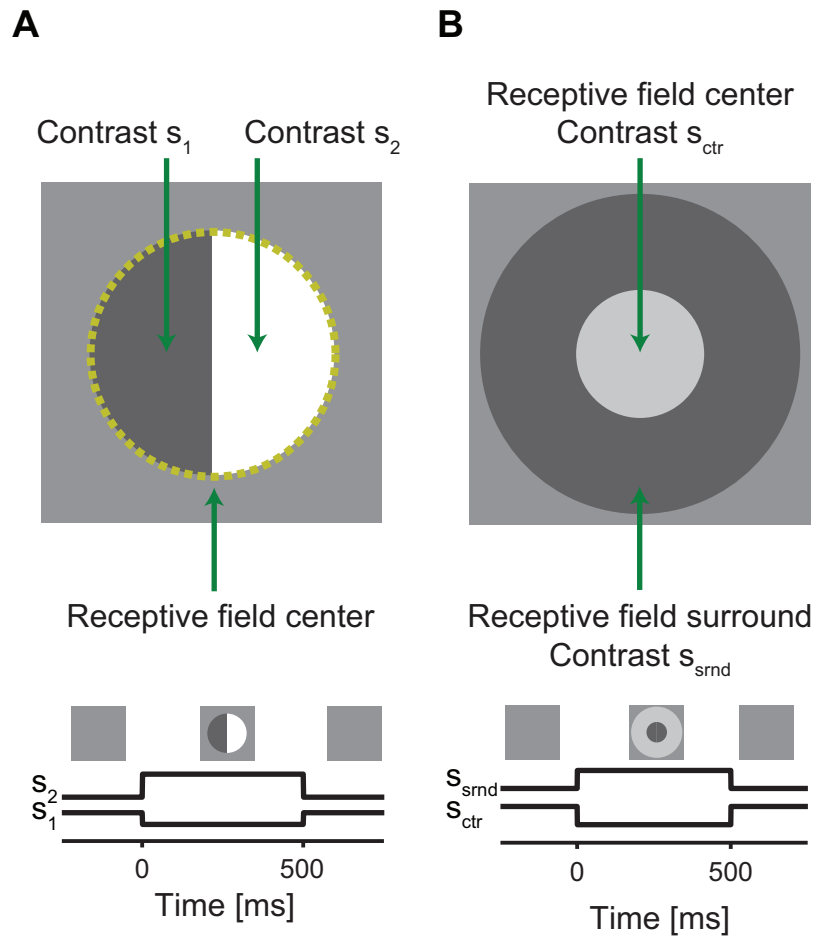


Figure 3.9: Stimuli used for the measurement of iso-response curves. **(A)** Stimulus used for the investigation of spatial integration in the receptive field center. **(B)** Stimulus to investigate center-surround antagonism.

In chapter 5 we will use the same approach to study the integration of stimuli presented in the center and in the surround. Therefore, center and surround subunits are separately stimulated (Fig. 3.7 **B**) with contrasts s_{ctr} and s_{srnd} , respectively⁴.

Without stimulation, amphibian retinal ganglion cells normally do not elicit spontaneous action potentials. In response to the stimulus onset, a burst of spikes is elicited before the cell silences again. It is generally thought that the bulk of relevant information in this response is encoded mostly in lower-dimensional response features, such as the number of spikes, or the first-spike latency. Thus, we chose these two quantities for the determination of iso-response curves in this thesis. On the one hand, the number of action potentials elicited by a stimulus onset is taken

⁴We will explain in chapter 3.4 how the border between center and surround is defined.

into account. That is, those stimuli which on average led to the same spike count are compiled in so-called iso-rate curves. On the other hand, the first-spike latency is taken into account in so-called iso-latency curves. These curves represent the combinations (s_1, s_2) which lead on average to a constant time between stimulus onset and the first spike.

In order to measure iso-response curves in an efficient way, we will use an online search algorithm during the experiment. This allows us to actively search for iso-response stimuli. Details of this closed-loop paradigm are described in the following section.

3.4 CLOSED-LOOP DETERMINATION OF ISO-RESPONSE STIMULI

As motivated in the previous section, the determination of iso-response curves is a well suited tool for the assessment of subunit nonlinearities. The simplest way to obtain such a curve is to uniformly sample the whole stimulus space and then use the data to post-hoc determine those stimuli leading to the same response. The reason that this is not efficient is rooted in the fact that most information obtained by such a measurement will describe the output nonlinearity, and thus does not contribute in the description of the subunit nonlinearity. To overcome this problem, we use the closed-loop approach for the measurement of iso-response curves by an online search algorithm. Furthermore, we employ it for a rapid determination of spatial receptive fields of ganglion cells.

We start with the latter, because the assessment of the size and position of the ganglion cell's receptive field is a prerequisite for the investigation of spatial integration, where the stimuli we use have to be aligned to those structures. The procedure consists of two major parts. First, the center spot of the receptive field center is determined. Thereafter, we measure the size of the receptive field center.

The center spot of the spatial receptive field of a recorded ganglion cell was determined by finding the midlines of the receptive field in two orthogonal directions and then using their crossing point (Fig. 3.10 **A** and **B**). Each midline was determined in the following way: We initially separated the available stimulation area by a straight separation line into two equal regions and presented alternating black-white stimulation at 1 Hz for 6 sec first in one region and subsequently in the other region. We then calculated the difference in spike count for the two regions. Subsequently, the position of the separation line was shifted and the measurement repeated. A simple search algorithm (see Methods in Appendix J.1) was applied to search for the specific position that yielded zero spike count difference. At this position, we assumed that the line divides the receptive field into equal halves.

In order to determine the radius of the receptive field center a blinking spot was presented,

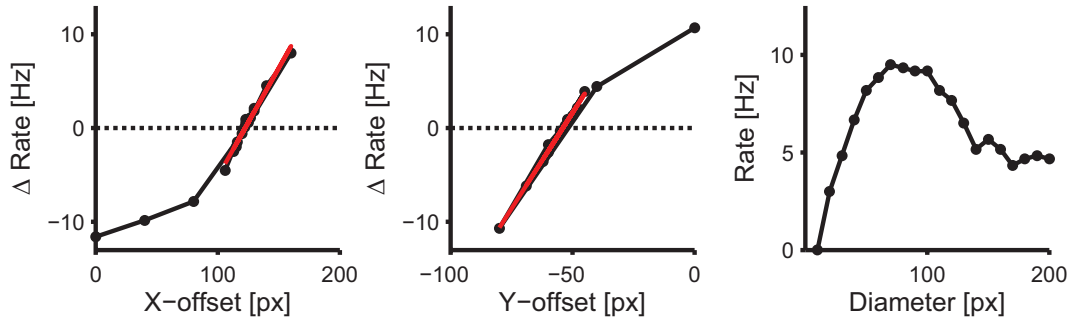


Figure 3.10: Online receptive field estimation. (A) Estimate of the receptive field midline in x direction. The red line indicates the linear fit of the data points close to Δ Rate = 0. The midline of the receptive field in x direction was defined as the root of the linear function. (B) Estimate of the receptive field midline in y direction. The receptive field midpoint was then defined as the crossing point of both midlines. (C) Estimate of the receptive field center radius. The receptive field center size was defined by the spot diameter eliciting the maximum number of spikes.

centered on the obtained receptive field midpoint (Fig. 3.10 C). The spot alternated between black and white at 1 Hz for 6 sec, and then the spot radius was successively increased from 5 to 100 pixels in steps of 5 pixels. The radius that elicited the maximum spike number was used as the radius of the receptive field center. For the investigation of center-surround integration, the receptive field surround was defined as an annulus with a width of approximately 450 μ m (outside radius minus inside radius) around the center. This area does not necessarily cover the whole ganglion cell surround, but a big enough portion to strongly contribute to the cell's response.

For some cells, we compared the result of this online receptive field determination to the receptive field estimation as obtained by a spatio-temporal STA measurement (Fig. 3.11). The agreement of both measurements was consistently very high. For some cells, the size estimate from the online procedure slightly exceeded the estimate from the STA measurement. This is most likely due to the fact that the excitatory contributions at the receptive field border are very small and cannot be resolved in the STA measurement.

Next, we describe the online procedure which is used to efficiently measure iso-response curves. The stimuli, as described in Fig. 3.9, consist of two contrast values spanning a two-dimensional stimulus space, in which iso-response curves were analyzed. Individual stimuli were presented either for 200 ms or for 500 ms, and spike counts were determined over 300 ms or 500 ms, respectively, with no differences in the results. The stimulus time course is shown in Fig. 3.12 A and D. Typically, a single stimulus presentation was used for every stimulus; in some trial experiments, each stimulus was repeated twice and responses were averaged, again

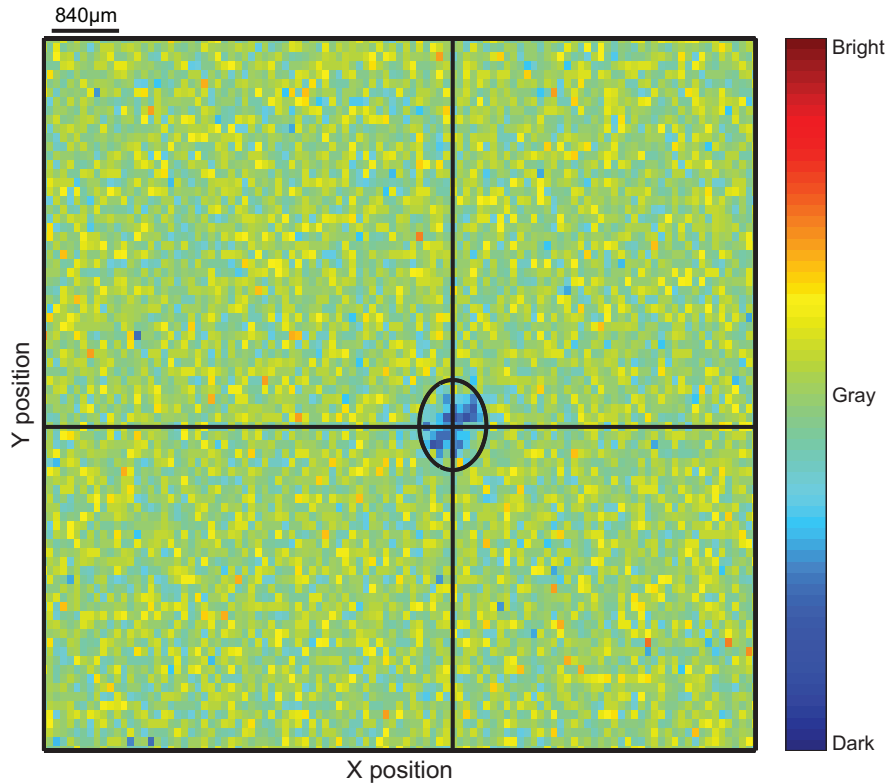


Figure 3.11: Comparison of the online receptive field estimate (black lines and black circle) with the spatial STA (color code) calculated from spikes elicited by a checkerboard white-noise stimulus.

with no effect on results.

For each measured iso-response curve, we selected a predefined response (either average spike count or average first-spike latency). The response selection typically aimed at requiring around 30-70% contrast for the predefined response from stimulation of one receptive field half alone. Using this range largely avoided coming too close to the physical limit of 100% contrast along the iso-response curve and at the same time provided enough contrast for reliable spike responses.

Each data point of an iso-response curve was obtained by performing a line search along a radial direction in stimulus space. The line was determined by fixing a certain angle $\alpha = \tan^{-1}(s_2/s_1)$ in stimulus space. Along this line a search algorithm (see Methods in Appendix J.2) was applied to find the radius $r = \sqrt{s_1^2 + s_2^2}$ that corresponded to the predefined response. Typically, we interleaved measurements along multiple search directions in a randomized fashion in order to minimize adaptation effects. In some experiments, the measurements were performed one search direction after another with no differences in the results.

After enough data for each angle had been acquired, the obtained data points in the vicinity of the aspired response (see Methods in Appendix J.2) were fitted by a linear function (iso-rate curves, e.g. 3.12 **B** and **E**) or an exponential function (iso-latency curves, e.g. 3.12 **C** and **F**):

- Iso-rate curves: $\text{Rate} = \text{Rate}_{\text{predef}} + b \cdot (r - r_0)$
- Iso-latency curves: $\text{Lat} = (\text{Lat}_{\text{predef}} - b) \cdot \exp((r - r_0)/s) + b$

The fit parameters r_0 and b (and s in the case of the iso-latency curve) were adjusted according to a least-squares criterion. The curve fit yielded the radius r_0 that corresponded to the predefined response ($\text{Rate}_{\text{predef}}$ or $\text{Lat}_{\text{predef}}$). Error bars of the iso-response curves displayed in the following chapters (e.g. Fig. 4.2 **B-D** or Fig. 5.3 **A-D**) represent 95% confidence intervals of the fit parameter r_0 . If the predefined response could not be reached within the available contrast range, the obtained data points were extrapolated. Such data points and data points from the fit that lay outside the available contrast range are marked in the iso-response plots by dashed lines connecting these points to their neighboring data points.

In the following chapter, we present the data obtained from such a closed-loop measurement of iso-response stimuli and investigate how spatially distinct stimuli are integrated within the receptive field center of a ganglion cell.

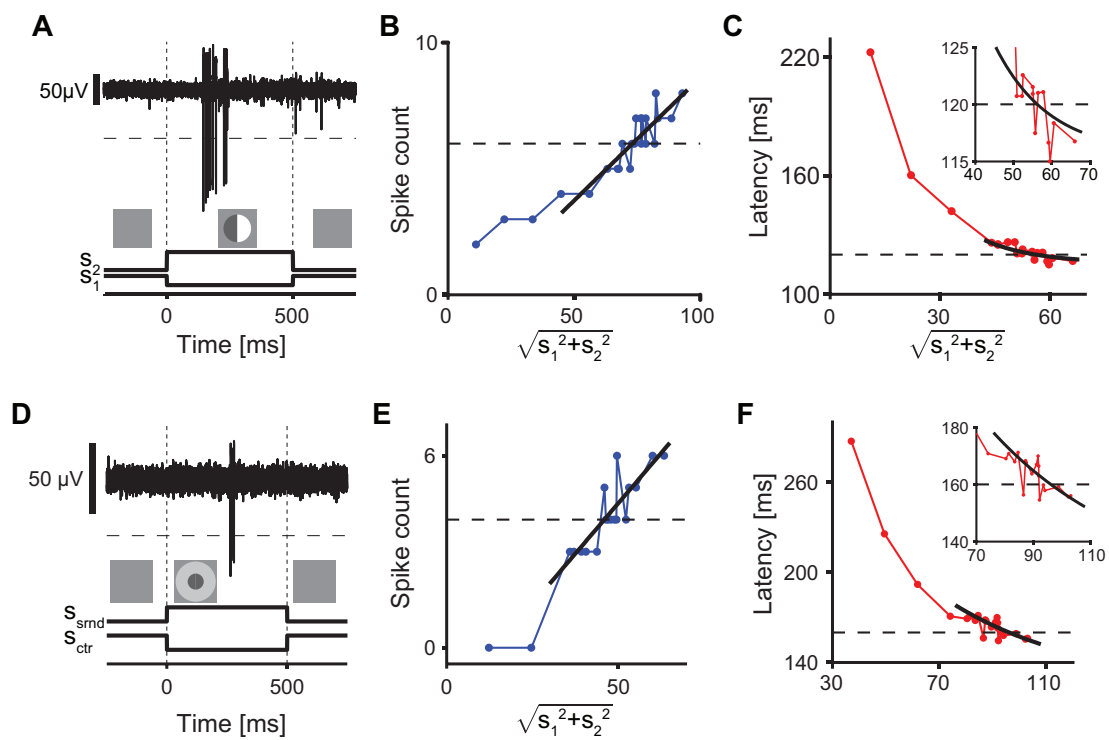


Figure 3.12: Measurement of iso-response curves. (A) Sample voltage trace recorded during an iso-response measurement with stimuli as shown in Fig. 3.9 A. (B) Search for a response of 6 spikes. (C) Search for a latency of 120ms. (D) Sample voltage trace recorded during an iso-response measurement with stimuli as shown in Fig. 3.9 B. (E) Search for 4 spikes. (F) Search for a latency of 140ms.

4. INTEGRATION IN THE RECEPTIVE FIELD CENTER

In this chapter, we present the first part of the results obtained from electrophysiological experiments performed on amphibian retinas. In particular, we study how the response of a single retinal ganglion cell is computed from the multiple inputs originating from photoreceptors within the receptive field *center*.

We will shortly summarize the essence of the previous chapters.

The basic assumption is that the retinal circuit can be approximated by a subunit model (Fig. 4.1 **A**, compare chapter 3.3), in which spatially separated stimuli are processed independently by receptive field subunits. The subunit outputs are subject to a nonlinearity $N(\cdot)$ before they are summed in the ganglion cell, where finally the spiking output is generated.

Thus, the nonlinearity $N(\cdot)$ is the hallmark of spatial integration and is what we attempt to determine. To this end, we restrict the visual stimulation only to the receptive field center of the ganglion cell. Thereby, we exclude additional effects mediated by a lateral signal flow generated in the receptive field surround. We stimulate both halves of the receptive field center separately. From a gray baseline stimulus, we independently update the intensity shown in each half (Fig. 4.1 **B**). The stimulus can be parameterized by the temporal contrasts s_1 and s_2 , defined as the intensity difference before and after switching on the stimulus in each half. The stimulus onset typically leads to a short burst of spikes in the ganglion cell.

To quantify the subunit nonlinearity, we measure iso-response curves. These consist of those stimuli (s_1, s_2) which lead to a certain pre-specified response on average. This can be either a certain number of spikes (iso-rate curve) or a certain first-spike latency (iso-latency curve). The closed-loop approach allows us to perform an online search algorithm. Thereby we can restrict the measurement only to those stimuli that lead to responses close to the pre-specified one.

In the following, we focus on salamander data only. Just in population data plots, or if indicated

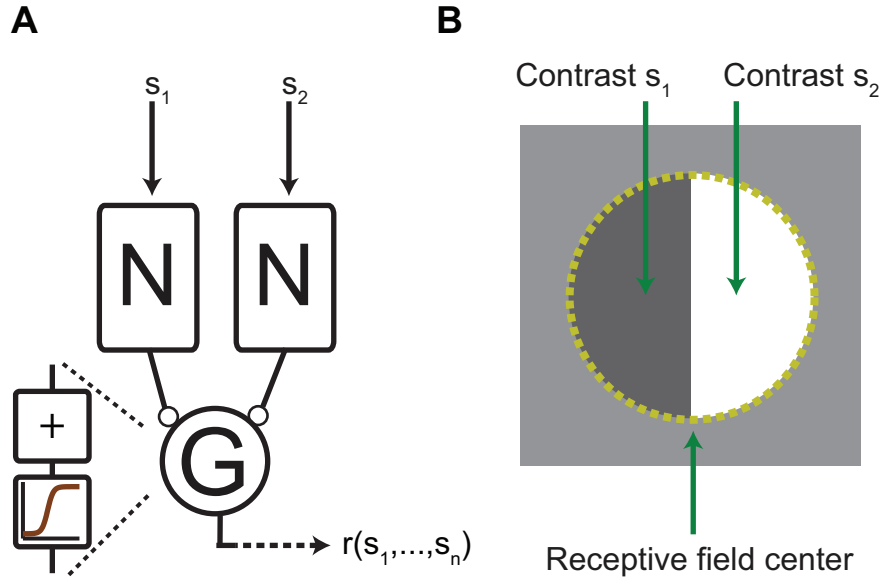


Figure 4.1: (A) Subunit model of the retinal circuit. (B) Stimulus used to determine potential nonlinearities $N(\cdot)$ by measuring iso-response stimuli in a closed-loop fashion.

otherwise, frog results are shown.

4.1 SPATIAL INTEGRATION IS NONLINEAR

We visualize the obtained iso-response stimuli in the two-dimensional stimulus space that is given by the contrast values in the two receptive field halves (Fig. 4.2 A). The vast majority of ganglion cells in the amphibian retina are dominated by OFF-type responses (Burkhardt et al. 1998, Geffen et al. 2007, Segev et al. 2006), and we therefore focused on OFF-type ganglion cells in this work. Figures 4.2 B-D show measured iso-response curves for three representative ganglion cells.

Iso-latency curves (red lines) always looked qualitatively similar. In particular, the curves were approximately parallel to the axes in those regions of stimulus space where one half of the receptive field experienced an increase in light intensity. This means that ON stimuli in one receptive field half hardly affected the latency; they were apparently cut off by a threshold non-linearity, providing half-wave rectification of the input signal. In some cells, this rectification occurred to be incomplete (Fig. 4.2 C). In these cases, bright contrasts weakly contributed to the cells' response by reducing the corresponding subunit signal.

In that region of stimulus space where both receptive field halves experienced negative contrast,

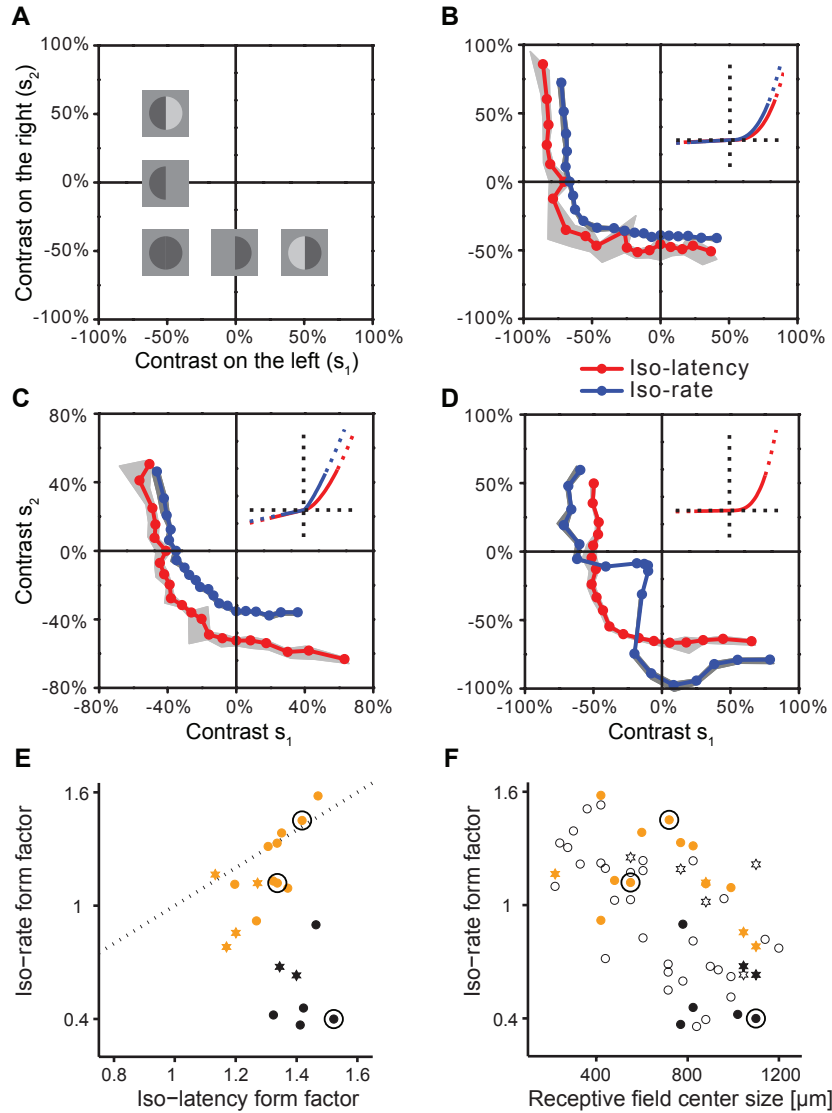


Figure 4.2: Iso-response curve analysis. (A) Illustration of the stimulus space. (B-D) Iso-rate (blue) and iso-latency curves (red) from three different ganglion cells. Predefined target responses were: 6 spikes and 170 ms (B); 4 spikes and 150 ms (C); 8 spikes and 120 ms (D). Insets show the corresponding nonlinearities obtained from a subfield model such as in Fig. 3.8 (see Methods). (E) Comparison of the shapes of iso-rate and iso-latency curves. Data are from salamander retinas (circles) as well as frog retinas (stars). Black symbols are used if the difference between iso-latency and iso-rate form factors is larger than 0.5, orange symbols otherwise. The data from the cells presented in (B-D) are marked by larger black circles around them. (F) Relation between iso-rate form factor and receptive field center size. Shapes and colors of symbols have same meaning as in (E). Small open symbols denote cells, for which only an iso-rate curve was measured, and which could therefore not be classified like the data presented in (E).

the iso-latency curves had an approximately circular shape. This indicated that two OFF stimuli were combined nonlinearly and that the nonlinearity approximately corresponded to a sum of squares. Indeed, we could fit the iso-response curves by a minimal model (Fig. 4.1) where each of the two input signals was transformed by a parameterized nonlinearity

$$N(x) = \begin{cases} m \cdot (x - \vartheta), & x \leq \vartheta \\ (x - \vartheta)^k, & x > \vartheta \end{cases} \quad (4.1)$$

before summation by the ganglion cell (see Methods in Appendix J.3 for details). x thereby denotes the *negative* contrast, i.e. $x = -s$.

In this model, ϑ denotes a threshold value. For contrast values $-s_i$ below ϑ , the nonlinearity describes an incomplete rectification (complete rectification is obtained for $m = 0$); for larger contrast values, the nonlinearity follows a simple power law, where $k = 2$ corresponds to the quadratic case.

We chose a power law nonlinearity rather than an exponential function because of its scale invariance. In this context, it means that the nonlinearity describes a certain shape of iso-response curve, independent of the magnitude of the input values s_i (see Appendix D for an example). The model was capable of describing the iso-latency curves very accurately (Fig. 4.3). As expected, the obtained nonlinearities approximately resembled threshold-quadratic functions (insets of Fig. 4.2 **B-D**, red lines): non-preferred signals were incompletely half-wave rectified, and preferred signals were exponentiated by an exponent usually much bigger than one before summation.

Iso-rate curves (Fig. 4.2 **B-D**, blue lines) displayed more variable shapes than iso-latency curves. For some cells, the iso-rate curve had approximately the same shape as the cell's iso-latency curve (Fig. 4.2 **B** and **C**), also indicating a nonlinearity of stimulus integration that is approximately threshold-quadratic or sometimes rather threshold-linear (insets of Fig. 4.2 **B** and **C**, blue lines, Fig. 4.3). These simple nonlinear characteristics were found for 25 of 45 of the recorded ganglion cells.

For other ganglion cells, however, the iso-rate curves displayed a notably different shape (Fig. 4.2 **D**), characterized by a notch along the lower-left diagonal. This notch gave the curves a distinctive non-convex shape. It showed that relatively little contrast was required for these cells to achieve the predefined spike count when both receptive field halves were stimulated with similar (negative) contrast. Stimulation of only one receptive-field half, on the other hand, required much larger contrast values. Thus, when considering the firing rate, these ganglion cells displayed exceptional sensitivity to homogeneous stimulation of the receptive field, and in the following we will therefore refer to these cells as homogeneity detectors.

Note that we found the same two types of iso-rate curves in frog retinal ganglion cells (Fig. 4.4).

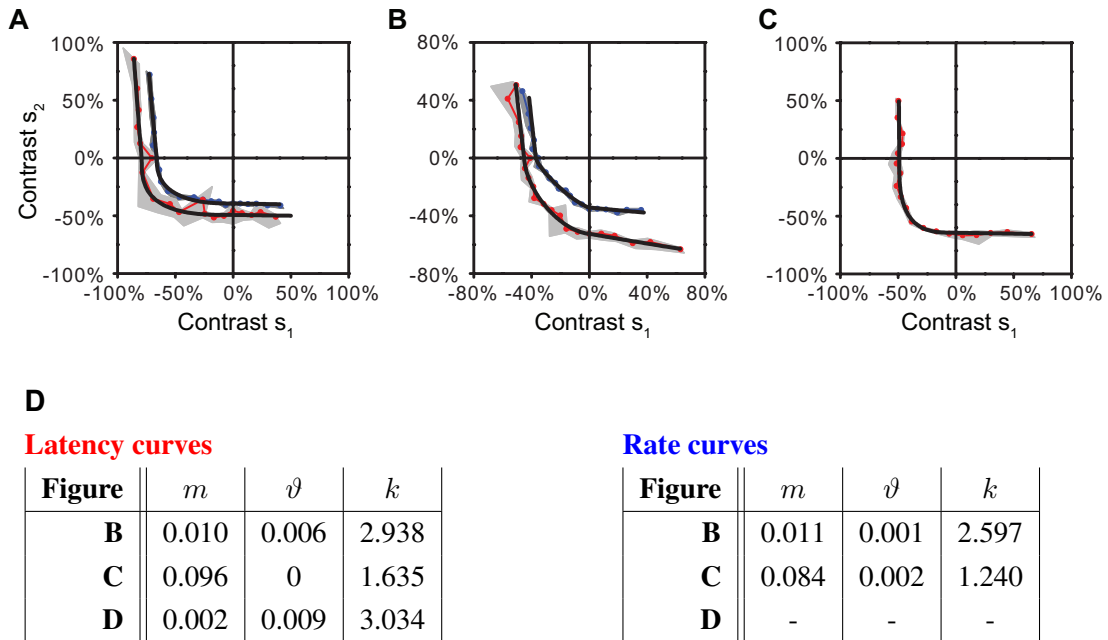


Figure 4.3: Model fits of iso-response curves. (A-C) The same iso-response curves of Fig. 4.2 B-D shown together with calculated curves (black) obtained from the fitted model. (D) Resulting parameters of equation (4.1).

It turned out that the non-convex curves of homogeneity detectors could not be well modeled by assuming a nonlinearity as in equation (4.1). Therefore, and because later experiments suggest that these curves were generated by dynamic processes rather than a static nonlinearity, we do not show fitting results from homogeneity detectors in Fig. 4.3.

Clearly, stimulus integration in the receptive field center of amphibian retinal ganglion cells deviated from linearity for all measured cells. To characterize the nonlinearity in the population data, we compared the radius of each iso-response curve along the direction where both receptive field halves were stimulated with the linear prediction derived from the two radii of the curve when each of the two halves were stimulated alone (Fig. 4.2 E). We calculated a form factor as the ratio of the measured radius and the linear prediction (see Methods in Appendix J.4). We found that the form factor for iso-latency curves is always larger than unity, confirming the approximately quadratic integration of preferred stimuli. Form factors of iso-rate curves, on the other hand, were similar to those from the iso-latency curves for many cells (Fig. 4.2 B and C), but much smaller than iso-latency form factors for others (Fig. 4.2 D) which corresponded to non-convex curves that were then classified as homogeneity detectors.

Homogeneity detectors were not a rare exception in our recordings; about 20 of 45 ganglion cells displayed the characteristic non-convex iso-rate curve that distinctly differed from the

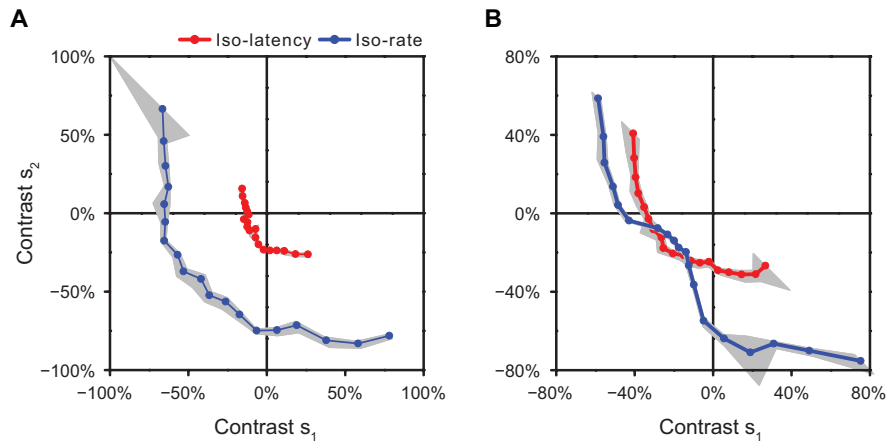


Figure 4.4: In frogs, the same types of iso-response curves as in salamander were found. (A) Iso-response curves from a cell with convex iso-rate curve. Target responses 15 spikes (blue), 130 ms (red). (B) Iso-response curves form a homogeneity detector. Target responses 21 spikes (blue), 110 ms (red).

cell's iso-latency curve. Interestingly, these cells were also characterized by a rather large receptive field center (Fig. 4.2 F) and by showing little or no antagonistic surround when stimulated with dark spots of increasing size (Fig. 4.5). Furthermore, the shape of the iso-rate curve appeared to be a generic feature of homogeneity detectors, independent of the exact stimulus layout and of the predefined spike count. The curve's non-convex shape remained qualitatively the same for a wide range of different spike counts (Fig. 4.6 A). Only the notch became more pronounced for higher responses. The shape was also unchanged when decreasing the stimulation radius (Fig. 4.6 C, green curve). Because the smaller stimulus did not cover the whole receptive field homogeneously, much bigger contrasts were necessary to elicit the same response as under control conditions. This is the reason why the curve could only be measured for dark contrasts in both stimulus halves. The non-convex shape also remained for stimulus layouts with a gap between the two stimulus areas (Fig. 4.6 C, orange curve). All together, these findings indicate that homogeneity detectors may indeed constitute of a particular type of ganglion cells in the amphibian retina.

4.2 SPATIAL SCALE OF NONLINEARITIES

In order to search for the mechanisms underlying the observed nonlinear features of stimulus integration, we first probed the spatial scale at which these occur. To this end, we spatially interleaved the two stimulus components by arranging them in a checkerboard fashion with various sizes of the checkerboard squares. We then measured iso-response curves for these

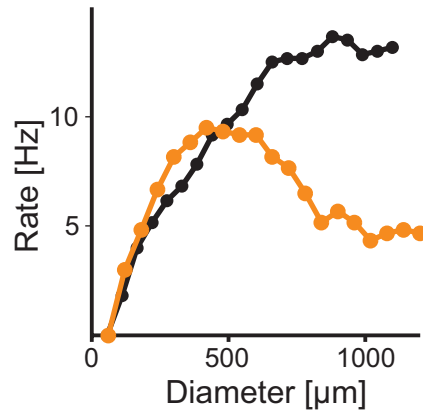


Figure 4.5: Receptive field size estimation. The structure of the receptive field was determined using a stimulus comprising a blinking circular spot of increasing size. For two different cells (black and orange), the resulting firing rate is shown in dependence on the spot diameter. The orange curve, belonging to a cell with convex iso-rate curve, reached a maximum and decreased for bigger diameter, indicating the presence of an antagonistic surround. The black curve, belonging to a homogeneity detector, did not reveal an antagonistic surround.

interleaved stimulus components. We found that stimulus integration generally became linear if the squares were sufficiently small (Fig. 4.7); the thresholding of non-preferred positive contrasts disappeared in iso-rate and iso-latency curves (Fig. 4.7 A-C), and homogeneity detectors lost the non-convex shape of their iso-rate curves (Fig. 4.7 B). These data are consistent with a subunit model (Crook et al. 2008, Enroth-Cugell and Freeman 1987, Hochstein and Shapley 1976, Victor 1988), in which the receptive field is composed of linear subunits whose outputs are nonlinearly combined.

By measuring how the level of half-wave rectification depended on the size of the stimulus squares, we estimated the spatial scale of the subunits to be around 100 μm (Fig. 4.7 D). The quantity used to characterize the degree of rectification is the averaged slope of iso-response curves in the regions with $s_1 \geq 0$; $s_2 < 0$ or vice versa (see Appendix J.5). A slope of zero indicates that the curve is parallel to the axis in these sections, thus labeling perfect rectification. A slope of one, on the other hand, refers to a linear integration, in which each increase of positive contrast has to be counterbalanced by an equally large negative contrast to obtain the same response.

For a more quantitative analysis, we reproduced this experiment *in silicio* (see Appendix E). To this end, we used a retinal model in which the ganglion cell receptive field consisted of circular subunits. Each subunit transformed its respective input by a rectifying-quadratic function with incomplete rectification. This model allowed us to compute iso-response curves in the same

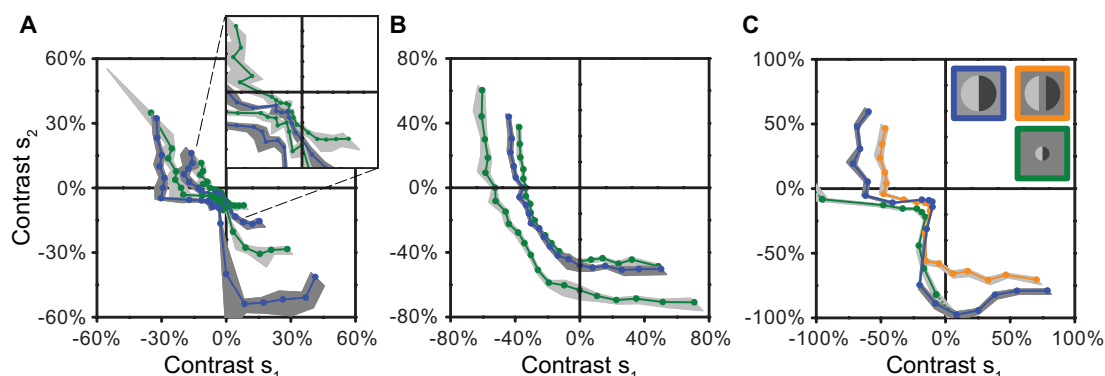


Figure 4.6: Dependence of iso-rate curves on spike count and stimulus layout. **(A)** Iso-rate curves of a homogeneity detector for different target responses. Target responses from inside to outside: 3, 4, 5, and 6 spikes. All curves showed the characteristic non-convex shape, although the inward notch became shallower with decreasing spike count. **(B)** Iso-rate curves for a ganglion cell with convex iso-rate curves. Target responses from inside to outside: 3, 4, and 6 spikes. **(C)** Iso-rate curves of a homogeneity detector for different stimulus layouts. The iso-rate curve obtained under control conditions (blue, target response of 8 spikes) is compared to a measurement where the two stimulus areas were separated by a 100 μm gray bar (orange, 6 spikes) and to a measurement where the stimulus diameter was reduced by 60% (green, 3 spikes).

way as we measured curves in the experiment. In particular, we determined the dependence of the iso-response curves' slope on the size of the checkerboard squares. The model allowed us to measure this dependence assuming different sizes of the subunit receptive fields. In Fig. 4.8, we compare the results to the experimental data.

The model confirmed that the experimental data could be reproduced by assuming subunit diameters between 50 μm and 150 μm . Subunits smaller than 20 μm , on the other hand, were not consistent with the data. This indicates that the nonlinearities do not occur on the level of photoreceptors, which have even smaller sizes (Mariani 2008, Sherry et al. 1998). Rather bipolar cells, which provide the direct excitatory drive to ganglion cells, are an obvious candidate for the subunits. These cells' receptive fields are known to have the desired sizes (Baccus et al. 2008, Hare et al. 1986, Wu et al. 2000). Indeed, nonlinear signal transmission from bipolar cells has been suggested to contribute to nonlinearities in ganglion cell receptive fields (Baccus et al. 2008, Demb et al. 2001, Gollisch and Meister 2008, Molnar et al. 2009, Ölveczky et al. 2003) and may thus underlie the threshold-quadratic nonlinearity apparent in the iso-latency curves and in many of the iso-rate curves.

Note that a common feature of basically all but one measured cells in salamander and frogs was the absence of any signature of excitation triggered by ON stimuli. Such inputs would

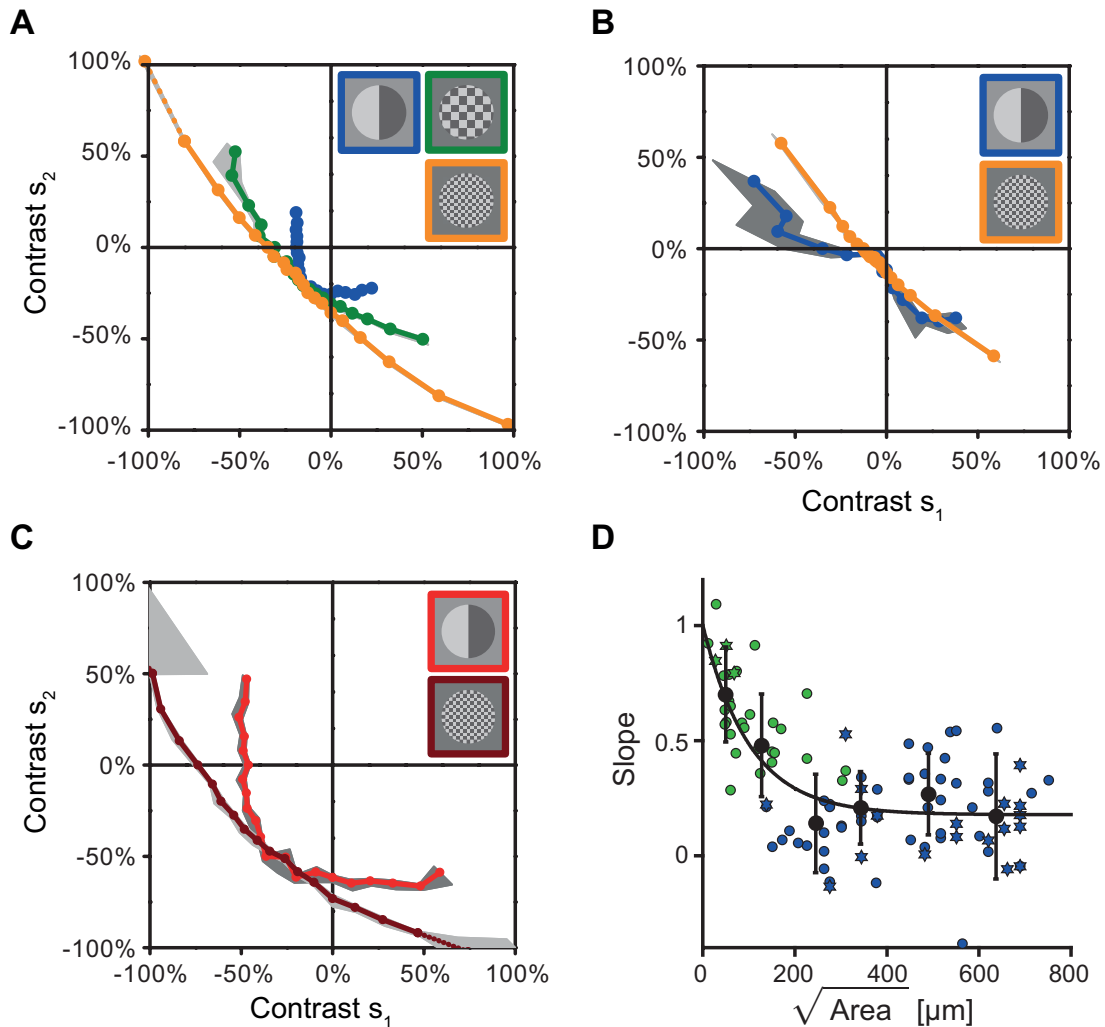


Figure 4.7: Estimation of the subunit receptive field size. (A) Iso-rate curves for control conditions (blue) and for two checkerboard arrangements of the two stimulus components with edge length of the squares of $150 \mu\text{m}$ (green) and $60 \mu\text{m}$ (orange). Target response: 4 spikes. (B) Analogous to A, but for a cell with a non-convex iso-rate curve under control conditions. Orange curve: checkerboard arrangement with edge length of $75 \mu\text{m}$. Target response: 6 spikes. (C) As in A, but for an iso-latency curve. Dark red curve: checkerboard arrangement with edge length of $120 \mu\text{m}$. Target response: 170 ms. (D) Dependence of rectification on spatial scale (I). Thereby, the spatial scale is given by the square root of the area of the stimulation subunits. The solid curve shows an exponential fit to the data, yielding a decay constant of $101 \mu\text{m} \pm 25 \mu\text{m}$ (90% confidence interval). Data are from salamander (circles) as well as frog retinas (stars).

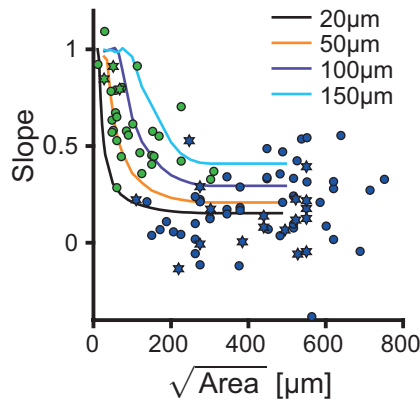


Figure 4.8: Dependence of rectification on spatial scale (II). The average level of response linearization when using checkerboard stimuli of different sizes was calculated in a computational model (see Appendix E). We did this assuming four different subunit diameters (black: 20 μm , dark blue: 50 μm , purple: 100 μm , light blue: 150 μm). When using 20 μm subunits, as an upper bound for photoreceptors, much finer checkerboard stimuli were necessary to linearize the responses than observed experimentally (green points). The amphibian data (salamander: circles; frog: stars) were better reproduced by subunits with diameter between 50 μm and 150 μm , corresponding to the receptive field size of bipolar cells. In blue, the level of rectification in response to a regular stimulus is shown to give a natural baseline.

correspond to a u-shaped subunit nonlinearity, or to a distinctly negative slope of the control iso-response curves as determined above (Fig. 4.8, blue markers). This finding is interesting, because we explicitly did not exclude OFF cells with biphasic temporal STAs, as might result from additional ON input. A possible explanation is that ON bipolar cells might connect to ON-OFF ganglion cells only in the receptive field surround (Sagdullaev and McCall 2005), and thus are not stimulated in the present experiments.

4.3 SPIKE PATTERNS ALONG ISO-RESPONSE CURVES

Static nonlinear signaling of bipolar cells cannot explain the surprisingly different shapes of iso-rate and iso-latency curves for homogeneity detectors. This is because a static nonlinearity should affect rate and latency both in the same way. To investigate this further, we measured iso-response curves and then chose three characteristic points on the curves for repeated measurements. These points corresponded to homogeneous dark stimulation and dark stimulation of only one of either side. All three stimuli were presented in a randomized fashion. This let us obtain an accurate picture of the temporal response profiles (Fig. 4.9).

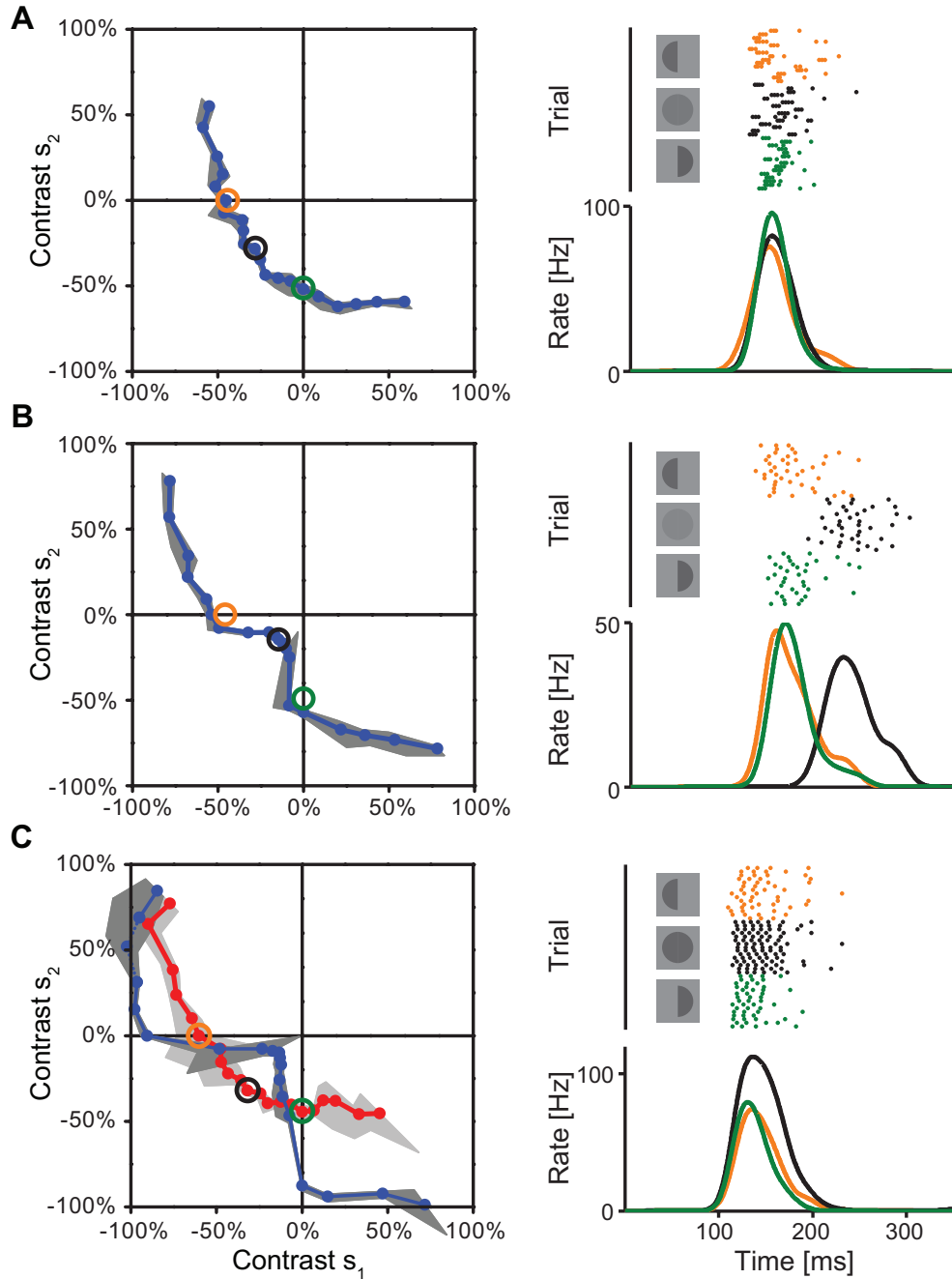


Figure 4.9: Temporal response profiles. (A) Iso-rate curve (left) and spike responses for three selected stimuli (right) of a ganglion cell with a convex iso-rate curve. Open circles along the iso-rate curve denote three stimulus patterns, which were used for repeated measurements. Raster plots on the right show spikes from 15 repeats of each of the three stimuli. Peri-stimulus time histograms are shown below. (B) As (A), but for a homogeneity detector with non-convex iso-rate curve. (C) As (B) for a second homogeneity detector, but measured for three iso-latency stimuli.

However, this experimental paradigm somewhat differed from the measurement of iso-response curves. Here, three rather strong stimuli consisting of only dark contrasts were shown consecutively. In contrast, during the iso-response measurement, such stimuli were interspersed with stimuli that were weaker and consisted of both bright and dark contrasts. Hence, the state of adaptation of the investigated ganglion cell might have been modified. The consequence was that the repeated measurement of the stimuli impaired the iso-response condition. To compensate, we corrected the stimulus contrasts after showing 30 repetitions of each stimulus. This allowed us to reobtain the iso-rate or iso-latency condition. This is why, in Fig. 4.9 **B**, marked stimuli slightly deviate from the iso-rate curve.

For cells with similar iso-rate and iso-latency curves, we found that response patterns had virtually identical temporal structure along iso-rate curves (Fig. 4.9 **A**). For homogeneity detectors, on the other hand, responses to stimulation of half the receptive field (Fig. 4.9 **B**, orange and green) were faster, narrower, and more strongly peaked as compared to homogeneous stimulation of the full receptive field (Fig. 4.9 **B**, black). Correspondingly, for stimuli along an iso-latency curve, responses to half receptive field stimulation appeared truncated at the tail end (Fig. 4.9 **C**). Together, these observations suggest that homogeneity detectors were affected by a dynamic mechanism that suppressed ongoing ganglion cell activity when stimulation was strong and locally restricted rather than distributed over the whole receptive field. This mechanism may be thought of as a local gain control which becomes effective during the course of the spike burst. It is *local* in the sense that it regulates down responses of individual subunits independently.

4.4 MECHANISMS OF LOCAL GAIN CONTROL

A first candidate mechanism for local gain control in homogeneity detectors is synaptic depression at bipolar cell terminals. Indeed, bipolar cell signals can display substantial depression (Burrone and Lagnado 2000, Singer and Diamond 2006), which could truncate responses to strong local activation. When activation is distributed over more bipolar cells, on the other hand, as in the case of homogeneous receptive field activation, synaptic depression is likely to be less effective and thus permit longer spike bursts. We therefore tested whether homogeneity detectors are cells with particularly strong local adaptation, as would result from synaptic depression. To do so, we used a stimulus that aimed at pre-depressing synapses in one half of the receptive field. We assessed the effect of this pre-depression on the iso-rate curves by a brief activation of one receptive field half shortly before each stimulus of the iso-rate-curve measurement (Fig. 4.10 **A**, Appendix J.6).

As expected, the pre-depression stimulus reduced sensitivity of the ganglion cells, which is

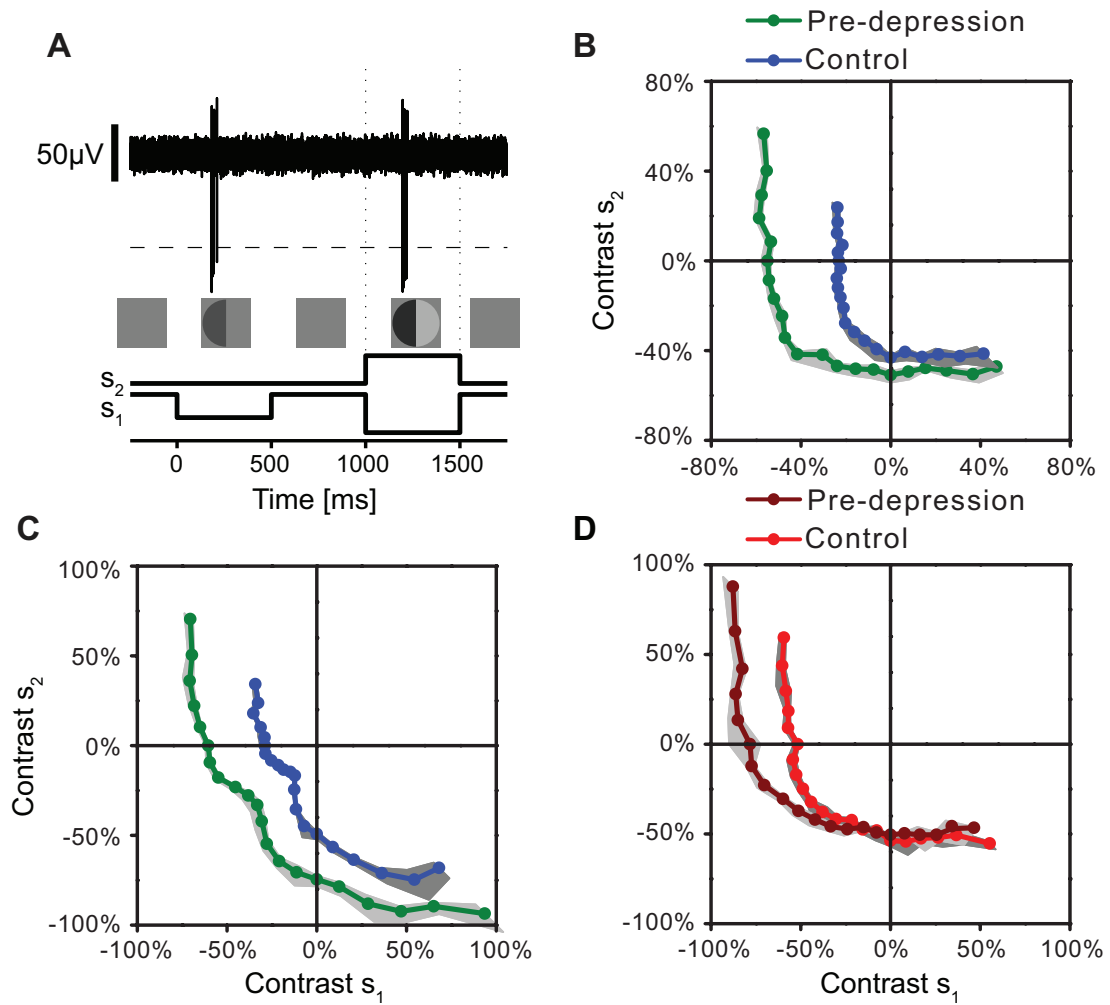


Figure 4.10: Assessment of the role of contrast adaptation. (A) Sample recording trace and stimulus layout. The actual iso-response stimulus was preceded by a fixed pre-depression stimulus (contrast = -40%) presented on one half of the receptive field. (B) Results for a cell with convex iso-rate curve under control conditions (blue) and in the presence of the pre-depression stimulus (green). Target response: 4 spikes. (C) Same as B, but for a homogeneity detector with non-convex iso-rate curve. Target response: 6 spikes. (D) Same as B, but for an iso-latency curve. Target response: 170 ms.

reflected by the increased radius of both iso-rate (Fig. 4.10 **B** and **C**, green lines) and iso-latency curves (Fig. 4.10 **D**, dark red line) as compared to the control condition without the pre-depression stimulus (blue lines or red line, respectively). The reduction in sensitivity may contain both global and local components; a symmetric scaling of the pre-depressed iso-rate-curve radius along all directions reflects a global loss in sensitivity, whereas an asymmetric scaling provides evidence for a local loss in sensitivity and thus a local adaptation mechanism. If the non-convex iso-rate curves of the homogeneity detectors were to result from particularly strong synaptic depression, this asymmetric scaling should be particularly strong for these cells. To demonstrate this, we created a computational model of a retinal circuit with strong synaptic depression (Appendix F). However, this expectation was not supported by the experimental data. In fact, homogeneity detectors typically displayed rather global adaptation effects and less local sensitivity loss (Fig. 4.10 **C**) than cells with a convex iso-rate curve (Fig. 4.10 **B**). Synaptic depression is thus not a plausible mechanism for the particular features of homogeneity detectors.

As an alternative model, we therefore explored whether local inhibitory signaling could mediate a local gain control. To test the role of inhibition, we pharmacologically blocked all inhibitory synaptic transmission in the retina and then repeated the measurement of the iso-rate curve. The inhibition block had a dramatic effect on the iso-rate curves (Fig. 4.11 **A**). First, it strongly reduced the radius of the iso-rate curves, corresponding to an overall increase in sensitivity, as expected from the general lack of inhibition. Second, it gave the iso-rate curves of homogeneity detectors a convex shape similar to the typical iso-response curves of other ganglion cells (Fig. 4.2 **B** and **C**). This effect has been observed in four homogeneity detector cells, two of which are shown. The transition from a non-convex to a convex shape upon inhibition block is also apparent when calculating the form factors of these cells (Fig. 4.12), similar as done in Fig. 4.2 **E** and **F**. All factors change from values smaller than one, characterizing a homogeneity detector, to values bigger than one, thus characterizing a regular convex curve.

The loss of the non-convex shape of the iso-rate curve is not a result of the reduced contrast level in these inhibition block experiments. When we decreased the radius of the stimulation area in order to reduce the effectiveness of the applied stimuli, the required contrast levels returned to the range of the control experiment, but the iso-rate curves still remained convex under the inhibition block (Fig. 4.11 **B**). Note that simply reducing the stimulation area without inhibition block did not affect the non-convex shape of the iso-rate curves (Fig 4.6 **C**). We thus conclude that local inhibitory signaling is responsible for the non-convex shape of the iso-rate curves of homogeneity detectors.

We also tested if the retinal ON pathway is responsible for the non-convex shape of homogeneity detector iso-rate curves via crossover inhibition (for review, see Werblin (2010)). Therefore

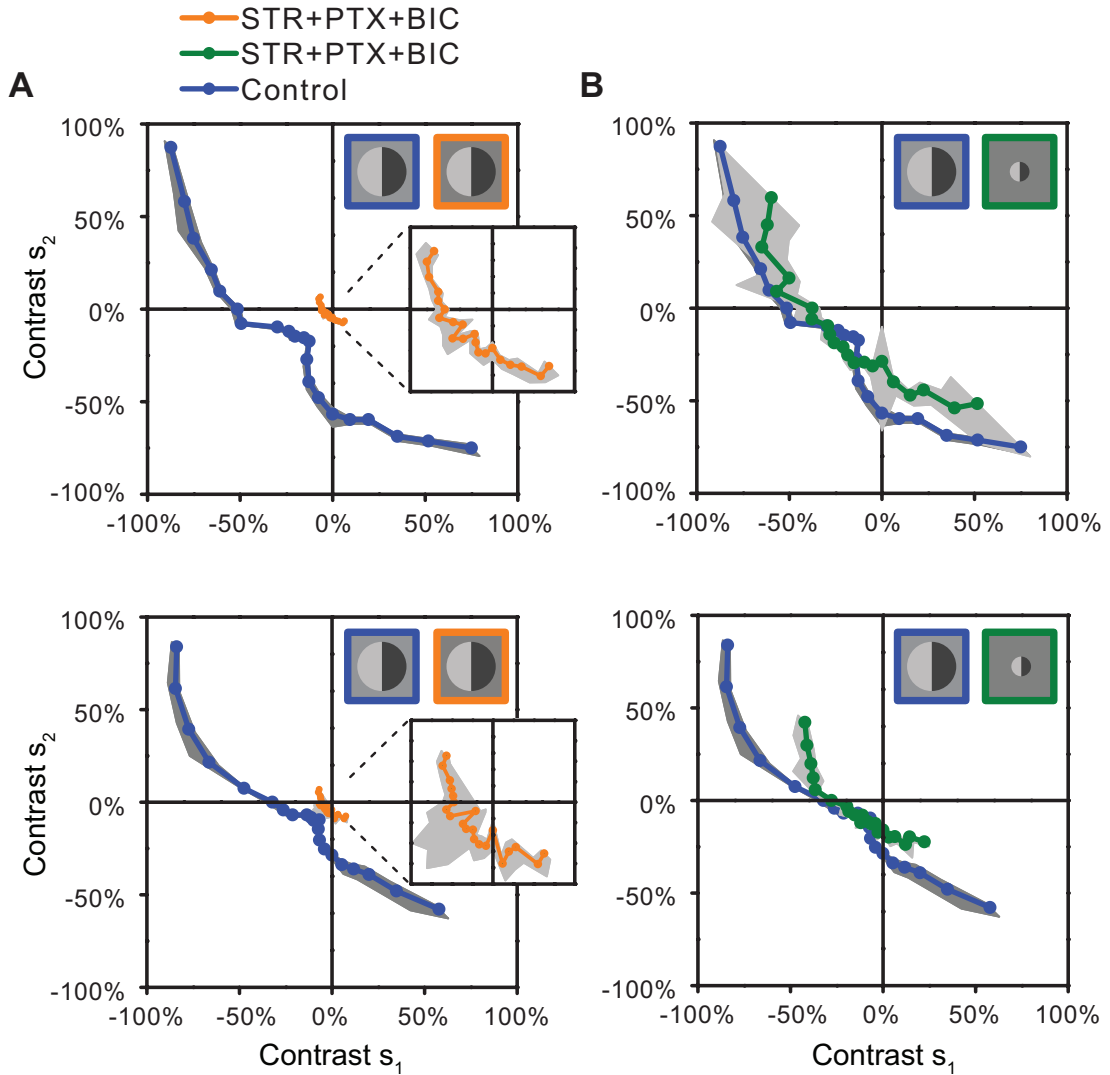


Figure 4.11: Inhibition-block experiments. **(A)** Iso-rate curves for two different homogeneity detectors under control conditions (blue) and in the presence of a pharmacological block of inhibition (orange). Iso-rate curves became convex when inhibition was removed from the circuit. Target response: 6 spikes for all curves. **(B)** Iso-rate curves for the same cells as in (A), but with reduced stimulation area under the inhibition block (green). Target responses: 8 spikes (top) and 6 spikes (bottom). Control curves (blue) are the same as in (A).

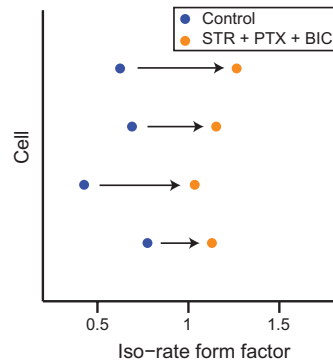


Figure 4.12: Change of the iso-rate form factor upon inhibition block. For every Homogeneity detector, the form factor changed from a value smaller than one to a value bigger than one upon inhibition block. This clearly indicates the transition from an iso-rate curve of non-convex shape, as characteristic for a homogeneity detector, to a convex curve.

we pharmacologically abolished inputs to ON bipolar cells by blocking metabotropic glutamate receptors mGluR6 using APB (Slaughter and Miller 1981, Nakajima et al. 1993) and then remeasured iso-rate curves (Fig. 4.13). We found no significant change, neither in convex iso-rate curves (Fig. 4.13 **A**) nor in non-convex curves of homogeneity detectors (Fig. 4.13 **B**). Thus, the contrast gain control mechanism seems to be independent of ON path signaling.

This leads us to a simple circuit model for homogeneity detectors (Fig. 4.14): They receive excitatory input from bipolar cells, which have smaller receptive fields and therefore constitute the subunits. The bipolar cell signals undergo a threshold-quadratic nonlinear transformation before they are pooled by the ganglion cell. In addition, the bipolar cells activate local amacrine cells, which provide inhibition either directly to the ganglion cell or as feedback to the bipolar cells. This inhibition must have a high threshold or be otherwise nonlinear so that it becomes relevant only for strong local activation. Furthermore, the inhibition must be delayed compared to the excitatory input into the ganglion cell so that the timing of the first spike of the ganglion cell response remains unaffected. We simulated this model (Fig. 4.14, iso-response curves) assuming that the amacrine cell acts as a low-pass filter with a rectifying-quadratic output nonlinearity (see Methods in Appendix J.7 for details). The generated inhibition then acts subtractive on the excitatory bipolar cell output. Another possible implementation of this circuit, which relies on divisive shunting inhibition (Holt and Koch 1997, Doiron et al. 2001, Dayan and Abbott 2001), is discussed in Appendix G.

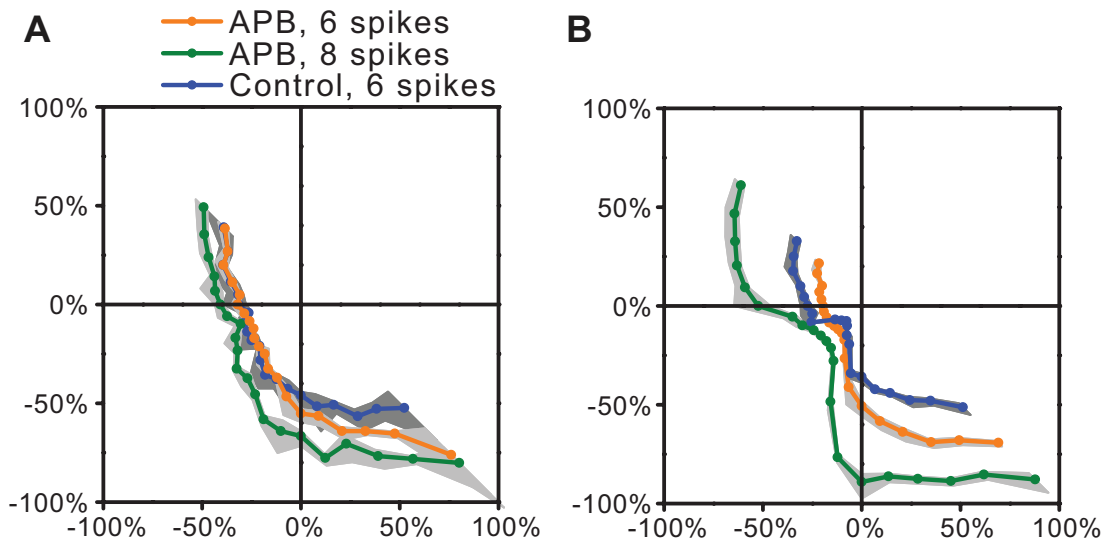


Figure 4.13: Iso-rate curves with and without pharmacological block of the ON path. After APB (200 μM) was added to the Ringer solution, the retina was rested for 20 min for the drug to take effect. Responses to full field black-white-blinks recorded before and while drug application were compared to verify that the drug is blocking the retinal ON path as intended. **(A)** Results of a cell with convex iso-rate curve under control conditions (blue, control). When blocking the ON path, the shape of the curves remained unchanged. **(B)** Results of a homogeneity detector. Also here, the non-convex shape of the iso-rate curve remained unchanged under APB. Hence, in both cases APB did not significantly alter the shape of the iso-response curve, indicating that neither the rectification of nonpreferred signals nor the notch of iso-rate curves in homogeneity detector cells depend on ON path signaling.

4.5 FUNCTIONAL CONSEQUENCES FOR STIMULUS INTEGRATION

The striking differences between different ganglion cells in the nonlinearities of signal integration raise the question of the associated visual functions. To illustrate the effects of the observed receptive field nonlinearities, let us therefore consider a simple visual stimulus, which contains a large dim object as well as a group of several small objects at high contrast (Fig. 4.15 A). When viewed through linear receptive fields, both the large dim object and the area with the small high-contrast objects appear equally prominent (Fig. 4.15 C). Receptive fields that integrate their subfields with a threshold-quadratic nonlinearity, however, emphasize the high-contrast region (Fig. 4.15 D), whereas the nonlinear integration of the homogeneity detectors facilitates the detection of the large dim object while being insensitive to high-contrast clutter (Fig. 4.15 E). This suggests that homogeneity detectors contribute particularly to the detection of large objects.

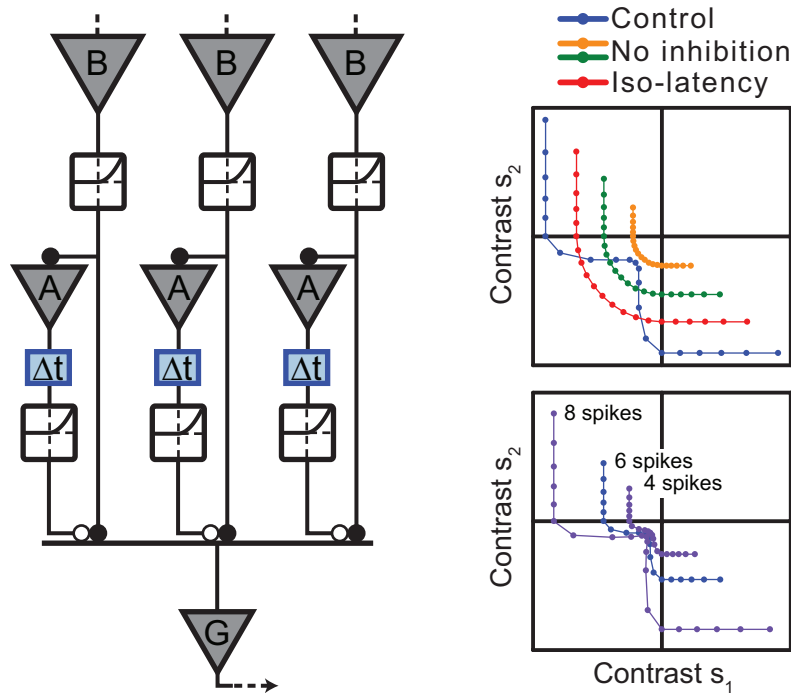


Figure 4.14: Circuit model for homogeneity detectors. Bipolar cells (B) are assumed to represent contrast in a linear fashion. Their output undergoes a threshold-quadratic nonlinearity and excites the ganglion cell (G) as well as narrow-field amacrine cells (A). The inhibition provided by the amacrine cells is subject to a threshold-quadratic nonlinearity and is delayed in time compared to the excitation. Model results are shown on the right.

4.6 DIFFERENT CELL TYPES AND SPECIES

So far, our whole investigation focused solely on amphibian OFF ganglion cells. In the course of the project, only three times an ON cell was found and used for iso-response measurement (Fig. 4.16 A). All those curves revealed threshold-quadratic nonlinearities, similar to those we found to underly spatial integration the majority of OFF cells. However, no ON equivalent to a homogeneity detector cell was found.

Furthermore, rare attempts were made to measure iso-response curves in mouse¹ retinas. Being a mammalian system, the mouse retina is closer to human physiology and is therefore of special interest. Unfortunately, due to high spontaneous activity in mouse retinal ganglion cells, we did not succeed to measure iso-latency curves. Also the measurement of iso-rate curves was subject to a higher distortion. This is due to the peculiar effect that spontaneous activity often

¹*Mus musculus*, strain C57Bl6

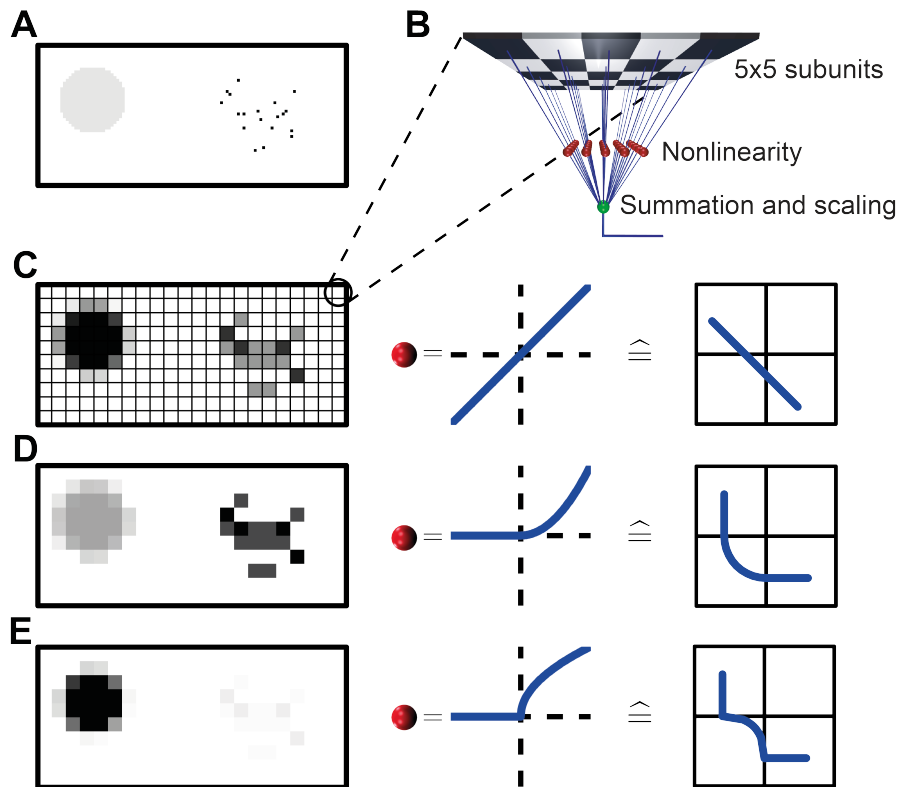


Figure 4.15: Consequences of different subunit nonlinearities on image perception. (A) Sample image, consisting of a large homogeneous low-contrast object and a region with multiple small high-contrast objects. (B) Model of ganglion cell processing of the image. The image is tiled by the spatial receptive fields of an array of identical ganglion cells. Each ganglion cell's receptive field is divided into a 5x5 matrix of spatial subunits. The subunits are "Off-type" and linearly integrate the stimulus in their receptive field regions. Their outputs are passed through a nonlinearity and summed by the ganglion cell. In the following image reconstructions, white pixels correspond to a ganglion cell output of zero spikes, and black pixels correspond to the maximum ganglion cell spike count. (C) Image reconstruction with linear summation of subunit activity (left) and corresponding iso-response curve (right). (D) Image reconstruction with a threshold-quadratic nonlinearity applied to the subunit signals (left) and corresponding iso-response curve (right). The region containing small high-contrast objects is amplified. (E) Image reconstruction with a subunit nonlinearity composed of a threshold and a square-root transformation (left). This nonlinearity is used to qualitatively model the effect of the non-convex iso-rate curve (right) when the iso-latency curve is not considered. Now, the region of the homogeneous low-contrast object is amplified.

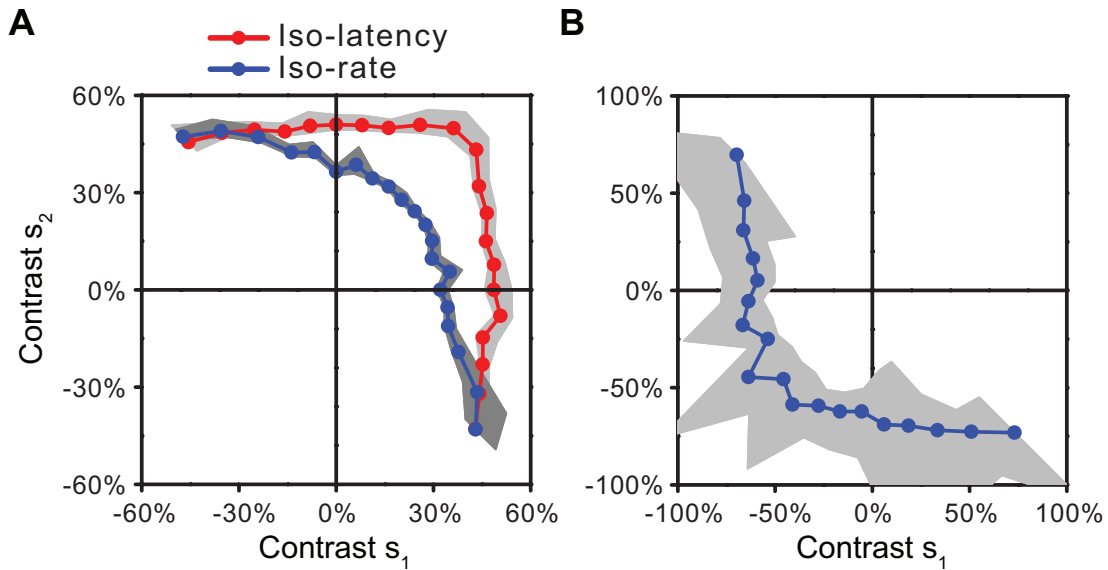


Figure 4.16: Iso-response curves in different cells and species. **(A)** Iso-response curves from a salamander ON cell. Target responses: 6 spikes; 180 ms. **(B)** Iso-rate curve from a mouse retina OFF cell. Target response: 10 spikes. Because of high spontaneous activity, the error of the measurement is increased compared to curves measured in amphibian ganglion cells.

silences after strong cell activation. Thus the firing rate is first increased by a preferred stimulus and subsequently decreased before it relaxes back to the maintained rate. When integrating the rate over a fixed time interval, these opposing effects tended to partly cancel out and thus obstruct the measurement. Therefore, for a cell with high spontaneous activity, it might be better to choose an alternative response feature than the overall number of spikes, such as the peak firing rate in an interval extending several hundreds of milliseconds after the stimulation onset.

In the case of an OFF cell with a low maintained firing rate we once succeeded to measure an iso-rate curve (Fig. 4.16 **B**). This revealed the presence of threshold-quadratic nonlinearities also in this system.

4.7 ISO-RESPONSE RESULTS IN HIGHER DIMENSIONS

Until now, we characterized nonlinearities in spatial integration via the measurement of (one-dimensional) iso-response curves. Here we want to demonstrate that the method can be generalized to higher dimensions. To this end, we measured iso-response surfaces embedded in a three-dimensional stimulus space. This was done for a salamander OFF-center homogeneity

detector for which the conventional iso-response curve had been determined beforehand. We used a stimulus dividing the receptive field center into thirds (Fig. 4.17 **A**). Using the subunit model, we could predict how the iso-response surface should look like and thus chose the search angles in stimulus space adequately in order to get a good representation of the surface with few data points. Here we used 13 points, which is even less than the 21 point that typically constituted our iso-response curves.

The result² is shown in Fig. 4.17 **B**. The measurement was performed searching for 3 spikes per stimulus presentation, which is less than what we generally used for iso-response curves (mostly 4 to 8 spikes). This is because for some stimuli only one third of the receptive field center was stimulated. In contrast, when determining regular iso-response curves, at least one half of the center experienced a preferred stimulation.

The obtained surface showed all the effects we expected from the prediction of the subunit model. First, bright stimuli were rectified. Second, the necessary contrasts when stimulating only one third of the receptive field were highly increased. Third, when stimulating the whole receptive field center homogeneously, a notch in the surface indicated that in this case only little contrast was required to yield the aspired response of three spikes.

In summary, all the effects expected of a homogeneity detector could be recovered in a two dimensional iso-response surface. Furthermore, its determination did not take more time than the measurement of an iso-response curve. This leads us to the assumption that, also in general, iso-response measurements in higher dimensional stimulus spaces are feasible and useful tools to characterize neuronal systems.

In the next chapter, we shift gears and extend the analysis of nonlinear stimulus integration on contrasts stimulating both center and surround. Thereby, we investigate the effects of the so-called antagonistic surround on a functional level.

²To better visualize the manifold, it is necessary to use a 3d viewer which allows rotations of the surface. A video, which shows this plot rotating, can be requested at boelinger@neuro.mpg.de

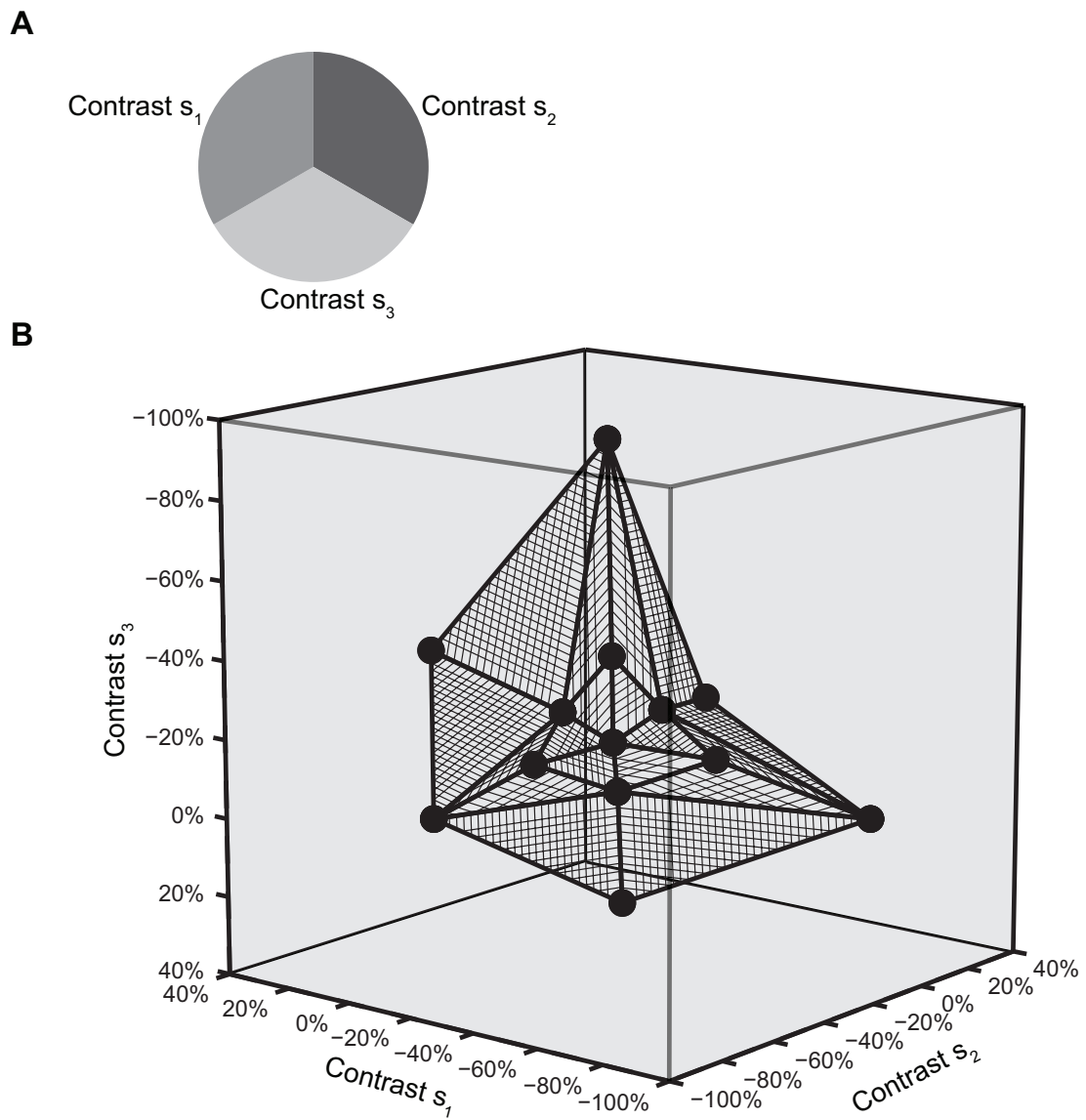


Figure 4.17: Three dimensional iso-response surface. (A) Stimulus layout. (B) Iso-rate surface of a homogeneity detector. Target response: 3 spikes.

5. CENTER-SURROUND INTEGRATION

In this chapter, we use the closed-loop method to address the second question of this thesis. Instead of determining the subunit nonlinearities in the ganglion cell receptive field center (chapter 4), we here investigate how stimuli shown in the surround affect the response of the retinal ganglion cell to stimuli in its center. Experimental data are obtained only from salamander.

First, we shortly summarize the basic facts and concepts discussed previously. Center-surround antagonism is a well known property of retinal receptive fields, already discovered by S. W. Kuffler (1953). Nevertheless, the exact mechanisms remain controversial until today. Although many pathways are known (Zaghloul et al. 2007, Ichinose and Lukasiewicz 2005), it is still not clear what the individual contributions are. Functionally, the center-surround structure of retinal ganglion cells is often described in the linear-nonlinear model, in which the spatial receptive field is usually approximated by the difference of two Gaussians (Dayan and Abbott 2001). This implies that the contributions of the center and the surround are integrated linearly with opposite sign. Especially, the surround in such a linear model is both suppressive upon equipolar stimulation, and responsive upon antipolar stimulation. In contrast, Enroth-Cugell and Freeman (1987) proposed a model in which the surround arises from a nonlinear combination of subunits. Each subunit thereby featured its own local center-surround structure. Also divisive (Merwine et al. 1995) effects of the surround have been proposed.

Here we attempt to elucidate center-surround antagonism from a new point of view. The goal is to probe to what extent the linearity of integration, as proposed by the LN model, holds true in amphibian retinal ganglion cells. To this end, we assess the strength of the surround signals in response to different stimulation contrasts. We do this using the iso-response approach. This allows us to ask a precise question: depending on the strength and sign of surround stimulation, how much preferred contrast has to be presented in the center to elicit a pre-specified response? As shown before in section 3.3, this method has the advantage of being independent of the cell's spike generation mechanism. Closed-loop measurements allow us to gain sufficient statistics for the relevant part of stimulus space.

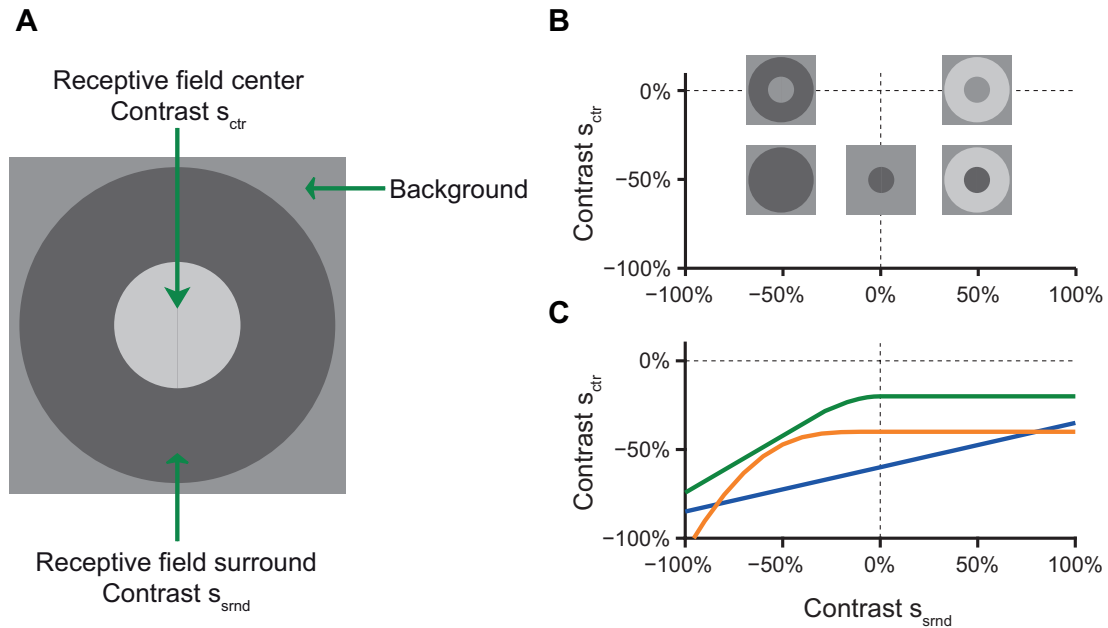


Figure 5.1: Investigation of center-surround integration. **(A)** Used stimulus. **(B)** Schematic of the stimulus space. **(C)** In case of linear integration of center and surround contrasts, as predicted by the LN model, the iso-response curve would resemble a straight line (blue). If rectifying quadratic nonlinearities are assumed in both center and surround, iso-response curves will display a piecewise hyperbolic shape (green). If stimuli in the center are subject to a rectifying-quadratic nonlinearity, while surround stimuli are transformed by a rectifying power of four nonlinearity, the orange curve will be the result.

We apply the iso-response paradigm in the following way. First, the size and position of the receptive field center is determined by an online procedure (chapter 3.4). In particular, the receptive field center size is defined by the diameter of the optimal spot, eliciting the maximum response upon alternating black-and-white blinking. The receptive field surround is taken as an annulus of fixed width around the center (Fig. 5.2). Second, we measure iso-response curves using a stimulus layout which consists of a contrast s_{ctr} presented in the center and a contrast s_{srnd} simultaneously presented in the surround (Fig. 5.1 A). The iso-response condition is given either by a fixed number of spikes (iso-rate curves) or a fixed first-spike latency (iso-latency curves), triggered by stimulus onset. An online search algorithm is applied in order to find all stimuli (s_{ctr}, s_{srnd}) which elicit the pre-specified response on average. We visualize the iso-response stimuli in the two-dimensional stimulus space given by the contrast values in the center and the surround (Fig. 5.1 B). Also in this chapter, we focus on OFF retinal ganglion cells. Compared to chapter 4, we modified the style of the error bars of iso-response curves to emphasize that iso-response curves now occur in a different context and have to be read differently.

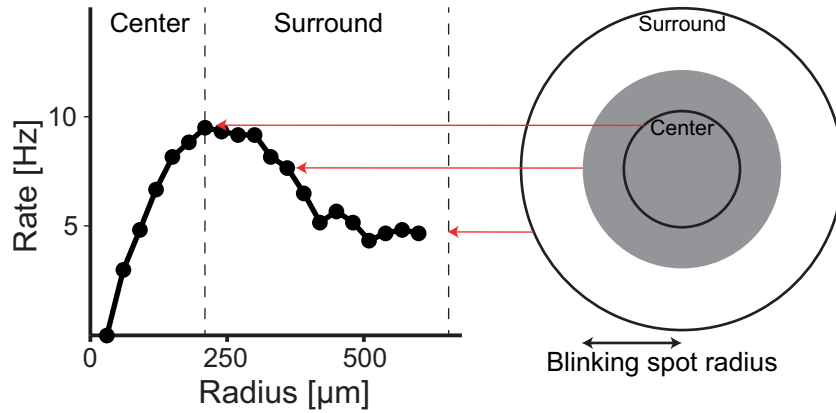


Figure 5.2: Receptive field size estimation. The structure of the receptive field has been determined using a stimulus comprising a blinking circular spot of increasing size. The receptive field center was defined by the diameter of the spot yielding the maximum response. The receptive field surround stimulation area was chosen as annulus of fixed width (approximately $450\mu m$ outside radius minus inside radius) around the center.

The underlying assumption is that subunits in center and surround process their individual inputs imposing different nonlinearities $N_{ctr}(s_{ctr})$ or $N_{srnd}(s_{srnd})$, respectively. The ganglion cell then pools both signals. Hence, the nonlinearities determine how center and surround contrasts are combined. Therefore, our goal is to study these nonlinearities. From the results in chapter 4, we already know that the majority of amphibian retinal ganglion cells derive their output by imposing a rectifying-quadratic transformation on the inputs to the receptive field center. Let us first assume a similar nonlinear processing in the surround as well as a summation of center and surround signals in the ganglion cell. In this case, one would expect iso-response curves as depicted in Fig. 5.1 C (green curve). Another likely assumption is that the inhibitory surround is generated by an amacrine cell with a rectifying-quadratic output nonlinearity (compare Fig. 4.14), which is in turn activated by a rectifying-quadratic bipolar cell. This will in sum give rise to a $|\cdot|_+$ -transformation of surround inputs (Fig. 5.1 C orange curve). In contrast, the center-surround integration could also occur purely presynaptically to the bipolar cell terminal, thus before the nonlinearities are imposed. Hence, a linear behavior would be the result. Iso-response curves then resemble straight lines (Fig. 5.1 C blue curve).

Note that the center and surround nonlinearities, as determined by the iso-response procedure, do not depend on whether the surround acts subtractive or divisive. In both cases, the iso-response condition can be formulated as $N_{ctr}(s_{ctr}) - N_{srnd}(s_{srnd}) = const.$ Hence, the iso-response methods allows us to measure the functional nonlinearities without requiring an assumption of a subtractive or divisive effect of the surround. Only if we determine iso-

response stimuli for several responses, we can conclude from the scaling of the curves about the specific type of integration (see Appendix H).

5.1 CENTER-SURROUND INTEGRATION IS NONLINEAR

If the contributions of the OFF-type center and the antagonistic surround are well described by a linear filter, one would expect an iso-response measurement to result in a linear curve with positive slope (Fig. 5.1 C blue curve): dark contrasts in the center and bright contrasts in the surround would be the preferred stimuli. These are integrated linearly to produce the cell's response. However, experiments performed on amphibian retinas yield iso-response curves that deviate substantially from this behavior (Fig. 5.3).

Iso-latency curves (Fig. 5.3 A-C red curves) did not indicate an antagonistic effect of the surround. For positive surround contrasts, iso-latency curves were approximately parallel to the x axis. This indicates that bright surround stimulation did not play a significant role in modifying the response latency; these signals were cut off. Most of the times, however, this rectification was not perfect. Curves were not exactly parallel to the axis, but displayed either a small positive or negative slope.

For negative surround contrasts, the curves had an approximately circular shape with negative slope. The darker the surround was stimulated, the less dark contrast needed to be shown in the center to yield the predefined response. Thus, dark surround contrasts were preferred stimuli, which acted latency reducing in the same way as dark center stimulation did. Apparently, the surround elicited excitation upon dark OFF stimulation. The circular shape supports the assumption of a roughly quadratic dependence of this excitation on the contrasts in center and surround.

For further verification, we performed a maximum likelihood estimate of the involved nonlinearities. The fit resulted in a model which provides an accurate description of the measured curve (Fig. 5.4 A). The obtained nonlinearities indeed show an incomplete rectification as well as a superlinear power-law behavior (Fig. 5.4 B and C, see Appendix J.8 for details).

In summary, iso-latency curves suggest that salamander retinal ganglion cells receive excitatory inputs from a rather homogeneous set of approximately rectifying-quadratic bipolar cells located both in center and surround.

Iso-rate curves (Fig. 5.3 blue and green curves) showed a very different behavior than iso-latency curves. They could be qualitatively sub-divided into four different regions spanning different surround contrasts (Fig. 5.3 A).

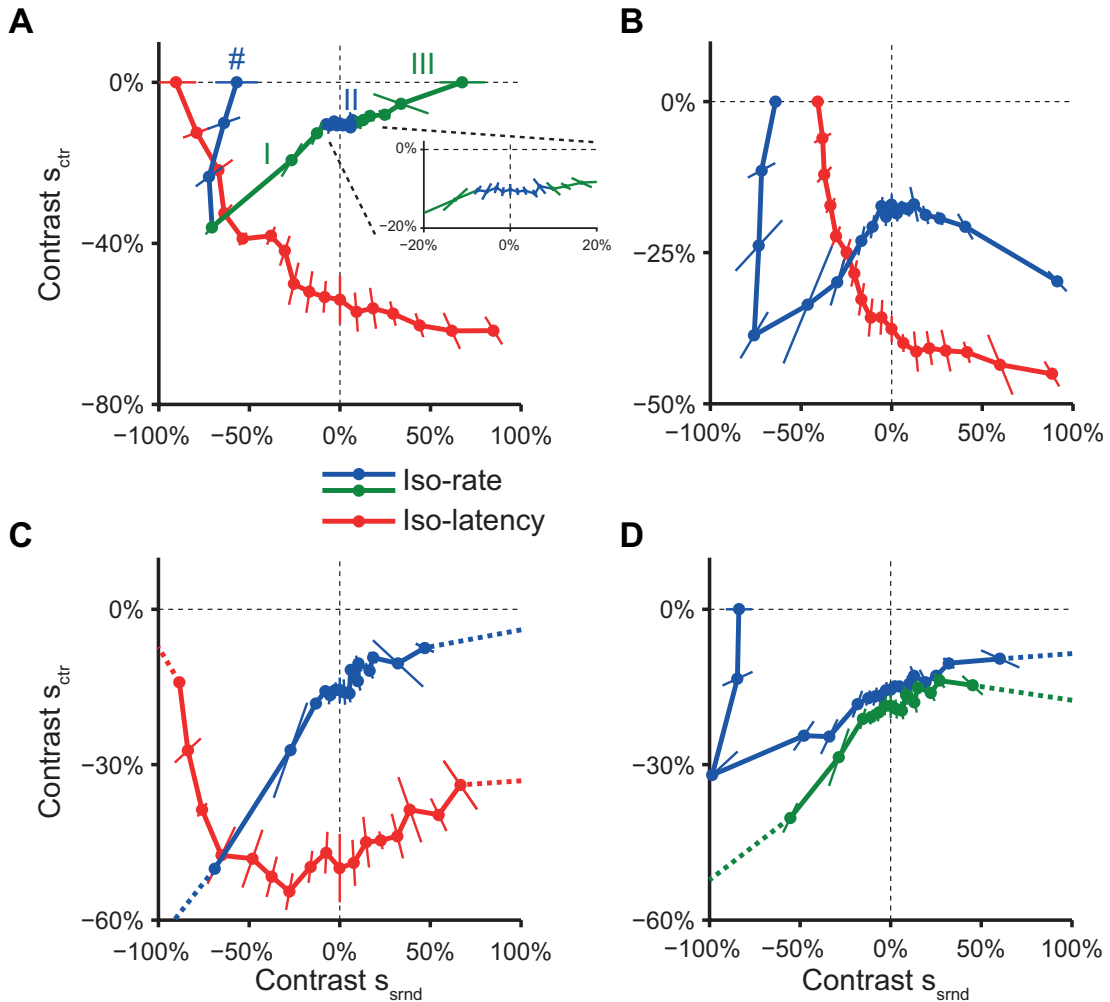


Figure 5.3: Iso-response curves of four different cells. **(A)** Iso-rate (3 spikes) and iso-latency curve (140 ms). Stimulus center diameter 420 μm . To visualize the four regions of an iso-rate curve, they are exemplarily colored alternating blue and green and labeled with roman numbers I - III and #. **(B)** Iso-rate curve (6 spikes) with negative slope for bright surround contrasts and iso-latency curve (160 ms). Stimulus center diameter 360 μm . **(C)** Iso-rate curve (4 spikes) without upsurge at very dark surround contrasts and iso-latency curve (140 ms). Stimulus center diameter 452 μm . This cell was classified as homogeneity detector by a separate experiment using the methods of chapter 4. **(D)** Two curves of one cell searching for different number of spikes elicited (blue: 3 spikes; green: 4 spikes). The iso-rate curve along which more spikes were elicited does not show an upsurge for very strong dark stimulation. Stimulus center diameter 730 μm .

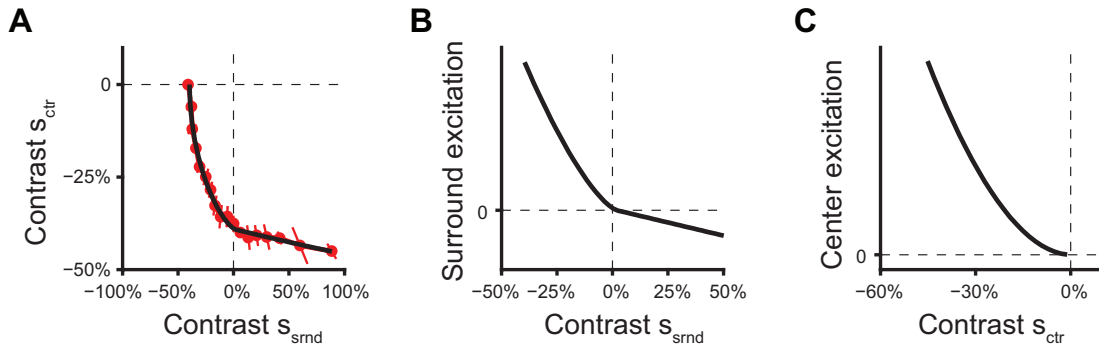


Figure 5.4: Maximum likelihood estimation (MLE) of the center-surround nonlinearities. (A) The measured iso-latency curve (red) is overlaid with a curve (black) calculated according to equation $N_{ctr}(s_{ctr}) + N_{srnd}(s_{srnd}) = const.$ (B) The surround nonlinearity $N_{srnd}(s_{srnd})$, as obtained by an MLE fit, is an incompletely rectifying power-law transformation (exponent = 1.5). (C) The center nonlinearity $N_{ctr}(s_{ctr})$ also corresponds to a power-law transformation (exponent = 1.9).

First, we focus on the regions I to III. The responses to stimuli in region # differed from the other responses and will be treated separately afterwards.

Because iso-rate curves were not simply straight lines, they also clearly revealed a nonlinear integration of center and surround signals. Individual iso-rate curves were much more diverse than iso-latency curves (Fig. 5.3). However, we did not find evidence that distinct curve types belonged to distinct ganglion cell types (see below). Hence, to interpret the main effect of the involved nonlinear processing, let us first look at the *average* iso-rate curve of the assessed cell population. Later we look at individual curves to discuss the deviations from the average behavior.

On average, the curves had a steep positive slope for dark contrast levels in the surround (Fig. 5.5): the darker the surround was stimulated, the darker the center had to be stimulated to yield the aspired number of spikes. This indicates that dark contrasts in the surround were non-preferred and had to be counterbalanced by preferred dark stimulation of the center. That the average curve (Fig. 5.5) was approximately linear for dark contrast levels (normalized contrast $s_{srnd} \lesssim -0.5$) argues for identical nonlinear transformations in both center and surround. In particular, if we assume that the nonlinearities $N_{ctr}(s_{ctr})$ and $N_{srnd}(s_{srnd})$ are well approximated by power-law transformations, it follows that the exponents of these power-laws have to be equal. This holds true because only in this case the equation $N_{ctr}(s_{ctr}) - N_{srnd}(s_{srnd}) = const$ yields a linear behavior for $s_{srnd} \ll 0$ (Appendix I). The information about the specific numeric value of the exponent of this power-law, however, is only encoded in the curvature of the curve in the region of small surround contrasts. Because the effects of the surround are

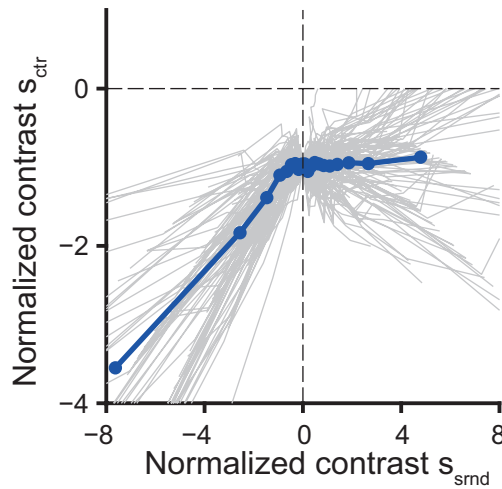


Figure 5.5: Behavior of the *average* iso-rate curve. The average curve was determined as average over all measured curves from all measured cells. Data points of curve region # were excluded. All curves were scaled such that the stimulus ($s_{ctr} = 1, s_{srnd} = 0$) lay on the curve (see Appendix J.9 for details). That the curve is rather linear for dark surround contrasts indicates that excitatory signals in the center and inhibitory signals in the surround are transformed by similar nonlinearities and subsequently integrated.

typically weak in this region, the exponent is difficult to recover from these experiments.

For bright surround contrasts, the slope of the average curve was close to zero, indicating that bright contrasts in the surround were cut off and did not contribute. Hence, the average behavior corresponded to a purely suppressive surround mechanism as suggested by H. B. Barlow (1953).

Now let us discuss individual curves instead of the average. In order to quantify their behavior, we compared the slopes of the curve regions I to III as obtained from a piecewise linear fit¹ among each other (Fig. 5.6, see Methods in Appendix J.9 for details). To this end, we fixed the boundaries of the different regions: region I, $s_{srnd} \leq -10\%$; region II, $-10\% < s_{srnd} \leq 10\%$; region III, $s_{srnd} > 10\%$, and ignored region #. In the following, we use the fit slopes to discuss the effects of surround stimulation in the different regions.

The steep positive slope for dark surround contrast levels that was dominating the average iso-rate curve could indeed be observed in every individual iso-rate curve (Fig. 5.6 B). If the target-response for the measured iso-rate curve was raised (Fig. 5.3 D), the slope became substantially increased. If one compares this result to the theoretical expectations of the scaling behavior

¹Please note that we use this fitting model just as a tool to describe the relative strength of the individual contributions and do not claim that indeed in each region a linear integration of center and surround signals occurs.

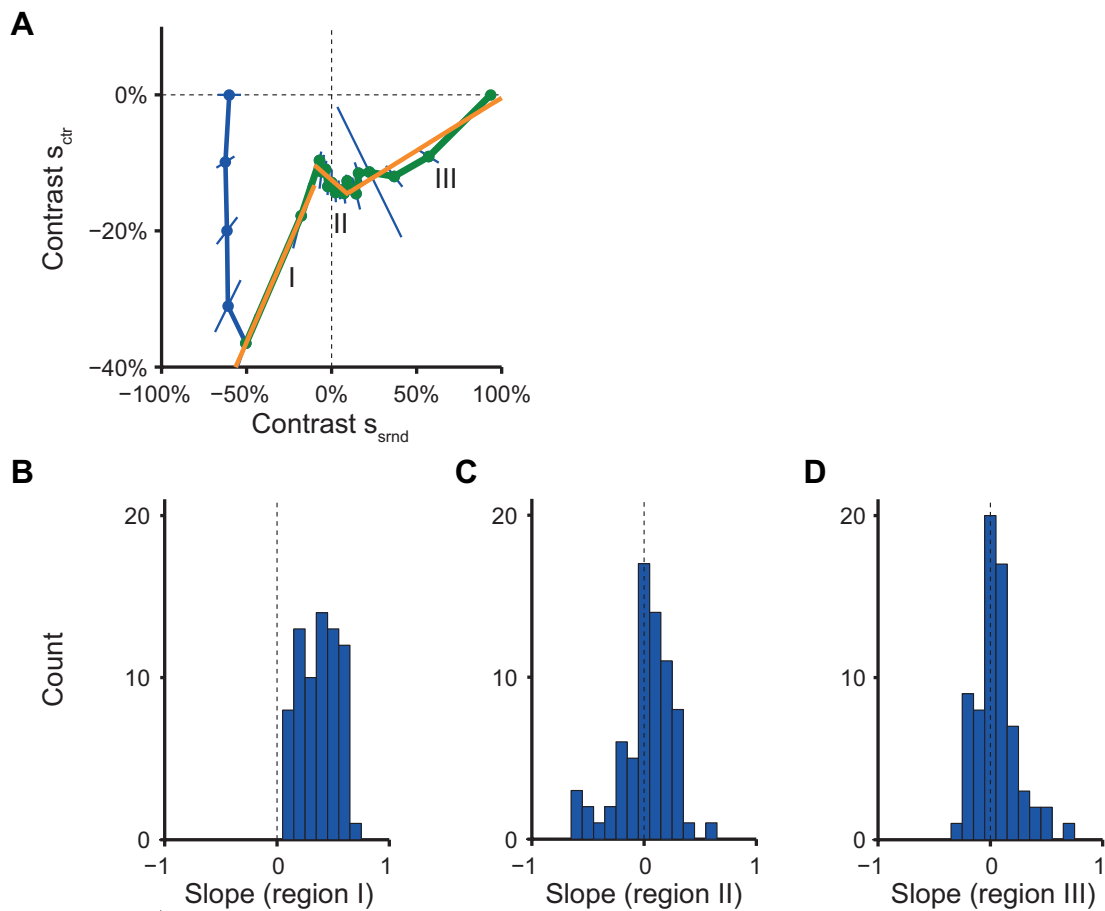


Figure 5.6: Analysis of individual iso-rate curves. (A) Example of a piecewise linear fit to iso-rate curves. Data points constituting a dark contrast upsurge were not taken into account. (B-D) Histograms of slopes of iso-rate curves in different regions.

(Fig. H.1), this might hint at a divisive effect of the surround.

In region III, comprising stimuli with strong bright surround contrast levels, the average curve ran parallel to the x axis, indicating a rectification of bright surround contrasts. Individual curves, however, deviated strongly from the average behavior (Fig. 5.6 D). Only in about one fourth of the cells a slope close to zero ($-0.05 < \text{slope} < 0.05$) could be observed. A more positive slope, as displayed by about half the cells, indicated that bright surround contrasts facilitate the center response: the brighter the surround was stimulated, the less dark contrast was needed in the center to yield the pre-specified response. Thus, bright stimuli in the surround acted either disinhibitory or excitatory. This effect corresponds to the behavior expected by a responsive surround in the sense of S. W. Kuffler (1953). About one fourth of the cells, however, displayed a negative slope in region III. This indicated that a bright surround stimulation suppressed the spiking response in a similar way as dark surround stimulation did. In this case, bright stimuli are either inhibitory or disexcitatory. Notably, the slopes of iso-rate and iso-latency curves in region III did not always correspond to each other (e.g. Fig. 5.3 A). This might result from slower dynamics of the ON compared to the OFF pathway (Nelson 1973, Frumkes and Miller 1979, Burkhardt et al. 2007), or from a time delay induced by an inhibitory interneuron.

Similar effects as in region III could be observed in region II, defined by weak stimulation of the surround with either bright or dark contrasts. Also in this region half the cells displayed a positive slope, while one fourth of cells either had a negative slope or a slope around zero ($-0.05 < \text{slope} < 0.05$). In the latter case, a flat plateau arose, suggesting a threshold mechanism in the surround of these cells (e.g. Fig. 5.3 A). If the contrast level was below this threshold, it did not influence the center response.

In summary, the diverse behaviors of iso-rate curves for weak and bright surround contrast levels suggest that multiple pathways mediated the signals evoked by these stimuli: in some cells, weak and bright surround contrasts generated excitatory or disinhibitory signals. The opposite was true in other cells, where inhibitory or disexcitatory signals were generated. In many cells, however, weak or bright contrasts were cut off and did not contribute at all. When we quantified these effects by calculating the slope of the iso-rate curve in the specific region (Fig. 5.6 C and D), we did not observe separable clusters in any of the histograms. Furthermore, we did not find any other cell properties (e.g. receptive field size or properties of the temporal STA) which were correlated with the slopes in region II and III. Hence, there is no indication that different curve types can be assigned to distinct cell types.

In most but not all iso-rate curves, a fourth region # could be observed for very dark contrasts in the surround (Fig. 5.3 A). There, the trend of the curve was suddenly reversed and the center

contrasts necessary to fulfill the iso-response condition started to decrease rapidly, resulting in an upsurge of the iso-rate curve. This upsurge extended until the end of the measured interval, where dark surround stimulation alone was sufficient to drive the cell strong enough to trigger the aspired number of spikes. If one measured iso-rate curves from a single cell for increasing target-responses (Fig. 5.3 D), the upsurge was observed to disappear.

5.2 SPIKE PATTERNS ALONG ISO-RATE CURVES

In order to shed more light on the iso-rate upsurge occurring at very dark surround contrasts (region #) and the dynamics of center-surround antagonism, we measured iso-response curves and then chose three characteristic stimuli on the curves for repeated measurements (see Methods in Appendix J.10 for details). This again allowed us to obtain PSTHs and visualize the temporal response profile (Fig. 5.7 A). Let us first compare the response for center only stimulation (Fig. 5.7 A, orange) with the response for homogeneous dark stimulation of center and surround (Fig. 5.7 A, black). We found that the latter had a shorter latency, was narrower and more peaked. This agrees with the notion that surround-generated inhibition truncated later responses. The reduction of later spikes then had to be compensated by earlier spikes in order to fulfill the iso-response condition. These earlier spikes were elicited by a stronger center stimulation (Sestokas et al. 1987). We expected that this reduction of latency would continue for increasing dark surround stimulation. Surprisingly, for the stimulus consisting of dark stimulation of the surround only (Fig. 5.7 A, green), the trend was broken and fewer fast spikes were generated. Instead, a second very late response peak was observed.

This occurrence of a second response peak for strong dark surround-only stimulation was further investigated. To this end, we repeatedly measured stimuli with fixed dark surround contrast and eight equally spaced dark center contrasts (Fig. 5.7 B, 4 of 8 stimuli are shown). For surround-only stimulation, both the fast and slow response peaks were clearly visible. When increasing the center contrast, the amplitude of the first peak increased and the amplitude of the second peak decreased until disappearance.

Thus, the late spikes were preferentially elicited if there was a stronger stimulation in the surround than in the center. Below, we hypothesize two alternative mechanisms which both can explain the occurrence of the delayed spike burst.

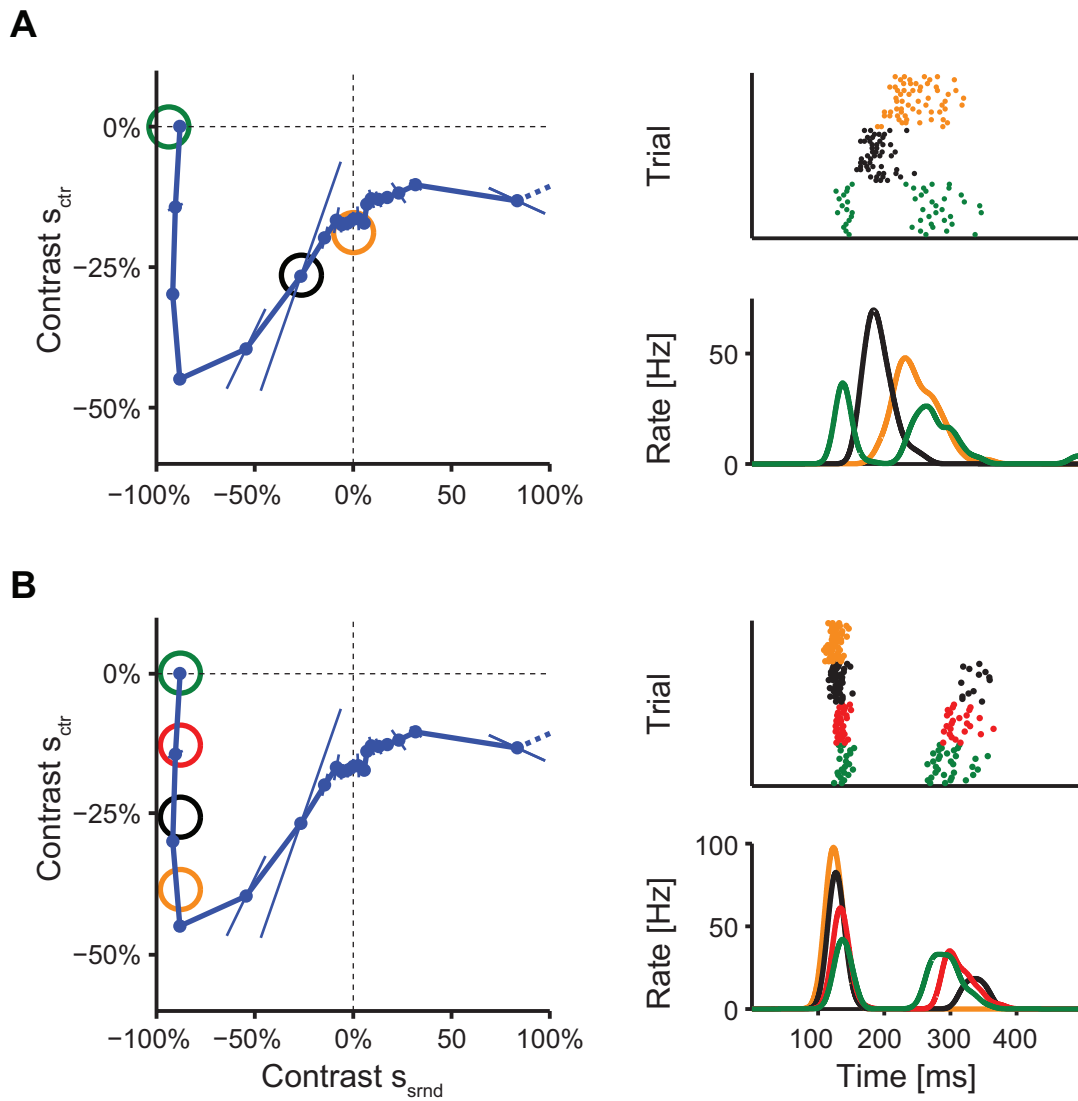


Figure 5.7: Temporal response profiles. (A) PSTHs for three different stimuli with center only stimulation (orange), homogeneous center-surround stimulation (black) and surround only stimulation (green). (B) PSTHs for stimuli with fixed surround contrast and an increasing center contrast.

5.3 COMPUTATIONAL MODELS OF CENTER-SURROUND INTEGRATION

The first hypothesis relies on the assumption that the surround is mainly inhibitory, and only little excitatory, while it is the other way round for the receptive field center. Thus, reducing the center stimulation² while keeping the surround stimulation fixed (Fig. 5.7 **B**) leads to a strong decrease of excitatory signals. Inhibitory signals, on the other hand, are less attenuated. Hence, the result is a vast exuberance of surround inhibition and only little or no center excitation. Because the late spike burst occurred preferentially under this condition, it suggests that it is the inhibition itself that generated this burst by a rebound excitation mechanism: strong postsynaptic inhibitory input causes a strong hyperpolarization of the ganglion cell. When the inhibition stops, the ganglion cell membrane potential overshoots the resting potential and thus creates a transient depolarization; causing spikes. Such a mechanism indeed has been found in retinal ganglion cells (Mitra and Miller 2007a,b).

Taking such a spike generation mechanism into account, a simple circuit model could reproduce the measured iso-rate upsurge (Fig. 5.8 **A**). In the model (see Methods in section J.11 for details), the antagonistic surround is mediated by an amacrine cell, which in turn is excited by rectifying-quadratic OFF bipolar cells in both center and surround. The amacrine cell itself is linear; hence this setup features a rectifying-quadratic dependence of the inhibition on the input contrasts. Additionally, the bipolar cells forward direct excitation to the ganglion cell. The synaptic weights are adjusted with respect to the assumption that the surround contributes most to the inhibition: the synapse between the surround bipolar cell and the amacrine cell has a bigger synaptic weight than the synapse between the center bipolar cell and the amacrine cell. Furthermore, the weight of the bipolar cell to ganglion cell synapse is weaker in the surround than in the center. Spikes are generated either if the ganglion cell membrane potential, calculated as difference of incoming excitation and inhibition, crosses a small positive threshold (regular spikes) or falls below a big negative threshold (rebound spikes). With this simple setup, the model can qualitatively reproduce iso-response curves as well as the observed temporal response profile (5.8 **A** middle and bottom).

The second hypothesis relies on the assumption that the late spikes are triggered by excitation that still prevails after inhibition has declined. We constructed a model that fulfills three conditions along an iso-rate curve: A) Upon stimulation of the center only, the inhibition is too slow and too weak to significantly reduce the ganglion cell's response. B) When stimulating the center and the surround, the inhibition is strong enough that all spikes are effectively abolished

²When we are talking about dark stimuli, *reducing* the stimulation actually means reducing the absolute value of the contrast $|s|$.

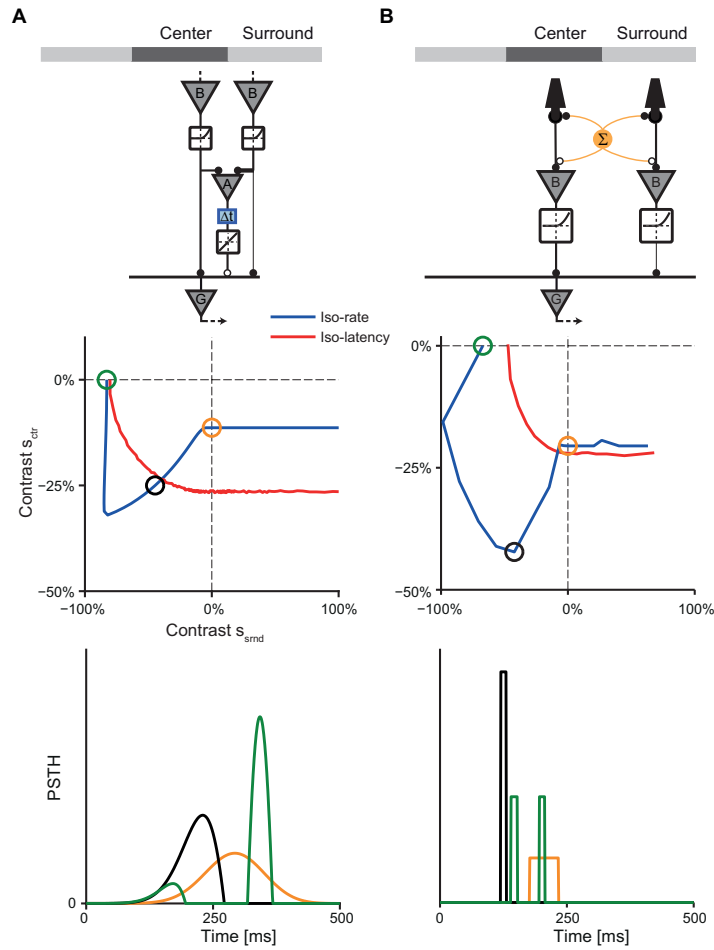


Figure 5.8: Computational models to explain the double-peaked temporal response profile. **(A)** A retinal circuit model simulating a rebound spike mechanism to reproduce the iso-rate upsurge (see Methods in Appendix J.11 for details). **(B)** A retinal circuit model simulating horizontal cell mediated inhibition. In this model, late spikes occur not as rebound spikes. They are generated by excitation that still prevails after the inhibition has declined (see Methods in Appendix J.12 for details). Top: Model circuits. Middle: Iso-response curves. Bottom: PSTHs for three distinguished stimuli.

after inhibition onset. C) When the center stimulation is decreased while the surround stimulus remains unchanged, the duration of the inhibition drops faster than the duration of excitation. Finally, upon surround stimulation only, the inhibition is shorter than excitation. Thus, spikes are triggered before inhibition onset and after inhibition offset.

We chose an implementation of this model relying on the outer plexiform layer as origin of the inhibition. On this level, horizontal cells create inhibitory feedback to photoreceptor terminals and most likely to bipolar cells (Duebel et al. 2006). The difference to inhibition in the inner plexiform layer (IPL) is the fact that horizontal cells are excited directly by cones; thus *before* the signal is transformed by the bipolar cell output nonlinearities. Therefore, signal integration by horizontal cells can be much more linear than one would expect in the IPL. Hence, we modeled the horizontal cell as linearly pooling center and surround contrasts (Fig. 5.8 **B**) and forwarding linear inhibitory output to the bipolar cell dendrites in center and surround. The effect of the horizontal cell is a function of $-(s_{ctr} + s_{srnd})$. In a second step of integration, the ganglion cell pools bipolar cell signals from both center and surround. Because the conditions A)-C) require a very detailed balance of excitation and inhibition, both signals were modeled as square pulses with variable latency and duration. This allows us to control signal duration and latency in more detail (see Methods in section J.12 for details).

Iso-response curves calculated in this model are indeed comparable to the measured curves (Fig. 5.8 **B** middle). Center stimulation only or homogeneous center-surround stimulation lead to a single spike burst, the latter with a reduced latency (Fig. 5.8 **B** bottom, orange and black PSTH). In contrast, stimulation of the surround only leads to two bursts of spikes, one before inhibition onset and one after inhibition offset (Fig. 5.8 **B** bottom, green PSTH).

Hence, with a horizontal cell mediated mechanism, it is possible to qualitatively explain the observed data. However, this model requires substantial fine-tuning of the model parameters and hence does not arise naturally from the circuit. Furthermore, it demands that excitation drops faster than inhibition for fixed surround contrasts and decreasing center contrasts. This seems to be quite artificial, because usually the excitatory component of the center is assumed to be stronger than its inhibitory component. Nevertheless, we chose to discuss the model to illustrate that we cannot absolutely exclude the horizontal cells as origin of the observed effects.

5.4 SURROUND ANTAGONISM IS MEDIATED BY INHIBITORY NEUROTRANSMITTERS

Iso-latency curves (Fig. 5.3 A-C, red curves) revealed an excitatory effect of dark surround stimulation, while iso-rate curves displayed a strong antagonistic effect. While excitation is directly forwarded to the ganglion cell, inhibition is generated in amacrine or horizontal cells and therefore acts slightly time delayed (Enroth-Cugell and Lennie 1975). During the course of the response, surround inhibition overcompensates surround excitation and leads to a net antagonistic effect. Due to the time delay, iso-latency curves are independent of inhibition and are only affected by the excitatory effect of the surround.

To test this, we added strychnine, bicuculline and picrotoxin to the bath in order to block glycinergic and GABAergic signal transmission and re-measured iso-rate curves (Fig. 5.9). While the control curves (Fig. 5.9, blue curves) clearly displayed an antagonistic effect of the surround, this effect disappeared when we blocked inhibitory neurotransmitters (Fig. 5.9, orange curves); the curves became similar to iso-latency curves, as expected from our hypothesis.

5.5 CENTER-SURROUND STRUCTURE OF HOMOGENEITY DETECTORS

In chapter 4, we reported that homogeneity detectors are usually cells that do not show an antagonistic surround when stimulated with blinking dots of increasing size (Fig. 4.5). In contrast, in this chapter we demonstrated that all measured cells displayed suppressive responses upon dark stimulation of the surround. Among the assessed cells were also homogeneity detectors, as we verified by measuring iso-response curves of the kind introduced in chapter 4 (e.g. the cell of Fig. 5.3 C). Apparently the two tests for center-surround antagonism, blinking spots or iso-response curves, yielded different results. The reason is likely to be the very different stimuli used in both cases. When we used blinking spots, both center and surround saw the same contrast changes. When we measured iso-response curves, the contrast shown in the surround was usually bigger than the contrast shown in the center (e.g., compare the scaling of x- and y- axis in Fig. 5.3), rendering this method more sensitive to capture effects of surround antagonism.

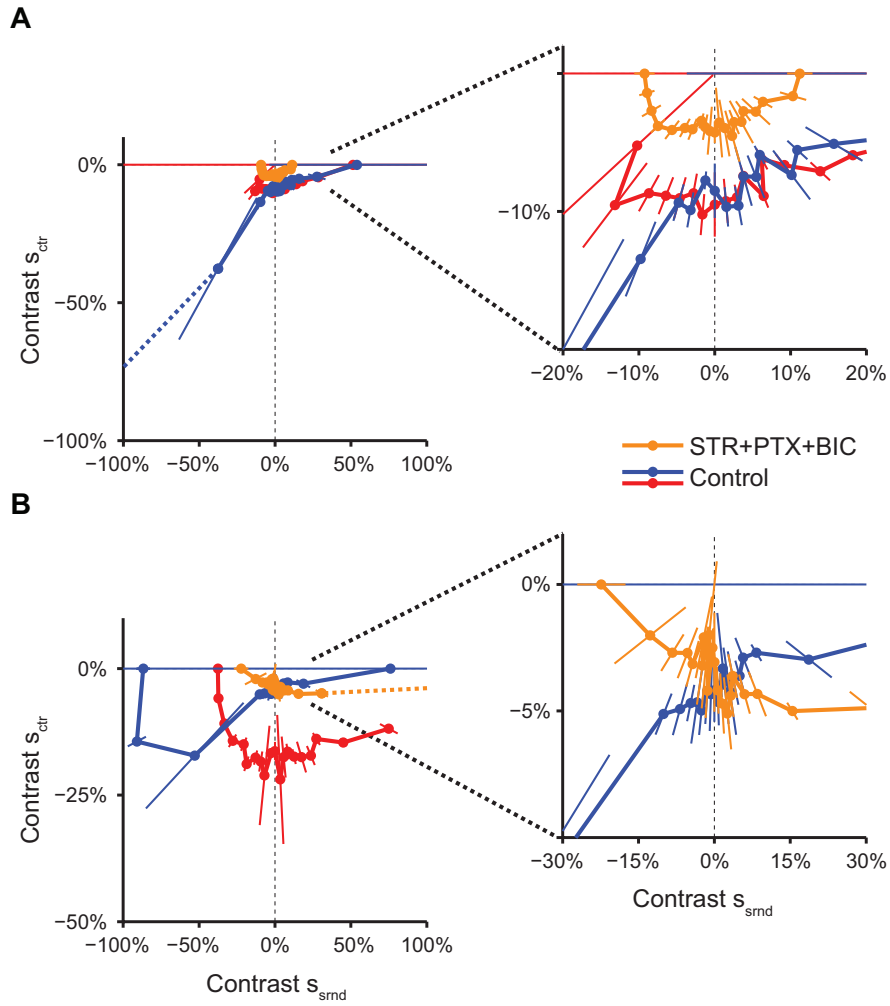


Figure 5.9: Inhibition-block experiments. **(A)** Iso-rate curves with inhibition blockers (orange, 4 spikes) and iso-rate (blue, 4 spikes) and iso-latency curves (red, 160 ms) under control conditions. **(B)** Second example. Orange: 6 spikes. Blue: 4 spikes. Red: 160 ms.

6. SUMMARY & DISCUSSION

Neurons in the nervous system typically receive multiple inputs which they integrate and consequently use to calculate their output. The role of the neuron is thus determined by the way this signal integration is performed. In particular, nonlinear processing steps are necessary to allow the neuron to execute *computations*. Thereby, important stimulus features can be amplified, while uninteresting components may be suppressed. In this thesis, we studied such nonlinear neuronal signal integration in retinal ganglion cells by measuring iso-response stimuli.

First we addressed the question of spatial integration within the ganglion cell receptive field center (chapter 4). For amphibian OFF ganglion cells, we generally found an approximately threshold-quadratic nonlinearity that was imposed locally on otherwise linearly integrated signals (Fig. 4.2). The nonlinear transformation seemed to occur on the level of bipolar cell terminals (Fig. 4.7 and Fig. 4.8). Due to this rectifying-quadratic signal integration, most assessed cells appeared to be particularly sensitive to small high-contrast stimuli within the receptive field center (Fig. 4.15 **D**). Surprisingly, a subset of cells generated spikes preferentially in response to low contrasts stimulating the whole receptive field center homogeneously (Fig. 4.15 **E**). We discovered that the spike-count response of these so-called homogeneity detectors was determined by a dynamic gain control mechanism which down-regulated strong subunit signals during the course of the response. The first-spike latency, however, was not affected by this mechanism (Fig. 4.2 **D**). We found that this gain control relied on inhibition and was thus most likely mediated by narrow-field amacrine cells (Fig. 4.11). A scenario based on synaptic depression (Fig. 4.10) or crossover inhibition (Fig. 4.13) was inconsistent with the data. Our experiments allowed us to suggest a circuit model that could explain all the obtained results (Fig. 4.14). Because homogeneity detectors typically had large receptive fields and only little or no antagonistic surround, these cells might indeed correspond to a certain morphological cell type. That there are two different types of nonlinear spatial integration in retinal ganglion cells has to our knowledge never been reported before. This is because other methods like the X-/Y-cell analysis or spike-triggered covariance analysis cannot reliably discriminate between the two nonlinearities.

Subsequently, we studied center-surround integration in salamander OFF ganglion cells by

using iso-response curves. The determined curves (Fig. 5.3) strongly deviated from straight lines. This indicates that center and surround signals were nonlinearly transformed before they were combined. Iso-latency curves revealed that the first-spike latency was not subject to a *suppressive* surround. Instead, the surround contributed to the cell's response in the same way as the center did. In particular, the surround elicited excitatory signals which also seemed to be transformed by a roughly rectifying-quadratic nonlinearity. Iso-rate curves, on the other hand, were dominated by a strong surround-triggered inhibition, elicited by dark surround stimuli. The data seem to be most congruent to a model that derives its inhibitory surround signals by the same nonlinearity as used by the center to derive its excitatory signals (Fig. 5.5). In response to bright stimuli in the surround either excitatory, inhibitory, or no signals were elicited in different cells, respectively. If there were such signals, they affected the response typically weaker than the inhibitory signals triggered by dark surround contrasts. Moreover, in most cells, the antagonistic effect of the surround on the number of elicited spikes was suddenly reversed when the surround contrast levels fell below a negative threshold: stimuli expected to be mostly suppressive triggered an unexpectedly large number of action potentials. By measuring the temporal response profile for those stimuli (Fig. 5.7), the occurrence of a second delayed spike burst could be identified as origin of this effect. These late spikes might be generated by rebound excitation which was triggered by a hyperpolarization of the ganglion cell in response to strong surround stimulation. It could be shown in a simulation (Fig. 5.8 A) that such a mechanism in combination with an integration of center and surround signals in the inner plexiform layer can indeed well reproduce all measured data. Nevertheless, we cannot completely rule out that the outer plexiform layer plays a role. By blocking GABAergic and glycinergic synaptic transmission, the antagonistic effects of the surround could be abolished (Fig. 5.9). Iso-rate curves took a similar shape as iso-latency curves, also revealing the presence of an excitatory contribution of the surround.

6.1 BENEFITS OF ISO-RESPONSE MEASUREMENTS

Throughout this thesis, we relied on the measurement of iso-response stimuli to determine the nonlinearities involved in spatial integration in the retina. This method had previously proven to be particularly suited to determine nonlinearities in neuronal processing (Gollisch et al. 2002, Gollisch and Herz 2005). Also for our investigation, iso-response stimuli offered several advantages compared to other approaches.

First, the method is fast. Multi-electrode arrays typically provide stable extracellular recordings over several hours. By comparison, a closed-loop measurement of a single iso-response curve typically takes only about 15 minutes. The online processing of the obtained data allows us

to evaluate the determined curve immediately after it has been recorded. Hence, on the basis of the previous results, we can decide which measurements to execute next. In particular, it enables us to initiate follow-up experiments like measurements of temporal response profiles (Fig. 4.9 and Fig. 5.7), iso-response curves with different checkerboard (Fig. 4.7) or pre-depressing stimuli (Fig. 4.10), or inhibition block experiments (Fig. 4.11, Fig. 4.13 and Fig. 5.9). Therefore we can make optimal use of the available measurement time.

Second, the nonlinearities of spatial integration can be determined by the measurement of iso-response stimuli independent of the intrinsic nonlinear processing of the ganglion cell (equation (3.3)). This cell-intrinsic nonlinearity describes the spike generation mechanism and transforms the cell's output *after* the inputs have been integrated. Therefore, it is not possible to discriminate linear from nonlinear integrating cells by simply comparing the sum of the responses triggered by individual stimuli to the response triggered by the sum of those stimuli (Fig. 3.8). The shape of iso-response curves, on the other hand, is independent of any nonlinear transformation of the output. Hence it allows us to directly read out the underlying nonlinearities of spatial integration without further assumptions. For example, curves that run parallel to one contrast axis indicate a rectification of the contrast represented by this axis. Circular curves represent a quadratic integration of preferred stimuli (Fig. 4.2), while linear lines correspond to a linear integration. Furthermore, for the investigation of center-surround integration, the shape of the iso-response curves does not depend on whether the surround has a divisive or subtractive effect on the signals generated in the center. Only the involved nonlinearities are reflected by the determined curves (Appendix H).

Third, by automatically searching for iso-response stimuli in a closed-loop fashion, we restrict the stimulation to contrasts that were in the right range to generate the aspired output signal. Thereby, we avoid stimuli that are much too strong. This does not only save measurement time, but also helps keeping the cell close to a constant adaptation level.

Fourth, by determining the stimuli which lead to the same response of a ganglion cell, we also learn which stimuli are classified as equal by upstream visual areas. In general, a mapping from a high-dimensional input onto a lower dimensional output does not only induce unwelcome ambiguities, but also helps to establish necessary invariances. In object recognition, for example, it is desirable that images of the same object are mapped onto a defined neuronal response, independent of the specific viewing angle. Such an invariance might arise from an appropriate integration over inputs from non-invariant cells (Riesenhuber and Poggio 2000). Hence, determining those stimuli that are classified as equal by the neuronal circuit seems to be a very natural way to learn about the important invariances of neurons, and thereby about their computational role in neuronal processing.

However, the closed-loop measurements of iso-response stimuli also had minor disadvantages. First, the spike-sorting had to be performed online. To this end, we used a simple threshold crossing algorithm. This is why we had to restrict our measurements to cells whose extracellular spiking responses had a big signal-to-noise ratio, and hence displayed large and easy-to-separate spikes. Most likely, such large spikes arise since the distance between the electrode and the recorded cell is small. Nevertheless, it is known that cells with big cell bodies generate bigger spikes in extracellular recordings than cells with small cell bodies (Olshausen and Field 2005, Towe and Harding 1970). Therefore, we possibly did not sample the ganglion cell population in an unbiased way, but preferred cells with large somata. The occurrence of homogeneity detectors in our measurements might thus not reflect the ratio of these cells in the retina. In future experiments, we expect that the spike detection can be significantly improved by the employment of real-time spike-sorting algorithms (Takahashi and Sakurai 2005, Franke et al. 2010). For the present study, we verified our results after the experiments by an additional in-depth analysis of the spike waveforms (Pouzat et al. 2002). The second disadvantage is that we could only assess one cell at a time, because the closed-loop algorithm calculates the next stimulus from the previous response of one specific cell. Therefore, we did not use the full potential of the multi-electrode array with which in principle sixty channels can be recorded simultaneously.

Throughout this thesis, we used step-like stimuli, meaning that the intensity values were simply switched on (Fig. 3.9). Instead, one might argue to use flickering contrasts. Iso-response curves could then be determined by spike-triggered systems analysis instead of a closed-loop experiment. This would allow us to assess multiple cells at the same time, but otherwise would have several disadvantages. First, as discussed in chapter 3.2, the sampling density will be distributed according to a pre-specified stimulus distribution and thus not provide sufficient data points along a single iso-response curve. Second, due to the temporal structure of the stimulus it is possible that further temporal nonlinearities come into play and disturb the assessment of spatial nonlinearities. Third, white noise stimuli drive retinal ganglion cells typically much weaker than step-like stimuli. Thus, subunit nonlinearities are sampled only in the range of low excitation.

Furthermore, it can be argued that a step stimulus that is switched on from a gray background is less artificial than one might think. The eye is performing eye movements all the time, either saccades or microsaccades (Martinez-Conde et al. 2004). It was shown that ganglion cells are silenced by rapid global shifts in natural scenes (Burr et al. 1994, Roska and Werblin 2003), as induced by saccades. Therefore, the time during such a shift might correspond very well to the gray background stimulation in our measurements. The image that falls onto the retina after a saccade thus has a clear onset and corresponds to a switched-on stimulus as used in this

investigation.

6.2 NONLINEAR SPATIAL INTEGRATION IN THE RECEPTIVE FIELD CENTER

Our starting point for the investigation of spatial integration in the receptive field center were the many studies reporting a nonlinear signal integration mediated by subunits in the receptive field. These studies, however, could only determine the underlying nonlinearities either very indirectly (Enroth-Cugell and Robson 1966, Baccus et al. 2008, Hochstein and Shapley 1976, Victor 1988, Victor and Shapley 1979), or only on the level of individual circuit elements, such as bipolar cell synapses (Demb et al. 2001, Burkhardt and Fahey 1998, Molnar et al. 2009). In contrast, in this thesis we strived for a complete functional characterization of the underlying nonlinearities.

In our experiments, we found that the latency response of all assessed ganglion cells was determined by approximately threshold-quadratic nonlinearities which occurred locally in spatial subunits. We argued that this nonlinearity reflects the underlying transformation imposed on the excitatory signals in the retina. Our results are supported by previous reports of rectifying nonlinearities involved in spatial integration in ganglion cells (Demb et al. 2001, Geffen et al. 2007, Gollisch and Meister 2008, Münch et al. 2009, Ölveczky et al. 2003, Shapley and Victor 1979, Victor and Shapley 1979). Individual subunits appeared to correspond to bipolar cells (Fig. 4.7), and the nonlinear transformation was not mediated by inhibitory neurotransmitters (Fig. 4.11 and Fig. 4.13). Therefore we assume that the bipolar cells themselves perform the threshold-quadratic signal transformation, either by a nonlinearity in their voltage response (Burkhardt and Fahey 1998), or in the synaptic transmission at the bipolar cell terminals (Demb et al. 2001, Baccus et al. 2008, Molnar et al. 2009).

The rate responses of the homogeneity detectors, however, appeared to be determined not only by excitation, but also by inhibition (Fig. 4.11). If individual subunits were strongly stimulated, this inhibition was triggered and suppressed the further spiking response. Thereby, the cells became particularly sensitive to homogeneous stimuli. Presumably, the inhibitory signals were generated by narrow-field amacrine cells (Chen et al. 2010, Masland 2001) which could be activated by single bipolar cells independently. Different from that, most previously studied contrast gain control mechanisms were independent of amacrine cell signaling (Beaudoin et al. 2007, Rieke 2001, Baccus and Meister 2002, Demb 2008, Manookin and Demb 2006, Burrone and Lagnado 2000, Singer and Diamond 2006). That the latency response was not affected by this gain control is likely due to the fact that inhibitory signals require an additional synaptic

stage, and are therefore time delayed compared to the excitation from bipolar cells (Cafaro and Rieke 2010, Roska et al. 2006, Werblin and Dowling 1969). Our data suggest that strong subunit stimulation generated disproportionately stronger inhibitory signals. Hence, the dependence of the amacrine cell activation on the bipolar cell output was superlinear. An example for such a nonlinear activation of inhibition has recently been reported by Jarsky et al. (2011), where they performed paired recordings of AII amacrine cells and presynaptic rod bipolar cells. In our recordings, this nonlinear activation of inhibition is also reflected in the iso-rate curves that were measured for different target spike counts. The notch in iso-rate curves became more pronounced with stronger stimulation (Fig. 4.6 A), as is expected from a superlinear activation of the involved amacrine cells (Fig. 4.14).

One could speculate that this local gain control arises by intrinsic properties of retinal ganglion cells. Active conductances in the dendrites, e.g. potassium channels, also might lead to a local downregulation of strong inputs (Weick and Demb 2011). If the activation of these conductances is sufficiently delayed, iso-latency curves would not be affected. Thus, this mechanism would resemble the effects of the gain control presented here, but would not require an additional inhibitory pathway. Therefore, it might be considered to be physiologically *cheaper*. Which advantages does the implementation of the gain control via an inhibitory pathway offer? One possibility is that the implementation via an amacrine cell provides more flexibility: for example, additional mechanisms (e.g. dopamine level, adaptation level, far-surround stimulation) could regulate the properties of the involved inhibitory pathway, and maybe even possess the capability to switch the gain control on or off. A similar mechanism has already been demonstrated in the salamander retina (Geffen et al. 2007). In this study, far-surround stimulation was found to modulate an inhibitory amacrine cell. This inhibition could in turn control the relative contributions of the ON and OFF path to the ganglion cell input. Thereby, these ganglion cells could dynamically switch from OFF to ON cells, depending on the visual context.

Homogeneity detectors responded most strongly to large dark stimuli that covered the whole ganglion cell receptive field. It is conceivable that such a stimulus indicates a potential threat to the animal, for example a suddenly appearing predator. Therefore it might be beneficial for the amphibian retina to have a distinguished type of ganglion cell which explicitly encodes such stimuli. Indeed, a ganglion cell type with similar properties has previously been found in the frog retina (Ishikane et al. 1999, 2005). Ishikane et al. described so-called dimming detectors which could detect large looming objects and subsequently trigger the frog's escape behavior. In particular, they demonstrated that the escape behavior could be abolished by blocking inhibitory neurotransmitters. Furthermore, they reported that dimming detectors had no antagonistic surround when stimulated with blinking black dots of increasing size. Both properties were also found in homogeneity detectors. In contrast to homogeneity detectors, the

mechanism underlying dimming detectors relied on synchronized retinal oscillations, rather than contrast gain control. However, it is possible that both mechanisms are present in the same cell type and work together to generate reliable alert signals in a wide range of possible scenarios.

6.3 NONLINEAR CENTER-SURROUND INTEGRATION

The term *antagonistic surround* is somewhat misleading because it can refer to two different effects. First, it suggests that stimulating the surround with the preferred contrast of the center reduces the ganglion cell response (suppressive surround). Second, it implies that stimulating with an opposing contrast increases or facilitates the response (responsive surround). These two effects are expected to occur equally in a linear model. In the retina, however, both contributions might be mediated by different pathways, e.g. involving ON or OFF bipolar cells, respectively. This appears likely because of the multitude of rectifying nonlinearities in the retinal circuit which only allow the transmission of contrasts of a certain polarity. Thus it is by no means trivial that the linear model of the center-surround antagonism really holds.

Indeed, our data suggest substantial differences in the strength of the individual contributions. The suppressing effect of the surround, as determined by iso-rate curves, was stronger than the facilitating effect (Fig. 5.6 **B** and **D**, e.g. curves in Fig. 5.3). Functionally, surround-generated inhibition and center-generated excitation appeared to be transformed by a similar nonlinearity (Fig. 5.5). In chapter 4, we found that the majority of ganglion cells transform signals in the center with an approximately rectifying-quadratic nonlinearity (Fig. 4.2 **B-D**). If we assume that center and surround signals were integrated after this rectifying-quadratic transformation, i.e. in the inner plexiform layer (see below), it follows that the surround-generated inhibition in these cells was also derived by the square of the dark surround contrasts. For homogeneity detectors, on the other hand, we found previously that the center nonlinearity is determined by a dynamic contrast gain control mechanism (chapter 4). However, center-surround iso-rate curves of homogeneity detectors were not distinguishable from curves of other cells (e.g. Fig. 5.3 **C**), thus also revealing an identical nonlinear transformation in center and surround. This implies that either the same dynamic effects were present in the whole receptive field, or that the contrasts used in this experiment were too weak to trigger the contrast gain control.

The dominance of a suppressive surround fits to the circuit of surround antagonism as proposed by Zaghloul et al. (2007) (Fig. 1.4). They report that as many as three inhibitory pathways transmit the lateral signal from the surround to the center. Thus, one can argue that the circuit is specifically designed to provide a suppressive surround response. A responsive surround

which is mediated by these inhibitory pathways is only possible via disinhibition: bright surround contrasts could reduce the baseline response of a certain inhibitory cell and thus generate a net excitatory signal. Horizontal cells, which are known to respond very linearly over a wide contrast range (Tranchina et al. 1981, Sakuranaga and Naka 1985) might be suited candidates for this. Furthermore, a recent study suggests that linear OFF amacrine cells can have a strong disinhibitory effect (Manu and Baccus 2011). Another possible mechanism for a responsive surround is the involvement of ON path mediated excitation. Under this assumption, responses to bright surround contrasts result from excitatory ON bipolar cells in the receptive field surround. At first glance, this contradicts our finding that basically none of the amphibian ganglion cells displayed ON responses when stimulating only the receptive field center (compare chapter 4, Fig. 4.2 and 4.7). However, it was found in mice that the stimulation of the surround is a requirement for ON-OFF cells to respond to bright stimuli, supporting the notion that OFF center ganglion cells might be connected to ON bipolar cells primarily in their surround (Sagdullaev and McCall 2005)¹. This justifies the assumption of excitatory ON signals evoked by surround stimulation, although no evidence for it was found upon center-only stimulation. Moreover, our findings indicate that stimulating the surround with bright contrasts is in some cases not facilitating at all, but also suppressive (Fig. 5.6 **D**). This might result from an ON path triggered amacrine cell or from a disexcitatory effect of only weakly rectifying OFF bipolar cells.

A particularly interesting feature of the data is the occurrence of a double peaked temporal response profile. Such a response was elicited by strong dark surround contrasts (Fig. 5.7 **A** and **B**). The two response peaks correspond to an early and a late spike burst that constituted the prominent upsurge at the left end of most iso-rate curves. The early peak most likely arises, in agreement with the results from iso-latency curves, from excitatory OFF input from the surround. Subsequently, spiking is silenced by the time-delayed surround-generated inhibition. The origin of the late spike burst is not completely clear. Two hypotheses have been proposed. First, inhibition itself might generate the spikes via a rebound excitation mechanism (Fig. 5.8 **A**). This hypothesis fits best to the idea that the excitatory effect of the center is much stronger than its inhibitory effect. Spikes caused by rebound excitation have previously been shown to exist in the retina (Mitra and Miller 2007a,b). Second, late spikes might be generated by excitation that still persists after the inhibition has attenuated (Fig. 5.8 **B**). The latter, however, leads to a rather unintuitive explanation of the measured temporal response profiles. It requires that inhibition decreases stronger than excitation with decreasing center contrast. This is not the behavior expected of the receptive field center, which is thought to be mainly excitatory.

That the iso-rate upsurge is not present in all determined curves is probably not a question of cell type. For some measurements, the iso-rate upsurge might just be outside the experimen-

¹It is unclear, however, if this result also holds for amphibians.

tally accessible range. This notion is supported by the finding that the upsurge can appear or disappear depending on the number of spikes along a measured iso-rate curve (Fig. 5.3 **D**). Furthermore, the probability to measure the upsurge might depend on the size of the receptive field center. For big center sizes, the relative influence of the surround is smaller which makes it more difficult to generate enough (rebound) excitation for the upsurge to occur.

With our measurements, we could not with certainty disentangle inhibition in the outer plexiform layer from inhibition in the inner plexiform layer. However, our data gives hints on the type of the involved inhibitory pathways. In particular, two arguments favor the hypothesis that the observed inhibitory surround is more likely mediated by amacrine cells, and not by horizontal cells. First, blocking GABAergic and glycinergic signaling completely abolished the strong antagonistic effects of the surround. Horizontal cells most likely have a feedback mechanism which does not depend solely on these neurotransmitters (Wu 1994, 2010). Thus, one might assume that an antagonistic component remains upon GABA and glycine block if it was mediated by horizontal cells. Second, our computational modeling showed that a model relying on rebound excitation can explain the observed effects more robustly than a horizontal cell model. The generation of rebound spikes requires a strong hyperpolarization of ganglion cells, most likely produced by strong inhibition in the inner plexiform layer. Also a computational study of Saglam et al. (2009) concludes that the major part of the center-surround antagonism is amacrine-cell mediated. Several experimental studies support this hypothesis (Cook and McReynolds 1998, Zaghloul et al. 2007).

In contrast to iso-rate curves, iso-latency curves did not indicate the presence of an inhibitory surround (Fig. 5.3 **A-C**). Both dark surround and center stimulation seemed to elicit excitatory signals which were transformed by approximately rectifying-quadratic nonlinearities (Fig. 5.4), most likely mediated by rectifying-quadratic bipolar cells in center and surround (compare to chapter 4). Surround-triggered inhibition appears to be time delayed; therefore being too slow to affect the latency of the response. Indeed, also other groups reported that the response of the surround is time-delayed by tens of milliseconds to the center response. This was observed both in ganglion cells (Enroth-Cugell and Lennie 1975) and in bipolar cells (Werblin and Dowling 1969, Fahey and Burkhardt 2003). Furthermore, Gollisch and Meister (2008) suggested that the first-spike latency of specific cells is not subject to a surround suppression when encoding natural stimuli. The slow time course of inhibition might also be one reason why the step-like stimuli used in our experiments are better suited to probe the antagonistic surround than flickering stimuli, like those used to perform spike-triggered systems analysis (compare chapter 3.2). A common assumption is that this slow time course arises from low-pass properties of the additional synapses (Armstrong-Gold and Rieke 2003). If this is the case, inhibitory mechanisms integrate longer stimulus periods. Thus, randomly flickering inputs tend to average out and

impede strong surround responses.

Experiments using annuli of light as stimulus always suffer from uncertainties about how much stray light of the annulus falls onto the center region. In our measurements, we expect that stray light would push the slope of the iso-response curves towards smaller values. This occurs because bright stray light of the surround effectively reduces the dark stimulus in the center. We tried to minimize possible effects by carefully focusing the stimulus onto the photoreceptor layer of the retina, but cannot rule out completely that scattered light biased our experiments.

6.4 TEMPORAL INFORMATION IN RGC RESPONSES

Classically, the information encoded in the spiking response of a neuron is thought to be stored in the number of fired action potentials (Adrian and Zotterman 1926, Perkel and Bullock 1968, Bialek and Rieke 1992, Warland et al. 1997). However, over the last years evidence accumulated that also the temporal patterns of spikes contain information (Berry and Meister 1999, Nemenman et al. 2008, Gollisch and Meister 2008). In particular, it was shown in specific ganglion cells that the first-spike latency serves indeed better to discriminate between stimuli than the spike count (Gollisch and Meister 2008). Also during our experiments, we found indications that the latency, or even the structure of the temporal response profile, might play a role in the encoding of stimulus information.

First, the importance of latency coding is supported by the uniformity of all latency nonlinearities that were found in amphibian cells. In all cells, the latency response seemed to be determined solely by rectifying-quadratic subunits in both center and surround. No exceptions have been found. Any possible inhibition, which appears to make responses more diverse, seems to be too slow to significantly affect the latency. Therefore, the latency might provide a suited readout signal which can be treated equally from each cell, independent of its specific type. This readout could be used for rapid image formation in upstream visual areas (Olshausen and Field 2005, Gollisch and Meister 2008).

Second, we found that either homogeneous stimulation of the receptive field center and its surround, or stimulation of the surround only can lead to responses with an approximately identical number of spikes and a similar first-spike latency (Fig. 5.7 **B** orange and green). However, the two stimuli can still be discriminated by the temporal structure of the action potentials. In response to homogeneous stimulation, all the spikes follow the first spike within a single burst. In contrast, upon surround stimulation, two distinguished spike bursts are elicited, with silence in between. However, it remains unclear if the higher visual areas extract this available information.

OUTLOOK

In this thesis, we applied closed-loop measurements of iso-response stimuli for characterizing stimulus integration by retinal ganglion cells. The question we asked was:

How are spatially distinct visual stimuli within a receptive field of a ganglion cell combined and encoded in the cell's response?

Indeed, it turned out that the iso-response approach is an extremely useful tool to address this question, and several interesting results could be obtained. In particular, the experiments generated a deeper understanding of the computations performed in the retina.

In addition, the method has the potential to be applied on many more interesting questions. For example, the measurements performed in this thesis could be done intracellularly in a patch-clamp experiment. This would allow us to measure *iso-inhibition* or *iso-excitation* curves and thus to disentangle the network mechanisms on an even deeper level. Let us therefore assume that we measure such curves with the stimuli of chapter 4 which divide the receptive field center into halves. How are the results going to look like, assuming that the inhibitory signal in our proposed circuit model of homogeneity detectors is postsynaptic? In this case, one might expect that iso-excitation curves, along which the integral of excitation is constant, take rectifying-quadratic shapes for all cells. A deviation of this shape is expected in iso-inhibition curves of homogeneity detectors, in which the polar curve radius for homogeneous stimuli is expected to be strongly increased. In contrast, if the inhibition is presynaptic, the iso-excitation curves of homogeneity detectors will display the same shape as iso-rate curves in our measurements.

Also to elucidate the mechanisms of center-surround antagonism intracellular iso-response curves would be of great interest. To explain the iso-rate curves that we measured in chapter 5 (Fig. 5.3), we hypothesized two different models (Fig. 5.8). One of these models crucially depended on a rebound excitation mechanism. We assumed that strong hyperpolarization would trigger rebound spikes in ganglion cells. With intracellular measurements it should be possible to prove or disprove if strong stimulation of the receptive field surround can lead to a strong hyperpolarization of the cell. One approach could be to determine those stimuli which lead to

a predefined hyperpolarization.

Furthermore, it would be interesting to perform the same measurements of chapter 4 in cats, rabbits, or other mammals that are known to have linearly integrating cells. One suggestion is that this linear integration is achieved by correcting for nonlinearities in synaptic transmission via crossover inhibition (Molnar et al. 2009). If this holds true, one might expect to find rectification in iso-latency curves and linear iso-rate curves.

One might also try to explore the effect of the non-classical far surround (Geffen et al. 2007) or of the excitation of a neighboring cell on the spiking response. To this end, the closed-loop search algorithm could be used to find those far-surround stimulus patterns that maximize the influence on the cell's response.

Another experiment exploiting the closed-loop approach would be the search for *optimal stimuli* (Machens et al. 2005). Questions like "Which stimuli maximize the synchrony between two ganglion cells?" could be addressed by choosing an as general as possible stimulus that can be described in a preferably low-dimensional parameter space. The closed-loop approach would then be used to search for those stimulus parameters which maximize synchrony. Similar experiments asking the question "What does the eye see best" have already been performed in a similar, but less automated fashion (Watson et al. 1983).

Of course, the method is not restricted to investigations of the retina. Similar circuit structures as proposed to generate the local gain control of homogeneity detectors (Fig. 4.14) have also been identified elsewhere in the brain (Bellavance et al. 2010, Cruikshank et al. 2007, Gabernet et al. 2005, Porter et al. 2001, Pouille and Scanziani 2001, Strowbridge 2009, Sun et al. 2006) where they may serve similar functions by controlling local gain of signal integration. Assuming that different local subcircuits can be stimulated independently, it is likely that analogous investigations of input integration through iso-response measurements will help us better understand the function of this fundamental circuit design in these systems as well.

In a more general context, the usefulness of closed-loop experiments is not restricted to electrophysiology. Routinely, closed-loop feedback is used in virtual reality facilities, where the virtual scene is controlled by the movement of the subject. With such methods, it is possible to determine iso-response curves on a behavioral level (A. Bahl, personal communication).

Closed-loop approaches are also developed for fMRI applications where visual feedback is provided to patients to cure pain (de Charms et al. 2005) or tinnitus (Haller et al. 2010). Also fMRI iso-response measurements could be performed. It might be very interesting to approach questions of multisensory integration. "How do auditory stimuli influence our visual perception?" can be one of these questions. For example, in the so-called double-flash illusion, a certain number of flashes are displayed to the subject while simultaneously playing a certain

number of beep tones. It turns out that the number of perceived flashes is reduced if there were fewer beeps than flashes (Shams et al. 2000). fMRI studies show that already the V1 activity is changed by the auditory cues (Watkins et al. 2007). Iso-response experiments could shed more light on the type of integration performed in the visual cortex. If a set of iso-response (i.e. iso-BOLD) stimuli is obtained, one particular strength of fMRI comes into play: the test subjects are humans. Thus, the experiments can be connected with psychophysical studies, in which the equality of the BOLD response can be correlated with the equality of the subjective perception of the stimuli. Similar experiments could also be performed using purely visual stimuli, for example by studying the integration and iso-perception of stimuli with varying contrast and frequency.

CLOSURE

At the beginning of this thesis, we stated that we hope to elucidate the general mechanisms of signal integration in the brain by studying the particular spatial integration in the retina. Hence, let us summarize the generalized conclusions of this thesis. First, by investigating how signals are nonlinearly combined in retinal ganglion cells, we gave clues about how such an integration might be performed in other circuits of the brain. In particular, we showed that the same neuronal circuit can impose different nonlinearities on the response as determined by the rate, and on the response as determined by the latency. Thus, it is possible to perform two separate computations with only one circuit, and to encode the one result in the rate and the other in latency. Second, we demonstrated the usefulness of closed-loop measurements of iso-response stimuli for the assessment of the involved nonlinearities. It turned out that this method was very suited to pursue our investigation, and that it enabled us to elucidate neuronal processing from a new perspective. We are confident that the method can be successfully applied also in other parts of the brain where similar circuits are present. Therefore, we are looking forward to hearing of many more interesting studies which use closed-loop measurements of iso-response stimuli in the future.

APPENDICES

A HORIZONTAL CELL INHERITED SURROUND ANTAGONISM

In this chapter, a rough estimate of the contribution of horizontal cells to the center-surround structure of retinal ganglion cells is discussed in a linear model (Fig. A.1). The underlying assumption is that the horizontal cells induce a center-surround structure in bipolar cells. Because the receptive field of a ganglion cell consists of overlapping bipolar cell receptive fields, it can be approximated as a weighted sum of the latter. Thereby we neglect potential nonlinearities in the bipolar cell output. The weight describes the decrease in strength of synaptic connections for increasing distance from the ganglion cell (Kier et al. 1995). In the receptive field center, the effect of the bipolar cell surround averages out. In the periphery, a net antagonistic effect of the bipolar cell remains and is inherited by the ganglion cell. Thus, the horizontal cell induced receptive field surround is of the spatial scale of the surround of a single bipolar cell. Furthermore, it is weak because the small synaptic weight in the peripheral region.

In amphibians, however, the receptive field surround is assumed to be much larger than the inherited surround demonstrated here. This lets us assume that additional pathways contribute, e.g. amacrine cell mediated inhibition. Potentially, spatial nonlinearities might also boost the size of the inherited receptive field.

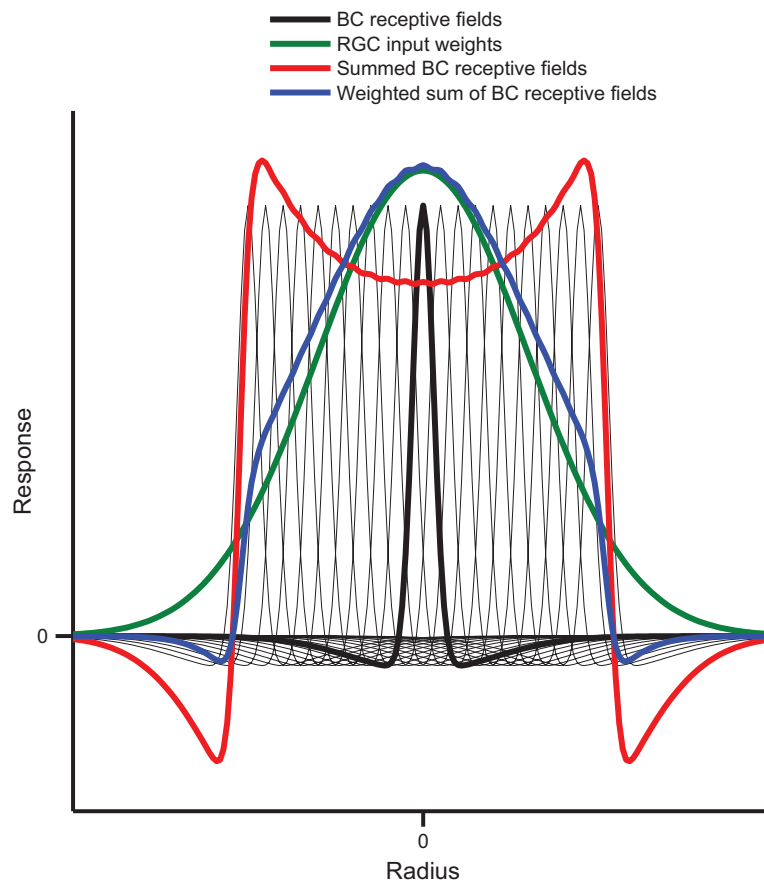


Figure A.1: Horizontal cells are likely to induce a center-surround structure within the bipolar cell receptive field (black). The summed effect of a set of overlapping bipolar cells is shown in red. If the synaptic weight is taken into account, which decreases with increasing distance from the center (green), the resulting ganglion cell receptive field takes a shape as shown in blue. It still displays a weak antagonistic surround effect inherited from the bipolar cells.

B EIGENVALUES OF THE STC MATRIX

Theorem: The variance of the stimulus ensemble in an arbitrary direction $\hat{\mathbf{y}}$ is given by the covariance matrix \hat{C} via

$$V_{\hat{\mathbf{y}}} = \hat{\mathbf{y}}^T \hat{C} \hat{\mathbf{y}}$$

if $\|\hat{\mathbf{y}}\| = 1$.

Proof: We simply expand the equation,

$$\begin{aligned} V_{\hat{\mathbf{y}}} &= \hat{\mathbf{y}}^T \hat{C} \hat{\mathbf{y}} = \frac{1}{N} \sum_i \hat{\mathbf{y}}^T (\mathbf{s}_k - \langle \mathbf{s} \rangle) (\mathbf{s}_k - \langle \mathbf{s} \rangle)^T \hat{\mathbf{y}} = \frac{1}{N} \sum_i \|(\mathbf{s}_k - \langle \mathbf{s} \rangle) \hat{\mathbf{y}}\|^2 \\ &= \frac{1}{N} \sum_i \|(\mathbf{s}_k \hat{\mathbf{y}} - \langle \mathbf{s} \hat{\mathbf{y}} \rangle)\|^2. \end{aligned}$$

The result is the variance of the projections of the stimuli on $\hat{\mathbf{y}}$, and thus is the variance in $\hat{\mathbf{y}}$ direction.

Theorem: The direction in stimulus space, in which the variance of a stimulus ensemble is maximal (minimal) is given by the eigenvector of the covariance matrix \hat{C} corresponding to the biggest (smallest) eigenvalue.

Proof: We proof this for the biggest eigenvalue λ_1 . To do so, we calculate the variance in an arbitrary direction $\hat{\mathbf{y}}$ expressed in the basis of the eigenvectors $\hat{\mathbf{e}}_i$,

$$\hat{\mathbf{y}} = \sum_i a_i \hat{\mathbf{e}}_i.$$

The variance in this direction is then determined by

$$V_{\hat{\mathbf{y}}} = \hat{\mathbf{y}}^T \hat{C} \hat{\mathbf{y}} = \hat{\mathbf{y}}^T \sum_i a_i \hat{C} \hat{\mathbf{e}}_i = \hat{\mathbf{y}}^T \sum_i a_i \lambda_i \hat{\mathbf{e}}_i \leq \lambda_1 \hat{\mathbf{y}}^T \hat{\mathbf{y}} = \lambda_1.$$

We used that $\|\hat{\mathbf{y}}\| = 1$, $\hat{C} \hat{\mathbf{e}}_i = \lambda_i \hat{\mathbf{e}}_i$ and that λ_1 is the biggest eigenvalue. For $\hat{\mathbf{y}} = \hat{\mathbf{e}}_1$ the equal sign in above equation holds. Therefore, the variance in $\hat{\mathbf{e}}_1$ -direction is maximal.

C STC ANALYSIS OF A MODEL NEURON

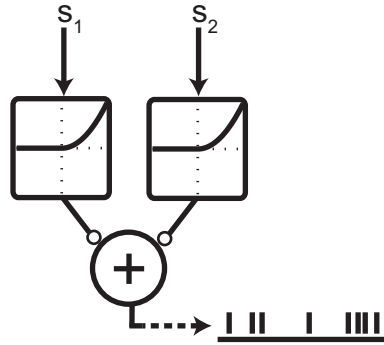


Figure C.1: Model neuron. The model consists of two spatial subunits which receive individual inputs and pass them through a rectifying quadratic nonlinearity. The outputs of both subunits is then summed in the ganglion cell. An instantaneous Poisson process decides how many spikes are elicited.

In this section, a neuron model is analyzed using STC analysis (Fig. C.1). The neuron consists of two subunits which receive individual inputs s_1 and s_2 , respectively. Each input value is drawn randomly from a Gaussian distribution with mean $\mu = 0$ and variance $V = 0.09$. The subunits pass their input through a rectifying-quadratic nonlinearity $N(\cdot) = |\cdot|_+^2$. The summed signal of both subunit outputs constitutes the instantaneous firing rate. The rate is converted into spikes by an instantaneous Poisson process. Thus, the cell can be described in a generalized LN model (Fig. 1.6 B) with two filters,

$$\mathbf{f}_1 = (1 \ 0)^T \quad \mathbf{f}_2 = (0 \ 1)^T$$

and subsequent nonlinearities $N(\cdot)$. When applying STC analysis to this model, two eigenvectors \mathbf{v}_i are recovered from the spike-triggered stimulus ensemble (Fig. C.2),

$$\begin{aligned} \mathbf{v}_1 &= (1 \ 1)^T & \lambda_1 &= 0.067 \\ \mathbf{v}_2 &= (-1 \ 1)^T & \lambda_2 &= 0.187. \end{aligned}$$

Both eigenvalues λ_i deviate significantly from the raw stimulus variance. \mathbf{v}_1 corresponds to the STA of the cell while \mathbf{v}_2 points in the orthogonal direction. The corresponding nonlinearities are exponential for \mathbf{v}_1 and u-shaped for \mathbf{v}_2 . Thus, the STC analysis does not recover the fundamental filters \mathbf{f}_i nor the nonlinearity $N(\cdot)$. In particular, the obtained filters \mathbf{v}_1 and \mathbf{v}_2 are linear combinations of the underlying filters.

Important to note, the results of the STC analysis are not wrong in any sense. The obtained filters and nonlinearities correspond to an equivalent representation of the model. Unfortunately,

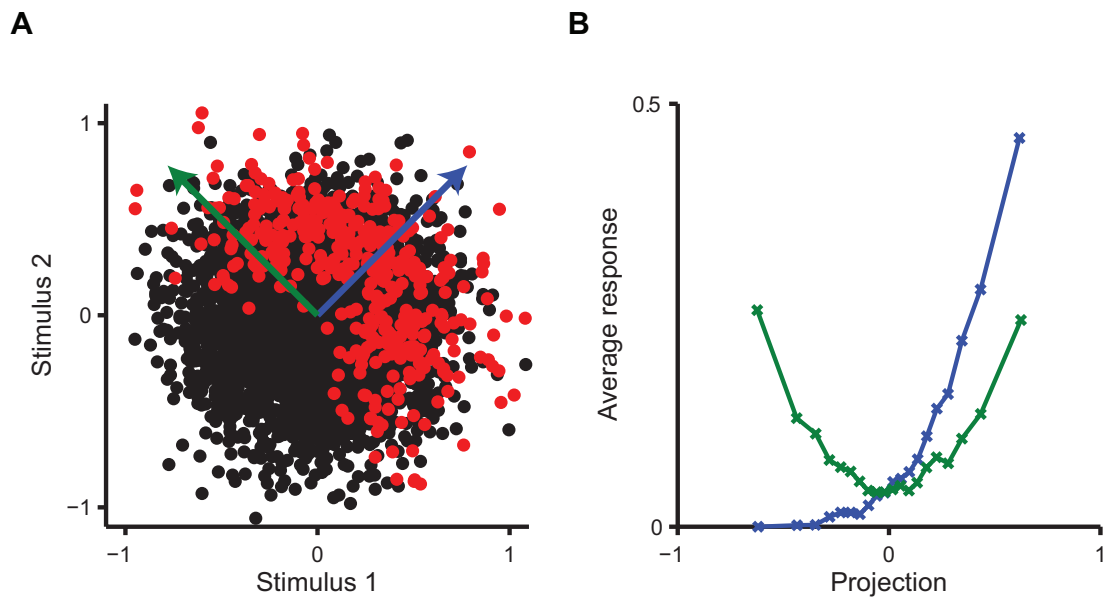


Figure C.2: STC analysis. (A) Raw- (black) and spike-triggered (red) stimulus ensemble. The eigenvectors of the spike-triggered covariance matrix are indicated as arrows. Green: Big eigenvalue. Blue: Small eigenvalue. (B) Nonlinearities of the eigenvectors. The colors correspond to the eigenvectors shown in A.

the spatial separation of subunits is lost in the STC description, because both filters include both subunits. Thus, STC analysis can be used to indicate spatial subunits, but is not a suited method for the determination of their individual spatial filters and nonlinearities.

D SCALE INVARIANCE OF ISO-RESPONSE CURVES

In this chapter, the concept of scale invariance is discussed in the context of iso-response curves. By definition, a function $f(\cdot)$ is called scale invariant if it fulfills the equation

$$f(\lambda x) = C(\lambda)f(x) \forall \lambda.$$

In particular, $C(\lambda)$ is a scaling function that only depends on λ , not on x . Power laws $f(x) = x^k$ are classical examples of scale invariant functions, as they fulfill

$$f(\lambda x) = (\lambda x)^k = \lambda^k x^k = C(\lambda)f(x), \quad C(\lambda) = \lambda^k.$$

In contrast, the exponential function $f(x) = e^x$ is not scale invariant, because

$$f(\lambda x) = e^{\lambda x} = (e^x)^{\lambda} e^x = C(\lambda, x)f(x),$$

i.e. the function $C(\cdot)$ is not independent of x .

As we will show in the following, a lack of scale invariance of the nonlinearities in the subunit model leads to different shapes of iso-response curves depending on the input strength, or equivalently, depending on the response elicited along the curve. To illustrate this, we assume a version of the subunit model (3.2) which we simplify by not considering a spike generation nonlinearity. Thus, the response r is given as

$$r(s_1, s_2) = N(s_1) + N(s_2).$$

In Fig. D.1 **A**, iso-response curves are determined for the not scale-invariant nonlinearity $N(x) = e^x$ for two different iso-responses $r = 2.8$ (green) and $r = 7.7$ (blue). To be able to better compare the shape of the curves, the radii of data points along the blue curve were scaled with a factor of one third. Thus, for the blue curve, the stimuli necessary to obtain the pre-specified response are about three times higher than in the green curve. As can be seen in the figure, the shape of both curves is not identical. The higher r , the more nonlinear the curve becomes. This is directly related to the lacking scale invariance of the nonlinearity. This becomes clearer in the Taylor expansion,

$$e^x = 1 + x + \frac{1}{2}x^2 + \dots$$

For small inputs x , the linear terms are dominant and the iso-response curve is rather linear. For big inputs, the higher order terms become stronger, thus the curvature is increased. In contrast, if one chooses a scale invariant function as subunit nonlinearity, as shown in Fig. D.1 **B** for $N(x) = \begin{cases} 0, & x < 0 \\ x^2, & x > 0 \end{cases}$, the shape of the curve is constant no matter on which scale the inputs are chosen.

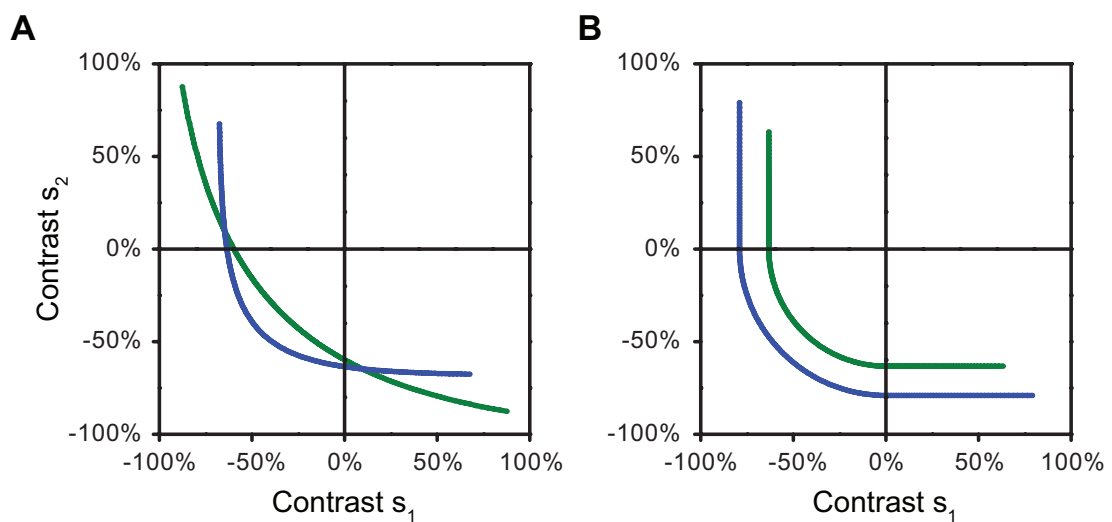


Figure D.1: Demonstration of scale invariance in iso-response curves. (A) Exponential nonlinearities are not scale invariant. Blue curve: Response $r = 7.7$ (scaled with a factor of $1/3$), green curve: $r = 2.8$. (B) Power law nonlinearities are scale invariant and therefore describe a certain shape of iso-response curves. Blue curve: $r = 10$ (scaled with a factor of $1/4$), green curve: $r = 0.4$.

E SIMULATION OF RESPONSE LINEARIZATION

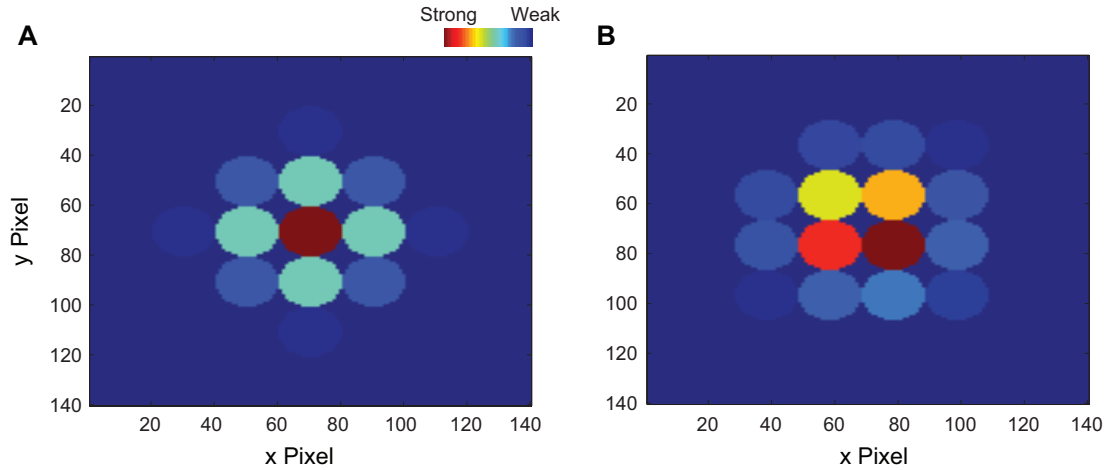


Figure E.1: Ganglion cell receptive field layout. The circular ganglion cell receptive field comprises circular subunits. The subunit midpoints are arranged on a square grid such that the subunit receptive fields touch each other at the rim. The weight of each subunit is determined by the distance of the subunit midpoint to the ganglion cell receptive field midpoint (blue: weak connection; red: strong connection). The alignment of the subunit grid with respect to the ganglion cell receptive field midpoint is random (A) Symmetric alignment such that a subunit midpoint is co-located with the receptive field midpoint of the ganglion cell (B) Shifted subunit layout.

In the model, the circular ganglion cell receptive field (600 μm diameter) is assembled by smaller circular subunits (Fig. E.1). The subunit midpoints are positioned on a rectangular grid such that they touch each neighbor at the rim. Each subunit sums the stimulus contrasts linear over its receptive field. We hereby assumed a flat filter, i.e. no Gaussian weighting within a subunit. On the subunit output the nonlinearity $N(g) = \begin{cases} m \cdot g, & g < 0 \\ m \cdot g + g^2, & g \geq 0 \end{cases}$ is imposed. g is the linear subunit activation, calculated as the average over all pixels within the subunit receptive field (Fig. E.2). Thus, the nonlinearity models a rectifying quadratic transmission with incomplete rectification. The factor $m = 0.3$ is set to reproduce the degree of rectification found experimentally when using stimuli dividing the receptive field into halves instead of checkerboard stimuli (Fig. 4.7 D, baseline of the exponential fit). Initially, the subunit grid is aligned in such a way that the midpoint of one subunit corresponds to the ganglion cell receptive field midpoint. The spatial phase of the subunit grating can be shifted in x- and y direction with respect to the midpoint of the RGC receptive field to account for different alignments of the subunit receptive fields with the stimulus (Fig. E.1 B). The maximum shift in each direction corresponds to a subunit radius. For bigger shifts the model becomes periodic.

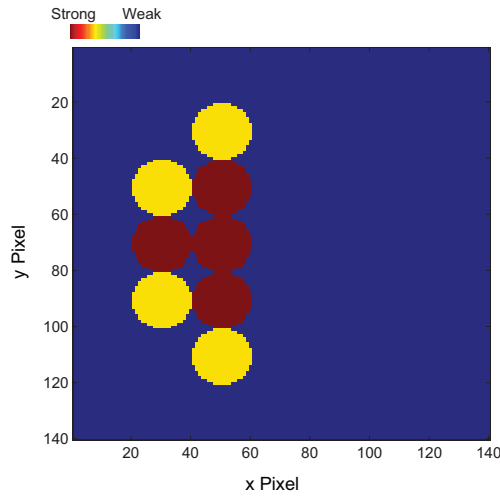


Figure E.2: Unweighted subunit responses elicited by a dark stimulation in the left half and a bright stimulation in the right half of the ganglion cell receptive field in case of symmetric subunit grid alignment. The central subunits do not contribute as they are stimulated with dark and bright contrasts on an equal area and integrate linearly. The bipolar cells which are dark-stimulated on their full receptive field contribute the strongest, the bipolar cells on the border of the receptive field are only piecewise stimulated.

The RGC input is the weighted sum of the subunit outputs. Each weight w_i is determined by the distance d_i of the midpoint of the i .th subunit to the ganglion cell receptive field midpoint via $w_i = N(d_i; 0, 100\mu m)$. Here, $N(d_i; \mu, \sigma)$ is the Gaussian distribution with mean μ and standard deviation σ . First, a checkerboard stimulus with $s_1 = 1$ and $s_2 = 0$ is presented and the response calculated. Then, the contrasts were set to $s_1 = -2s_2 = s$ and a search algorithm was used to find the value s for which the model yields the same response as in the first scenario. Thus, two points of the iso-response curve were determined (corresponding to polar angles of about 153.4° and 180°). From these points, the slope of the iso-response curve was calculated in the same way as we did with the experimental curves. A slope of 1 means linear integration while a slope of 0 means perfect rectification. For each checkerboard stimulus, 200 of these iso-response curves have been calculated. Each time, the displacement of the subunit grid to the stimulus was drawn randomly and the subunit weights were updated. We did that for a range of different stimuli varying the checkerboard square width. To do the simulation, the subunits and the stimulus were discretized into pixels, using a pixel width of $2\mu m$ per pixel (for the simulation with $20\mu m$ subunit diameter) or $5\mu m$ per pixel (for the other curves). We also verified that using a finer discretization does not change the results significantly.

F SYNAPTIC DEPRESSION MODEL

To quantify effects of synaptic depression, a computational model was created. Two subunits were assumed: the left subunit received the contrast signal presented in the left half of the receptive field, the right subunit the contrast signal in the right half. The subunit input $s_i(t)$ was convolved with a typical OFF cell temporal filter (see Fig. F.1), as determined by a spike-triggered average analysis. The resulting generator signal $g_i(t) = s_i(t) * STA(t)$ was considered to correspond to the subunit activation. The synapse was modeled as a certain pool of vesicles, which can be either in effective ($E(t)$) (i.e. currently used in transmission), inactive ($I(t)$), or recovered state ($R(t)$) (Tsodyks and Markram 1997).

The dynamics are described by

$$\begin{aligned}
 f_{eff \rightarrow inact} &= \frac{1}{\tau_{inact}} E(t) \\
 f_{inact \rightarrow recov} &= \frac{1}{\tau_{recov}} I(t) \\
 f_{recov \rightarrow eff} &= U \cdot R(t) \cdot \frac{N(g_i(t))}{C_{norm}} \\
 \frac{dE}{dt} &= -f_{eff \rightarrow inact} + f_{recov \rightarrow eff} \\
 \frac{dR}{dt} &= f_{inact \rightarrow recov} - f_{recov \rightarrow eff} \\
 I(t) &= 1 - E(t) - R(t).
 \end{aligned}$$

$E(t)$ is considered to be the subunit input to the RGC. The sum of the signals from both subunits resembles the resulting activation of the RGC, modeled as an integrate and fire neuron. $C_{norm} = 4$ is a normalization constant, set to be bigger than the maximal possible input into the synapse. $N(\cdot)$ is the static synaptic nonlinearity, assumed to be rectifying quadratic, as suggested by the measured iso-latency curves. U is a scaling parameter, which can be interpreted as the fraction of available vesicles triggered by the incoming signal per time. When modeling cells with convex iso-rate curves, U was set to $0.002/\Delta t$, for a Homogeneity detector to $0.04/\Delta t$. $\Delta t = 0.1$ ms is the simulation time step. The time constants were set to $\tau_{recov} = 4000$ ms and $\tau_{inact} = 4$ ms, similar to what was found in rat retinal ribbon synapses (Singer and Diamond 2006). The integrate and fire neuron is determined by the voltage equation

$$\tau_{membrane} \frac{dV}{dt} = R \cdot (E_{\text{left subunit}}(t) + E_{\text{right subunit}}(t)) - V(t) \quad \tau_{membrane} = 5ms, R = 1.$$

If V crosses threshold, a spike is elicited and the membrane potential is reset. Then there is an absolute refractory period of 3 ms. Crucial parameters are the spike threshold ϑ and the reset voltage V_{reset} . The spike threshold can be interpreted as the amount of effective vesicles

necessary to produce a spike. To model a convex iso-rate curve, good values turned out to be $\vartheta = 0.014$, $V_{reset} = -0.004$. With these, obtained iso-rate curves have the aspired shape and the effect of the pre-depressing stimulus has approximately the same magnitude as found in the experiment. To model a homogeneity detector iso-rate curve, the threshold was increased. This accounts for the hypothesized stronger synaptic depression: because more vesicles are needed per spike, the ready-releasable-pool depletes faster. The used parameters for a homogeneity detector cell are $\vartheta = 0.048$ and $V_{reset} = -0.0192$.

It turns out, that homogeneity detectors display a much stronger asymmetric scaling (Fig. F.1 **D** and **E**) than cells with convex iso-rate curves (Fig. F.1 **B** and **C**). However, this effect cannot be observed in our experimental data (Fig. 4.10). Therefore, synaptic depression seems not to be the origin of the non-convex shape of iso-rate curves in homogeneity detectors.

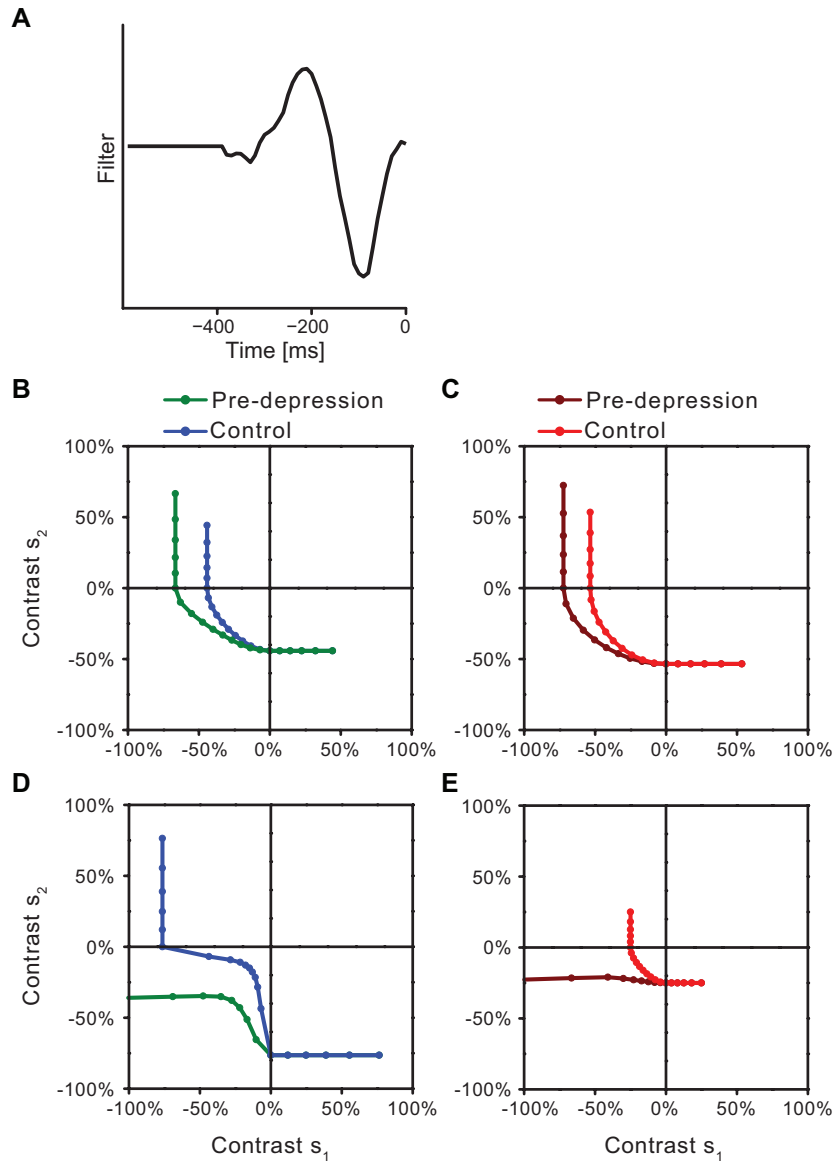


Figure F.1: Computational synaptic depression model. (A) Temporal filter ($STA(t)$) used to calculate the subunit activation $g_i(t) = s_i(t) * STA(t)$ produced by the input contrast $s_i(t)$. (B and C) Results of a cell with convex iso-rate curves. The model parameters are chosen to reproduce the shape of the iso-response curves as well as the effect of the pre-depressing stimuli. (B) Target response: 5 spikes. (C) Target response: 120 ms. (D and E) Iso-response curves of a homogeneity detector cell. All model parameters are the same as in B and C, except that the threshold of the integrate-and-fire neuron (and its reset voltage) was increased until the iso-rate curve (D, blue) displayed a prominent inward dip. (D) Target response: 5 spikes. (E) Target response: 120 ms. The effect of the pre-depressing stimuli turns out to be much bigger than in the cell with convex iso-rate curve, which is not what we observed experimentally.

G SHUNTING INHIBITION OF NARROW-FIELD AMACRINE CELLS

Here we discuss an implementation of the circuit model introduced in Fig. 4.14. As before, bipolar cell (BC) inputs are the contrast s_1 to BC 1 and s_2 to BC 2. The output is then nonlinearly derived by

$$B_{out,i}(s_i) = N(s_i) = \begin{cases} 0, & s_i < 0 \\ s_i^2, & s_i \geq 0 \end{cases}, \quad i = 1, 2.$$

This nonlinearity is inspired by the shape of iso-latency curves. The amacrine cell (AC) input $A_{in,i}(s_i)$ is assumed to be identical to the BC output, $A_{in,i}(s_i) = B_{out,i}(s_i)$. A priori, the amacrine cell output is an unspecified function of the input,

$$A_{out,i}(s_i) = G(A_{in,i}(s_i)) = G(B_{out,i}(s_i)).$$

Although here we discuss a static model without explicit consideration of time, a dynamic model would require to include a time delay of the amacrine cell output to ensure that the iso-latency curve is unaffected by the AC output. The amacrine cell output might now be acting as a local shunting inhibition. This is generally thought to have a divisive effect on the incoming excitation (Holt and Koch 1997, Doiron et al. 2001, Dayan and Abbott 2001):

$$R_{in,i}(s_i) = \frac{B_{out,i}(s_i)}{1 + A_{out,i}(s_i)}.$$

Here $R_{in,i}(s_i)$ is the RGC input of a single *subunit* (meaning a single circuit of BC and AC). The total RGC input is then

$$R_{in,total}(s_1, s_2) = \frac{B_{out,1}(s_1)}{1 + A_{out,1}(s_1)} + \frac{B_{out,2}(s_2)}{1 + A_{out,2}(s_2)}.$$

To discuss a concrete case, we assume that the amacrine cell output is a linear function of its input:

$$A_{out,i}(s_i) = m \cdot A_{in,i}(s_i) = m \cdot B_{out,i}(s_i).$$

For preferred contrasts $s_i > 0$, the RGC input of a single subunit would have the functional form

$$R_{in,i}(s_i) = \frac{s_i^2}{1 + m \cdot s_i^2},$$

which is a saturating monotonic function (see Fig. G.1 **A**). Iso-response curves are calculated to satisfy the equation

$$R_{in,total}(s_1, s_2) = C = \text{const},$$

(Fig. G.1 **B**). Different C correspond to different number of spikes in the experiment. Apparently the linear input output relation of the AC is sufficient to establish a non-convex iso-rate curve when assuming shunting inhibition.

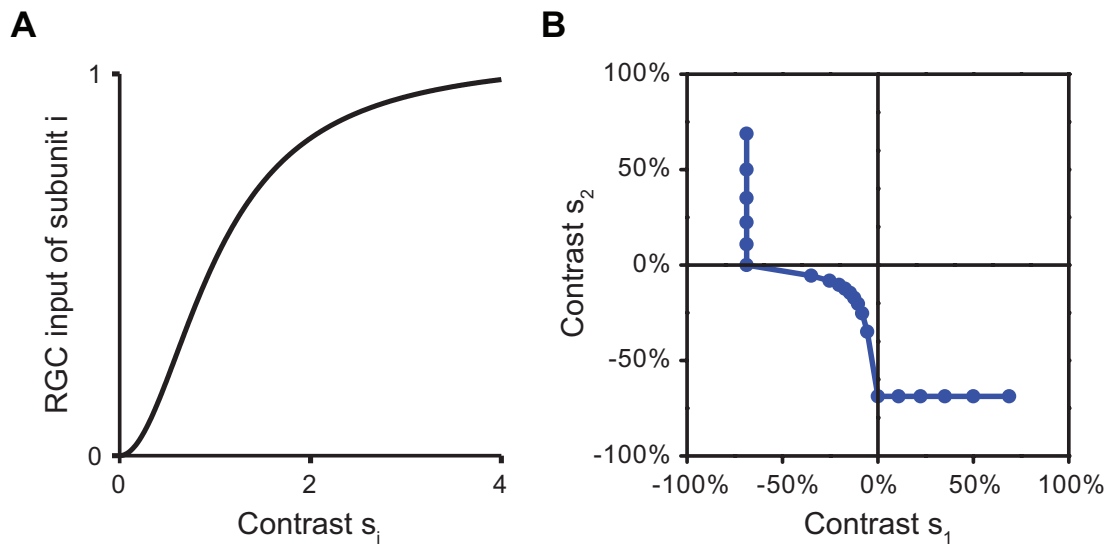


Figure G.1: Effect of shunting inhibition. **(A)** Dependence of the RGC input $R_{in,i}(s_i)$ from a single subunit on the input contrast s_i . Here $m = \frac{1}{1.05}$. **(B)** Iso-response curve for a linear AC ($C = 1$ and $m = \frac{1}{1.05}$).

H DIVISIVE OR SUBTRACTIVE INHIBITION LEADS TO IDENTICAL ISO-RESPONSE CURVES

In this chapter we demonstrate that the interpretation of the nonlinear effects obtained by iso-response curves does not depend on whether the surround acts subtractive or divisive. This can be seen in the following way.

If one assumes a subtractive effect of the surround, we can write the iso-response condition, equivalent to equation (3.3), as

$$N_{ctr}(s_{ctr}) - N_{srnd}(s_{srnd}) = const = r \rightarrow \frac{N_{ctr}(s_{ctr})}{r} - \frac{N_{srnd}(s_{srnd})}{r} = 1.$$

On the other hand, assuming a divisive integration leads to

$$\frac{N_{ctr}(s_{ctr})}{1 + N_{srnd}(s_{srnd})} = const = r \rightarrow \frac{N_{ctr}(s_{ctr})}{r} - \frac{N_{srnd}(s_{srnd})}{1} = 1.$$

In both cases an equation of the same shape is obtained, leading to indistinguishable iso-response curves (Fig. H.1). Only the scaling of iso-response curves when searching for different pre-specified responses r differs in both situations. The other way round, if we determine the properties of the surround nonlinearity from iso-response curves, we do not have to make an assumption of an either subtractive or divisive model. The same results are valid for both cases, only by rescaling the nonlinearity².

²If a subtractive and a divisive nonlinearity occur in the system, a mixture $N_{srnd}(s_{srnd}) = N_{subtr}(s_{srnd}) + r \cdot N_{div}(s_{srnd}) + N_{subtr}(s_{srnd}) \cdot N_{div}(s_{srnd})$ of both will be obtained.

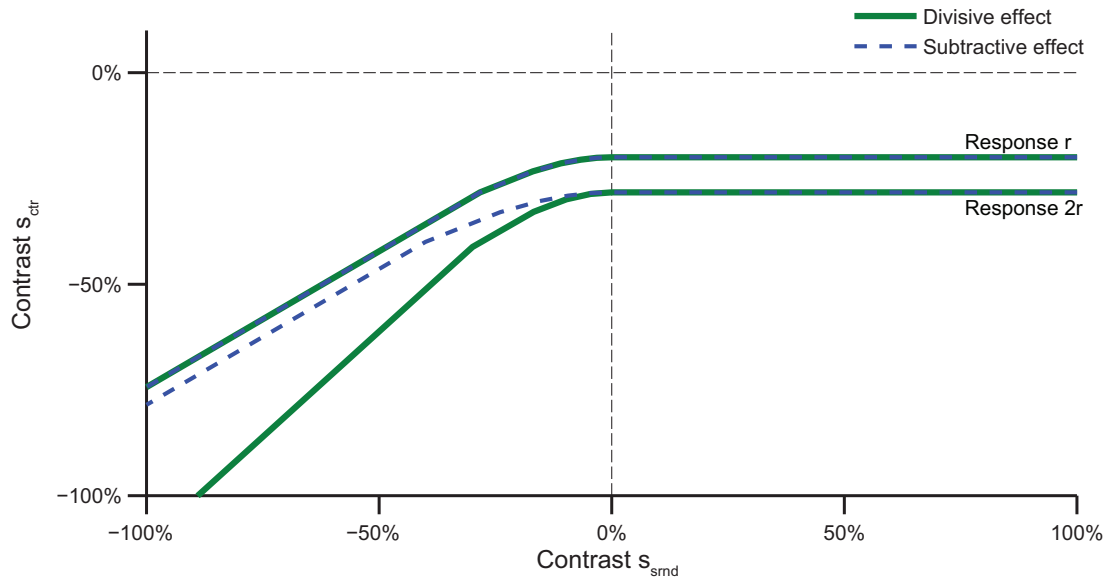


Figure H.1: Divisive and subtractive center-surround integration. For this plot, we assumed rectifying quadratic nonlinearities in both center and surround subunits, thus leading to the implicit iso-response equations $1 = \frac{|s_{ctr}|_+^2}{r} - \frac{|s_{srrnd}|_+^2}{r \cdot k}$ (subtractive) or $1 = \frac{|s_{ctr}|_+^2}{r} - \frac{|s_{srrnd}|_+^2}{k}$ (divisive), respectively. k is an additional scaling factor. Differences between the two models only emerge when comparing the scaling of iso-response curves for different responses r .

I LINEARITY OF CENTER-SURROUND ISO-RATE CURVES

Let us assume that the center nonlinearity $N_{ctr}(s_{ctr})$ as well as the surround nonlinearity $N_{srnd}(s_{srnd})$ can be well described by a power-law for negative surround contrasts. The implicit equation $N_{ctr}(s_{ctr}) - N_{srnd}(s_{srnd}) = const$ yields a linear behavior for $s_{srnd} \ll 0$ only if the exponents of both power-laws are identical. To illustrate this, let us calculate the slope of the implicit equation.

$$\begin{aligned}
 N_{ctr}(s_{ctr}) &\equiv (-s_{ctr})^a \\
 N_{srnd}(s_{srnd}) &\equiv (-s_{srnd})^b \\
 N_{ctr}(s_{ctr}) - N_{srnd}(s_{srnd}) = const &\rightarrow \frac{dN_{ctr}(s_{ctr})}{ds_{ctr}} \frac{ds_{ctr}}{ds_{srnd}} - \frac{dN_{srnd}(s_{srnd})}{ds_{srnd}} \\
 &= \frac{ds_{ctr}}{ds_{srnd}} = \frac{N'_{srnd}(s_{srnd})}{N'_{ctr}(s_{ctr})} = \frac{b(-s_{srnd})^{b-1}}{a(-s_{ctr})^{a-1}} \quad (8.1)
 \end{aligned}$$

$$\begin{aligned}
 N_{ctr}(s_{ctr}) - N_{srnd}(s_{srnd}) = const &\rightarrow -s_{ctr} = \left(const + (-s_{srnd})^b \right)^{1/a} \quad (8.2) \\
 \xrightarrow{(8.1) \text{ and } (8.2)} \frac{ds_{ctr}}{ds_{srnd}} &= \frac{b(-s_{srnd})^{b-1}}{a \left(const + (-s_{srnd})^b \right)^{\frac{a-1}{a}}} \\
 \xrightarrow{(-s_{srnd})^b \gg const} &\frac{b}{a} (-s_{srnd})^{(b-1) - (a-1)\frac{b}{a}}
 \end{aligned}$$

Hence, only for $a = b$ the slope of the implicit function becomes constant for $(-s_{srnd})^b \gg const$, and therefore only this case leads to an approximately linear behavior for dark surround contrasts.

J SUPPLEMENTARY METHODS

J.1 ONLINE IDENTIFICATION OF RECEPTIVE FIELD

The receptive field location is determined as described in chapter 3.3. Here the search algorithm is described which is used to find the position of the separation line where stimulation of both stimulation areas led to the same spiking response.

We started by choosing a separation line that simply cut the available stimulation area into equal halves. The search then proceeded in two phases. In phase 1, the separation line was shifted after each pair of stimuli by 40 pixels towards the side for which stimulation yielded more spikes. This was repeated until the first "sign change" was observed, that is, until that side yielded more spikes that had previously yielded less. In the following phase 2, 15 additional measurements were performed. After each measurement, the separation line was again shifted in the direction where more spikes were observed, but the number of pixels of this shift was chosen randomly from a uniform distribution between 1 and 20 pixels. The final midline of the receptive field was then determined by a linear fit of the spike count differences versus position of the separation line for the 15 measurements of phase 2.

J.2 ISO-RESPONSE MEASUREMENTS

In the following, we describe the line search along an individual search direction for a predefined spike count. Searches for predefined latencies were performed analogously.

The search algorithm proceeded similarly to the online estimation of the receptive field center spot. The search consisted of two phases. In phase 1, the radius r was increased step-by-step, starting from contrast zero, until the measured spike count was larger than the predefined response. The step size was 10% contrast for the larger of the two contrast values, while the smaller contrast changed correspondingly so that the fixed ratio of the two contrast values was preserved. In the subsequent phase 2, 15 further measurements were performed, and the contrast adjustment before each stimulus presentation was chosen randomly from a uniform distribution between 0 and 10%. Again, the larger of the two contrast values was adjusted by this amount while the smaller contrast value was changed accordingly so that the fixed ratio was preserved. The adjustment was used as a contrast increase if the previous spike count had been too small and as a decrease if it had been too large. If the response had been the exact target response, it was chosen at random whether the next step was an increase or decrease. Finally, the data from search phase 2 were fitted as described in chapter 3.3.

J.3 MODEL FITS OF SUBUNIT NONLINEARITY

To obtain the nonlinearities for the subunit model (insets of Fig. 4.2), we fitted the iso-response curves with a curve of the form

$$1 = \frac{1}{c_1^k} N(s_1) + \frac{1}{c_2^k} N(s_2). \quad (8.3)$$

Here, $N(\cdot)$ is the subunit nonlinearity, parameterized as given in equation (4.1). The variables m, k, ϑ are the free parameters of the nonlinearity, and c_1 and c_2 are scaling parameters that set the sensitivity along each of the axes in the two-dimensional stimulus space.

The parameter values were obtained by a standard maximum-likelihood fit. In short, to compute the likelihood, the model prediction for the radius $r = \sqrt{s_1^2 + s_2^2}$ was calculated for each experimentally used angle $\alpha = \tan^{-1}(s_2/s_1)$ by solving the above implicit Eq. (8.3) of the iso-response curve. The probability of each experimentally measured radius $r = \sqrt{s_1^2 + s_2^2}$ was then calculated by assuming that the data follow a Gaussian distribution with mean value given by the model prediction and standard deviation given by the experimental measurement error of r .

J.4 CALCULATION OF FORM FACTORS

We calculated form factors of the iso-response curves (Fig. 4.2 **E** and **F**) to quantify the extent and type of nonlinearity of the curves. The form factor compares the shape of the curve to the linear prediction, defined as the line between the two intersection points with the axes. It is larger or smaller than unity depending on whether the iso-response curve is convex or non-convex, respectively. The form factor was obtained in the following way. We first estimated the radius $r(\phi)$ for different polar angles by averaging the radius of all data points (typically three) with polar angles between -10° and $+10^\circ$. For the lower left diagonal, which corresponds to homogeneous dark stimulation, we obtained $r(225^\circ)$, and for the negative x axis and negative y axis, we obtained $r(180^\circ)$ and $r(270^\circ)$, respectively. The two latter values were then used to calculate the linear prediction for the radius along the lower left diagonal, $r_{pred}(225^\circ)$:

$$r_{pred}(225^\circ) = \sqrt{2} \frac{r(180^\circ) \cdot r(270^\circ)}{r(180^\circ) + r(270^\circ)}$$

The form factor is then calculated as the ratio $r(225^\circ)/r_{pred}(225^\circ)$.

J.5 SLOPE OF ISO-RATE CURVES FOR ASSESSMENT OF RECTIFICATION

To characterize the cells' rectification (Fig. 4.7), we calculated the average slope of each iso-rate curve in the regions where one contrast component was negative and the other positive. To

do so, the data points in the quadrant defined by $s_1 < 0$ and $s_2 \geq 0$ were fitted according to the linear regression model $s_1 = m_a \cdot (-s_2) + b_a$, and data points in the quadrant defined by $s_1 \geq 0$ and $s_2 < 0$ were fitted by $-s_2 = m_b \cdot s_1 + b_b$. The slope value that characterized the rectification of the iso-response curve was then obtained as the average of the fit parameters m_a and m_b . With the applied sign convention, a slope of zero corresponds to perfect half-wave rectification, whereas a slope of unity means no rectification, i.e., linear integration of s_1 and s_2 .

J.6 PRE-DEPRESSING STIMULI

In the experiments with the pre-depression stimulus (Fig. 4.10), each stimulus presentation used for the iso-response measurement was preceded by a brief dark flash (contrast = -40%) on one half of the receptive field. For experiments with 200-ms stimulation in the control case, the pre-depression stimulus lasted for 200 ms and was followed by a 300-ms pause; for experiments with 500-ms stimulation, pre-depression stimulus and pause each lasted 500 ms. Note that to measure the response in these experiments, only spikes from the actual iso-response stimulus were taken into account; spikes resulting from the pre-depression stimulus were not considered.

J.7 SIMULATION OF ISO-RESPONSE CURVES

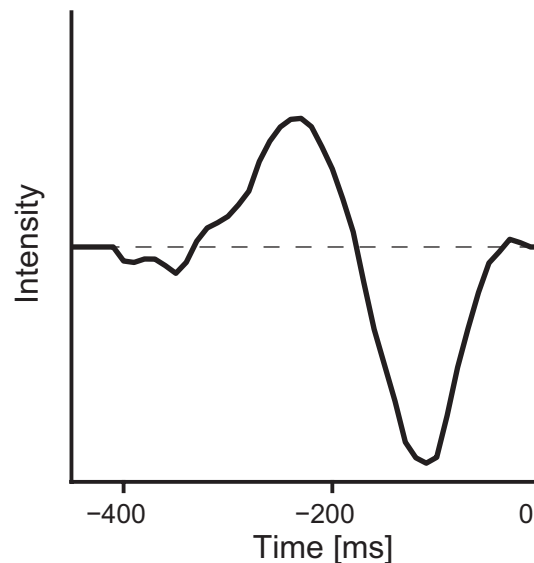


Figure J.1: Temporal subunit filter.

To simulate iso-response curves according to a circuit as shown in Fig. 4.14, we set up a computational model consisting of two independent subunits and one retinal ganglion cell. Each subunit i comprises an excitatory bipolar cell and an inhibitory amacrine cell. The bipolar cell input was modeled via a scalar intensity function which steps from 0 (gray) to s_i (positive values: bright contrasts; negative values: dark contrasts). This stimulus is then convolved with a biphasic temporal OFF-type filter to determine the bipolar cell activation level (Fig. J.1). Because the filter is biphasic, a dark stimulus leads to a transient bipolar cell excitation. The bipolar cell output $B_i(t)$ is determined by the half-wave rectified and squared activation level, as was found e.g. in iso-latency curves. This output signal serves as excitatory input to both ganglion cell and the amacrine cell. The amacrine cell is assumed to have low-pass filter characteristics. This accounts for the required time delay and also broadens the amacrine cell response. Thus, the amacrine cell activity $a_i(t)$ was calculated via $a_i(t) = a_i(t - \Delta t) + \alpha(B_i(t) - a_i(t - \Delta t))$ at each time step. The simulation time step was set to $\Delta t = 0.1ms$ and $\alpha = 5 \cdot 10^{-3}$. The output of the amacrine cell $AC_i(t)$ was also determined by the half-wave rectified, squared and scaled activation, $AC_i(t) = |a_i(t)|_+^2/15$. This nonlinearity was chosen to reproduce the experimental findings and might originate in the same mechanisms as the bipolar cell output nonlinearity. The total subunit output is the rectified difference of excitatory bipolar cell output and inhibitory amacrine cell output. Hence, the RGC input is given by $RGC(t) = |B_1(t) - AC_1(t)|_+ + |B_2(t) - AC_2(t)|_+$. The spike generation mechanism is modeled by scaling and a simple threshold crossing, i.e. the response PSTH of the cell in Hz is given by $PSTH(t) = |RGC(t) - \vartheta| \cdot 20$. The threshold is set to $\vartheta = 6$. Thus, the first-spike latency corresponds to the time point at which the RGC activation crosses threshold. The number of spikes is the integral of the PSTH. To model iso-response curves recorded with inhibition blockers, the amacrine cell output was set to zero (Fig 4.14 C, orange curve). To reproduce the scenario with a less efficient stimulus (Fig 4.14 C, green curve), the RGC input was divided by a factor of 4.

J.8 ESTIMATE OF THE SURROUND NONLINEARITIES

To fit the measured iso-latency curve (Fig. 5.4), the excitatory center nonlinearity was modeled as

$$N_{ctr}(s_{ctr}) = \begin{cases} (-s_{ctr}/s_y)^\xi & , s_{ctr} < 0 \\ 0 & , s_{ctr} \geq 0 \end{cases} . \quad (8.4)$$

The surround excitatory nonlinearity fitted to the measured iso-latency curve via $N_{ctr}(s_{ctr}) + N_{srnd}(s_{srnd}) = 1$ was chosen as

$$N_{srnd}(s_{srnd}) = \begin{cases} m \cdot (s_{srnd} - \vartheta)/s_x + (-(s_{srnd} - \vartheta)/s_x)^k & , s_{srnd} < \vartheta \\ m \cdot (s_{srnd} - \vartheta)/s_x & , s_{srnd} \geq \vartheta \end{cases} . \quad (8.5)$$

The model parameters ξ, k, ϑ, m as well as the scaling parameters s_x and s_y were estimated by a maximum likelihood estimate in the same way as described in section J.3. Because of the high dimensionality of the parameter space, the fit was quite dependent on the chosen starting values. Thus, we do not claim that the obtained solution is optimal in the sense of corresponding to the global maximum of the likelihood.

J.9 PIECEWISE LINEAR FIT OF ISO-RATE CURVES AND CALCULATION OF THE AVERAGE CURVE

In order to compare the slopes of the different regions of iso-rate curves, a piecewise linear model was fitted to the data. Therefore, the data were divided into three parts: the right part contained data points with $s_{srnd} > 10\%$, the central part data points with $-10\% < s_{srnd} < 10\%$ and the left part data points with $s_{srnd} < -10\%$. In the latter, only data that lie right of the point with the minimal center contrast were taken into account in order to ignore data points constituting the rebound upsurge. Additionally, only data points with contrasts $-100\% < s_i < 100\%$ ($i=ctr/srnd$) were taken into account. All data within one region were then fitted to a linear function $s_{ctr} = m \cdot s_{srnd} + b$. No continuity constraints were imposed. The resulting slopes m were then used to create the histograms of Fig. 5.6.

The data points (s_{srnd}, s_{ctr}) of all curves that were taken into account for the fitting were subsequently binned according to the s_{srnd} value. The bin size was adapted in such a way that each bin contained 100 data points. The data points of the mean curve (Fig. 5.5) corresponded to the average s_{srnd} and s_{ctr} value in each bin.

J.10 CENTER-SURROUND PSTH MEASUREMENTS

To obtain the PSTHs in Fig. 5.7 **A**, first an iso-rate curve was measured. From this curve, three stimuli were chosen: one with no surround stimulation (orange), one with homogeneous stimulation of center and surround (black) and one with dark surround stimulation only (green). Each stimulus was presented 30 times in a randomized fashion. Because repeated measurements of the same stimuli often distorted the responsiveness of the cell, the spike counts were compared and the stimuli updated in order to re-establish the iso-rate condition. Then the measurement was repeated. The procedure stopped when the iso-rate condition was fulfilled with an accuracy of more than 90% and only these trials were then used for the PSTHs. In contrast, PSTHs in Fig. 5.7 **B** were measured without imposing an iso-rate condition. Eight stimuli were chosen with a fixed surround contrast. Thereby, the surround contrast corresponded to the contrast value at the intersection of the iso-rate curve and the negative x axis. The center

contrasts were equally spaced in an interval from zero to the minimum center contrast found in the iso-rate curve. 25 trials of each stimulus were measured randomized in such a way that after each multiple of 8 trials, each stimulus was presented equally often.

J.11 CENTER-SURROUND REBOUND SPIKE MODEL

The computational model of Fig. 5.8 A is composed of an OFF bipolar cell in the center and in the surround, as well as one wide-field amacrine cell receiving excitatory input from both OFF bipolar cells, and one retinal ganglion cell which pools input from bipolar and amacrine cells. The inputs to the bipolar cells correspond to the contrasts shown in center or surround, respectively. The output B_i , $i \in \{ctr, srnd\}$ of bipolar cells is calculated from the input s_i by imposing a rectifying quadratic nonlinearity

$$B_i = \begin{cases} (-s_i)^2, & s_i < 0 \\ 0, & s_i \geq 0 \end{cases} .$$

The OFF amacrine cell is modeled with a linear input output function. Although center and surround bipolar cells are assumed to contribute with the same weight to the amacrine cell input, the output of the surround bipolar cell is taken into account more strongly to account for the bigger size of the surround. Thus, the amacrine cell output is given as $A = B_{ctr} + \beta \cdot B_{srnd}$ with $\beta = 3$. The ganglion cell pools excitation from center and surround via $Exc_{RGC} = B_{ctr} + \alpha \cdot B_{srnd}$ with $\alpha = 0.25$. The value of α reflects the smaller excitatory input weight bipolar cells in the surround have compared to center bipolar cells. The inhibition Inh_{RGC} received by the ganglion cell corresponds to the amacrine cell output A .

To introduce a temporal dimension in the model, the time courses of excitation $K_{exc}(t) = N(t; \mu, \sigma)$ and inhibition $K_{inh}(t) = N(t; \mu + 30 \text{ ms}, \sigma)$ are assumed to have a Gaussian profile $N(t; \mu, \sigma)$ ($\sigma = 60 \text{ ms}$ standard deviation, $\mu = 300 \text{ ms}$ mean), with inhibition being 30 ms delayed. The RGC membrane voltage is then given as $V_{RGC}(t) = Exc_{RGC} \cdot K_{exc}(t) - \gamma \cdot Inh_{RGC} \cdot K_{inh}(t)$. The parameter $\gamma = 0.225$ describes the relative effectiveness of inhibition. Spikes are generated either if the voltage is bigger than $\vartheta_{AP} = 5 \cdot 10^{-4}$ or smaller than a rebound threshold $\vartheta_{RB} = -2.5$. Thus, the PSTH in Hz is calculated as

$$PSTH(t) = 1000 \cdot \begin{cases} V_{RGC}(t), & V_{RGC}(t) > \vartheta_{AP} \\ -V_{RGC}(t), & V_{RGC}(t) < \vartheta_{RB} \\ 0, & \text{otherwise} \end{cases} .$$

The factor 1000 stems from the fact that the time step of the temporal kernels was set to $\Delta t = 1 \text{ ms}$. The number of spikes generated is assumed to be simply the integral of the PSTH,

$$\text{spike count} = \int PSTH(t) dt = \sum PSTH(t) \Delta t = \sum PSTH(t) / \text{Hz} / 1000.$$

For the iso-response curves, the aspired response was set to 10 spikes or 170 ms latency, respectively. All scaling factors have been determined heuristically to reproduce the experimentally observed behaviors.

J.12 HORIZONTAL CELL MODEL

The computational model of Fig. 5.8 **B** is composed of one OFF bipolar cell in the center and one in the surround, one horizontal cell and one ganglion cell. All signals are modeled as square pulses, which allows us to control the height and the duration in more detail. In particular, the height of the excitatory bipolar cell input pulse corresponds to the photoreceptor output value s_i , and its duration is calculated via

$$\text{Duration: } 41 + 12 \cdot \exp(s_i/4.7).$$

We assume the horizontal cell to linearly pool the center and surround inputs. Thus, the horizontal cell output to the bipolar cell dendrites or photoreceptor terminals is a function of $I_{HC} = -(s_{ctr} + s_{srnd})$. The inhibitory pulse has a height of I_{HC} , and duration and latency are determined by

$$\text{Duration: } 39 + 25 \cdot 10^{-6} \cdot \exp(I_{HC}/0.3)$$

$$\text{Latency: } 9.7 + 372 \cdot \exp(-I_{HC}/0.7)$$

Thereby, the latency is calculated with respect to the onset of the excitation (see below).

The total bipolar cell input is then assumed to be the difference of the excitatory and the inhibitory pulse. The bipolar cell output $B_i(t)$ is determined by imposing a rectifying-quadratic nonlinearity. The RGC sums over the signals from both bipolar cells, $I_{RGC}(t) = 2B_{ctr}(t) + \frac{4}{9}B_{srnd}(t)$.

The latency of the spiking response is furthermore calculated as

$$\text{Latency: } 117 + 120 \cdot \exp(-\max(I_{RGC}(t))/3),$$

and the number of generated spikes is then calculated as the integral over the pulse.

All the numerical values in the equations above are determined by a further simplifying analytical calculation. The exponential behaviors of the latencies are inspired by experimental findings, as can be seen e.g. in Fig. 3.12 **C**. For the iso-response curves, the aspired response was set to 10 spikes or 170ms latency, respectively.

BIBLIOGRAPHY

- Adrian ED and Zotterman Y (1926) The impulses produced by sensory nerve-endings: Part ii. the response of a single end-organ, *Journal of physiology* **61**:151–171.
- Armstrong-Gold CE and Rieke F (2003) Synaptic depression and the kinetics of exocytosis in retinal bipolar cells, *Journal of Neuroscience* **23**:3796–3806.
- Baccus SA, Ölveczky BP, Manu M, and Meister M (2008) A retinal circuit that computes object motion, *Journal of Neuroscience* **28**:6807–6817.
- Baccus SA and Meister M (2002) Fast and slow contrast adaptation in the retinal circuitry, *Neuron* **36**:909–919.
- Baldrige WH, Vaney DI, and Weiler R (1998) The modulation of intercellular coupling in the retina, *Semin. Cell. Dev. Biol.* **9**:311–318.
- Banks MS, Geisler WS, and Bennett PJ (1987) The physical limits of grating visibility, *Vision Research* **27**:1915–1924.
- Barlow HB (1950) The receptive fields of ganglion cells in the frog retina, *XVIII Int. Physiol. Congress, Copenhagen* pages 88–89.
- Barlow HB (1953) Summation and inhibition in the frog's retina, *Journal of physiology* **119**:69–88.
- Barlow HB and Levick WR (1969) Changes in the maintained discharge with adaptation level in the cat retina, *Journal of physiology* **202**:699–718.
- Beaudoin DL, Borghuis BG, and Demb JB (2007) Cellular basis for contrast gain control over the receptive field center of mammalian retinal ganglion cells, *Journal of neuroscience* **27**:2636–2645.
- Bellavance MA, Demers M, and Deschenes M (2010) Feedforward inhibition determines the angular tuning of vibrissal responses in the principal trigeminal nucleus, *Journal of Neuroscience* **30**:1057–1063.

- Benda J, Gollisch T, Machens CK, and Herz AVM (2007) From response to stimulus: adaptive sampling in sensory physiology, *Current opinion in neurobiology* **17**(4):430–436.
- Berry MJ and Meister M (1999) The neural code of the retina, *Neuron* **22**:435–450.
- Bialek W and Rieke F (1992) Reliability and information transmission in spiking neurons, *Trends in neurosciences* **15**:428–434.
- Bölinger D and Gollisch T (2011a) Closed-loop measurements of iso-response stimuli reveal dynamic nonlinear stimulus integration by retinal ganglion cells, *Neuron*, in press.
- Bölinger D and Gollisch T (2011b) Iso-response stimuli reveal nonlinearities in center-surround integration in the retina, in prep.
- Borst A and Euler T (2011) Seeing things in motion: models, circuits, and mechanisms, *Neuron* **71**:974–994.
- Burkhardt DA and Fahey PK (1998) Contrast enhancement and distributed encoding by bipolar cells in the retina, *Journal of Neurophysiology* **80**:1070–1081.
- Burkhardt DA, Fahey PK, and Sikora M (1998) Responses of ganglion cells to contrast steps in the light-adapted retina of the tiger salamander, *Visual Neuroscience* **15**:219–229.
- Burkhardt DA, Fahey PK, and Sikora MA (2007) Retinal bipolar cells: Temporal filtering of signals from cone photoreceptors, *Visual Neuroscience* **24**:765–774.
- Burr DC, Morrone MC, and Ross J (1994) Selective suppression of the magnocellular visual pathway during saccadic eye movements, *Nature* **371**:511–513.
- Burrone J and Lagnado L (2000) Synaptic depression and the kinetics of exocytosis in retinal bipolar cells, *Journal of Neuroscience* **20**:568–578.
- Cafaro J and Rieke F (2010) Noise correlations improve response fidelity and stimulus encoding, *Nature* **468**:964–967.
- Chen X, Hsueh HA, Greenberg K, and Werblin FS (2010) Three forms of spatial temporal feedforward inhibition are common to different ganglion cell types in rabbit retina, *Journal of Neurophysiology* **103**:2618–2632.
- Chichilnisky EJ (2001) A simple white noise analysis of neuronal light responses, *Network: Computation in Neural Systems* **12**:199–213.
- Cook PB and McReynolds JS (1998) Lateral inhibition in the inner retina is important for spatial tuning of ganglion cells, *Nature Neuroscience* **1**:714–719.

- Crook JD, Peterson BB, Packer OS, Robinson FR, Troy JB, and Dacey DM (2008) Y-cell receptive field and collicular projection of parasol ganglion cells in macaque monkey retina, *Journal of Neuroscience* **28**:11277–11291.
- Cruikshank SJ, Lewis TJ, and Connors BW (2007) Synaptic basis for intense thalamocortical activation of feedforward inhibitory cells in neocortex, *Nature Neuroscience* **10**:462–468.
- Dayan P and Abbott LF (2001) *Theoretical Neuroscience: Computational and Mathematical Modeling of Neural Systems*, Cambridge: MIT Press.
- de Charms RC, Maeda F, Glover GH, Ludlow D, Pauly JM, Soneji D, Gabrieli JDE, and Mackey SC (2005) Control over brain activation and pain learned by using realtime functional mri, *PNAS* **102**:18626–18631.
- de Schutter E and Bower JM (1994) An active membrane model of the cerebellar purkinje cell. i. simulation of current clamps in slice., *Journal of Neurophysiology* **71**:375–400.
- Demb JB (2008) Functional circuitry of visual adaptation in the retina, *Journal of physiology* **586**:4377–4384.
- Demb JB, Zaghoul K, Haarsma L, and Sterling P (2001) Bipolar cells contribute to nonlinear spatial summation in the brisk-transient (y) ganglion cell in mammalian retina, *Journal of Neuroscience* **21**:7447–7454.
- Doiron B, Longtin A, Berman N, and Maler L (2001) Subtractive and divisive inhibition: effect of voltage-dependent inhibitory conductances and noise., *Neural computation* **13**(1):227–248.
- Donner K and Grönholm ML (1984) Center and surround excitation in the receptive fields of frog retinal ganglion cells, *Vision Research* **24**:1807–1819.
- Dowling JE and Boycott BB (1969) Retinal ganglion cells: a correlation of anatomical and physiological approaches, *UCLA Forum Med. Sci.* **8**:145–161.
- Dowling JE and Dubin MW (2011) The Vertebrate Retina, *Comprehensive Physiology*, pages 317–339.
- Dreosti E, Esposti F, Baden T, and Lagnado L (2011) In vivo evidence that retinal bipolar cells generate spikes modulated by light, *Nature Neuroscience* **14**:951–952.
- Duebel J, Haverkamp S, Schleich W, Feng G, Augustine GJ, Kuner T, and Euler T (2006) Two-photon imaging reveals somatodendritic chloride gradient in retinal on-type bipolar cells expressing the biosensor clomeleon, *Neuron* **49**:81–94.

- Enroth-Cugell C and Freeman AW (1987) The receptive-field spatial structure of cat retinal y cells, *Journal of Physiology* **384**:49–79.
- Enroth-Cugell C and Jakiela HG (1980) Suppression of cat retinal ganglion cell responses by moving patterns, *Journal of Physiology* **302**:49–72.
- Enroth-Cugell C and Lennie P (1975) The control of retinal ganglion cell discharge by receptive field surrounds, *Journal of physiology* **247**:551–578.
- Enroth-Cugell C and Robson JG (1966) The contrast sensitivity of retinal ganglion cells of the cat, *Journal of Physiology* **187**:517–552.
- Fahey PK and Burkhardt DA (2003) Center-surround organization in bipolar cells: Symmetry for opposing contrasts, *Visual Neuroscience* **20**:1–10.
- Famiglietti EV (1983) Starburst amacrine cells and cholinergic neurons: mirror-symmetric on and off amacrine cells of rabbit retina, *Brain Research* **261**:138–144.
- Famiglietti EV and Kolb H (1975) A bistratified amacrine cell and synaptic circuitry in the inner plexiform layer of the retina, *Brain Research* **84**:293–300.
- Field GD and Chichilnisky EJ (2007) Information processing in the primate retina: circuitry and coding, *Annu. Rev. Neurosci.* **30**:1–30.
- Field GD, Gauthier JL, Sher A, Greschner M, Machado TA, Jepsen LH, Shlens J, Gunning DE, Mathieson K, Dabrowski W, Paninski L, Litke AM, and Chichilnisky EJ (2010) Functional connectivity in the retina at the resolution of photoreceptors, *Nature* **467**:673–677.
- Flores-Herr N, Protti DA, and Wässle H (2001) Synaptic currents generating the inhibitory surround of ganglion cells in the mammalian retina, *Journal of Neuroscience* **21**:4852–4863.
- Franke F, Natora M, Boucsein C, Munk MH, and Obermayer K (2010) An online spike detection and spike classification algorithm capable of instantaneous resolution of overlapping spikes, *J Comput Neurosci* **29**:127–148.
- Franze K, Grosche J, Skatchkov SN, Schinkinger S, Foja C, Schild D, Uckermann O, Travis K, Reichenbach A, and Guck J (2007) Muller cells are living optical fibers in the vertebrate retina, *Proc. Natl. Acad. Sci. USA* **104**:8287–8292.
- Frumkes TE and Miller RF (1979) Pathways and polarities of synaptic interactions in the inner retina of the mudpuppy: Ii. insight revealed by an analysis of latency and threshold, *Brain Research* **161**:13–24.

- Gabernet L, Jadhav SP, Feldman D, Carandini M, and Scanziani M (2005) Somatosensory integration controlled by dynamic thalamocortical feed-forward inhibition, *Neuron* **48**:315–327.
- Geffen MN, de Vries SE, and Meister M (2007) Retinal ganglion cells can rapidly change polarity from off to on, *PLoS Biology* **5**:e65.
- Gollisch T and Herz AVM (2005) Disentangling sub-millisecond processes within an auditory transduction chain, *PLoS Biology* **3**(8):e8.
- Gollisch T and Meister M (2008) Rapid neural coding in the retina with relative spike latencies, *Science* **319**:1108–1111.
- Gollisch T and Meister M (2010) Eye smarter than scientists believed: neural computations in circuits of the retina, *Neuron* **65**:150–164.
- Gollisch T, Schütze H, Benda J, and Herz AVM (2002) Energy integration describes sound-intensity coding in an insect auditory system, *Journal of Neuroscience* **22**(23):10434–10448.
- Grüsser OJ and Grüsser-Cornehls U (1973) Neuronal mechanisms of visual movement perception and some psychophysical and behavioral correlations, in *Handbook of Sensory Physiology*, volume VII/3A, chapter Central Processing of Visual Information, part A, Springer: Berlin.
- Haller S, Birbaumer N, and Veit R (2010) Real-time fmri feedback training may improve chronic tinnitus, *Eur. Radiol.* **20**:696–703.
- Hare WA, Lowe JS, and Owen G (1986) Morphology of physiologically identified bipolar cells in the retina of the tiger salamander, *Journal of Comparative Neurology* **252**:130–138.
- Haverkamp S and Wässle H (2004) Characterization of an amacrine cell type of the mammalian retina immunoreactive for vesicular glutamate transporter 3, *Journal of comparative neurology* **468**:251–263.
- Herz AV, Gollisch T, Machens CK, and Jaeger D (2006) Modeling single-neuron dynamics and computations: a balance of detail and abstraction, *Science* **314**:80–85.
- Hochstein S and Shapley RM (1976) Linear and nonlinear spatial subunits in y cat retinal ganglion cells, *Journal of Physiology* **262**:265–284.
- Holt GR and Koch C (1997) Shunting inhibition does not have a divisive effect on firing rates, *Neural computation* **9**(5):1001–1013, please note that the title might be misleading. The

paper shows that the effect of shunting inhibition on firing rates is subtractive although the effect on subthreshold membrane potential is divisive.

Ichinose T and Lukasiewicz PD (2005) Inner and outer retinal pathways both contribute to surround inhibition of salamander ganglion cells, *Journal of Physiology* **565**:517–535.

Ishikane H, Gangi M, Honda S, and Tachibana M (2005) Synchronized retinal oscillations encode essential information for escape behavior in frogs, *Nature Neuroscience* **8**:1087–1095.

Ishikane H, Kawana A, and Tachibana M (1999) Short- and long-range synchronous activities in dimming detectors of the frog retina, *Visual Neuroscience* **16**:1001–1014.

Jarsky T, Cembrowski M, Logan SM, Kath WL, Rieke H, Demb JB, and Singer JH (2011) A synaptic mechanism for retinal adaptation to luminance and contrast, *Journal of Neuroscience* **31**:11003–11015.

Johnson J, Sherry DM, Liu X, Fremeau RT, Seal RP, Edwards RH, and Copenhagen DR (2004) Vesicular glutamate transporter 3 expression identifies glutamatergic amacrine cells in the rodent retina, *Journal of comparative neurology* **477**:386–398.

Keating MJ and Gaze RM (1970) Observations on the 'surround' properties of the receptive fields of frog retinal ganglion cells., *Q. J. Exp. Physiol. Cogn. Med. Sci.* **55**:129–142.

Kier CK, Buchsbaum G, and Sterling P (1995) How retinal microcircuits scale for ganglion cells of different size, *Journal of Neuroscience* **15**:7673–7683.

Kim KJ and Rieke F (2001) Temporal contrast adaptation in the input and output signals of salamander retinal ganglion cells, *Journal of Neuroscience* **21**:287–299.

Kolb H, Linberg KA, and Fisher SK (1992) The neurons of the human retina: a golgi study, *Journal of comparative neurology* **318**:147–187.

Kolb H, Nelson R, and Mariani A (1981) Amacrine cells, bipolar cells and ganglion cells of the cat retina: A golgi study., *Vision Research* **21**:1081–1114.

Korenberg MJ and Hunter IW (1986) The identification of nonlinear biological systems: Lnl cascade models, *Biological Cybernetics* **55**:125–134.

Kuffler SW (1953) Discharge patterns and functional organization of mammalian retina, *Journal of Neurophysiology* **16**:37–68.

- Lindstrom SH, Nacsa N, Blankenship T, Fitzgerald PG, Weller C, Vaney DI, and Wilson M (2009) Distribution and structure of efferent synapses in the chicken retina, *Visual Neuroscience* **26**:215–226.
- Ölveczky BP, Baccus SA, and Meister M (2003) Segregation of object and background motion in the retina, *Nature* **423**:401–408.
- Machens CK, Gollisch T, Kolesnikova O, and Herz AV (2005) Testing the efficiency of sensory coding with optimal stimulus ensembles, *Neuron* **47**:447–456.
- Makino CL, Taylor WR, and Baylor DA (1991) Rapid charge movements and photosensitivity of visual pigments in salamander rods and cones, *Journal of Physiology* **442**:211–234.
- Mangel SC (1991) Analysis of the horizontal cell contribution to the receptive field surround of ganglion cells in the rabbit retina, *Journal of Physiology* **442**:761–780.
- Manookin MB and Demb JB (2006) Presynaptic mechanism for slow contrast adaptation in mammalian retinal ganglion cells, *Neuron* **50**:453–464.
- Mante V, Frazor RA, Bonin V, Geisler WS, and Carandini M (2005) Independence of luminance and contrast in natural scenes and in the early visual system, *Nature Neuroscience* **8**:1690–1697.
- Manu M and Baccus SA (2011) Disinhibitory gating of retinal output by transmission from an amacrine cell, *Proc Natl Acad Sci U S A* .
- Mariani AP (2008) Photoreceptors of the larval tiger salamander retina, *Proc R Soc Lond B Biol Sci.* **227**:483–492.
- Martinez-Conde S, Macknik SL, and Hubel DH (2004) The role of fixational eye movements in visual perception, *Nature Reviews. Neuroscience.* **5**:229–240.
- Masland RH (2001) The fundamental plan of the retina, *Nature Neuroscience* **4**:877–886.
- Masland RH and Tauchi M (1986) The cholinergic amacrine cell, *Trends in neurosciences* **9**:218–223.
- McMahon MJ, Packer OS, and Dacey DM (2004) The classical receptive field surround of primate parasol ganglion cells is mediated primarily by a non-gabaergic pathway, *Journal of Neuroscience* **24**:3736–3745.
- Meister M, Pine J, and Baylor DA (1994) Multi-neuronal signals from the retina: acquisition and analysis, *Journal of Neuroscience Methods* **51**:95–106.

- Merwine DK, Amthor FR, and Grzywacz NM (1995) Interaction between center and surround in rabbit retinal ganglion cells, *Journal of Neurophysiology* **73**:1547–1567.
- Mitra P and Miller F (2007a) Mechanism underlying rebound excitation in retinal ganglion cells, *Visual Neuroscience* **24**:709–731.
- Mitra P and Miller F (2007b) Normal and rebound impulse firing in retinal ganglion cells, *Visual Neuroscience* **24**:79–90.
- Münch TA, da Silveira RA, Siebert S, Viney TJ, Awatramani GB, and Roska B (2009) Approach sensitivity in the retina processed by a multifunctional neural circuit, *Nature Neuroscience* **12**:1308–1316.
- Molnar A, Hsueh HA, Roska B, and Werblin FS (2009) Crossover inhibition in the retina: circuitry that compensates for nonlinear rectifying synaptic transmission, *Journal of Computational Neuroscience* **27**:569–590.
- Morrison JD (1975a) The effects of adaptation on the centre and surround responses of frog retinal ganglion cells, *Vision Research* **15**:1345–1348.
- Morrison JD (1975b) The responses of the retinal ganglion cells of the frogs, *Vision Research* **15**:1339–1344.
- Nakajima Y, Iwakabe H, Akazawa C, Nawa H, Shigemoto R, Mizuno N, and Nakanishi S (1993) Molecular characterization of a novel retinal metabotropic glutamate receptor mglur6 with a high agonist selectivity for 1-2-amino-4-phosphonobutyrate, *Journal of Biological Chemistry* **268**:11868–11873.
- Nelson R (1973) A comparison of electrical properties of neurons in necturus retina, *Journal of Neurophysiology* **36**:519–535.
- Nelson R (1982) Aii amacrine cells quicken the time course of rod signals in the cat retina, *Journal of Neurophysiology* **47**:928–947.
- Nemenman I, Lewen GD, Bialek W, and de Ruyter van Steveninck RP (2008) Neural coding of natural stimuli: information at sub-millisecond resolution, *PLoS Computational Biology* **4**:e1000025.
- Oesch NW and Diamond JS (2011) Ribbon synapses compute temporal contrast and encode luminance in retinal rod bipolar cells, *Nat Neurosci* .
- Olshausen BA and Field DJ (2005) How close are we to understanding v1?, *Neural Computation* **17**:1665–1699.

- Pandarinath C and Nirenberg S (2010) A retinal prosthetic strategy with the capacity to restore normal vision: Quantifying the effects of the encoder and transducer, *Neuroscience Meeting Planner. San Diego, CA: Society for Neuroscience. Program No. 891.4. Online.*
- Perkel DH and Bullock TH (1968) Neural coding, *Neurosci. Res. Program. Bull.* **6**:221–348.
- Perry RJ and McNaughton PA (1991) Response properties of cones from the retina of the tiger salamander, *Journal of Physiology* **433**:561–587.
- Pillow JW, Shlens J, Paninski L, Sher A, Litke AM, Chichilnisky EJ, and Simoncelli EP (2008) Spatio-temporal correlations and visual signalling in a complete neuronal population, *Nature* **454**:995–999.
- Porter JT, Johnson CK, and Agmon A (2001) Diverse types of interneurons generate thalamus-evoked feedforward inhibition in the mouse barrel cortex, *Journal of Neuroscience* **21**:2699–2710.
- Pouille F and Scanziani M (2001) Enforcement of temporal fidelity in pyramidal cells by somatic feed-forward inhibition, *Science* **293**:1159–1163.
- Pouzat C, Mazor O, and Laurent G (2002) Using noise signature to optimize spike-sorting and to assess neuronal classification quality, *Journal of Neuroscience Methods* **122**:43–57.
- Pugh EN, Nikonov S, and Lamb TD (1999) Molecular mechanisms of vertebrate photoreceptor light adaptation, *Current opinion in neurobiology* **9**:410–418.
- Rieke F (2001) Temporal contrast adaptation in salamander bipolar cells, *Journal of neuroscience* **21**:9445–9454.
- Riesenhuber M and Poggio T (2000) Models of object recognition, *Nature Neuroscience* **3**:1199–1204.
- Roska B, Molnar A, and Werblin FS (2006) Parallel processing in retinal ganglion cells: how integration of space-time patterns of excitation and inhibition form the spiking output, *Journal of Neurophysiology* **95**:3810–3822.
- Roska B, Nemeth E, Orzo L, and Werblin FS (2000) Three levels of lateral inhibition: A space-time study of the retina of the tiger salamander, *Journal of neuroscience* **20**:1941–1951.
- Roska B and Werblin F (2003) Rapid global shifts in natural scenes block spiking in specific ganglion cell types., *Nature Neuroscience* **6**:600–608.
- Sagdullaev BT and McCall MA (2005) Stimulus size and intensity alter fundamental receptive-field properties of mouse retinal ganglion cells in vivo, *Visual Neuroscience* **22**:649–659.

- Saglam M, Hayashida Y, and Murayama N (2009) A retinal circuit model accounting for wide-field amacrine cells, *Cognitive Neurodynamics* **3**(1):25–32.
- Sakuranaga M and Naka K (1985) Signal transmission in the catfish retina. i. transmission in the outer retina, *Journal of Neurophysiology* **53**:373–389.
- Sanes JR and Zipursky SL (2010) Design principles of insect and vertebrate visual systems, *Neuron* **66**:15–36.
- Santamaria F, Wils S, Schutter ED, and Augustine GJ (2006) Anomalous diffusion in purkinje cell dendrites caused by dendritic spines, *Neuron* **52**:635–648.
- Schein SJ (1988) Anatomy of macaque fovea and spatial densities of neurons in foveal representation, *Journal of comparative neurology* **269**:479–505.
- Schwartz G and Rieke F (2011) Perspectives on: information and coding in mammalian sensory physiology: nonlinear spatial encoding by retinal ganglion cells: when $1 + 1 \neq 2$, *J. Gen. Physiol.* **138**:283–290.
- Schwartz O, Pillow JW, Rust NC, and Simoncelli EP (2006) Spike-triggered neural characterization, *Journal of Vision* **6**:484–507.
- Segev R, Puchalla J, and Berry MJ (2006) Functional organization of ganglion cells in the salamander retina, *Journal of Neurophysiology* **95**:2277–2292.
- Sestokas AK, Lehmkuhle S, and Kratz KE (1987) Visual latency of ganglion x- and y-cells: a comparison with geniculate x- and y-cells, *Vision Research* **27**:1399–1408.
- Shams L, Kamitani Y, and Shimojo S (2000) Illusions. what you see is what you hear, *Nature* **408**:788.
- Shapley RM and Enroth-Cugell C (1984) Visual adaptation and retinal gain controls, *Prog. Retinal. Res.* **3**:263–346.
- Shapley RM and Victor JD (1978) The effect of contrast on the transfer properties of cat retinal ganglion cells, *Journal of Physiology* **285**:275–298.
- Shapley RM and Victor JD (1979) Nonlinear spatial summation and the contrast gain control of cat retinal ganglion cells, *Journal of Physiology* **290**:141–161.
- Sharpe LT and Stockman A (1999) Rod pathways: the importance of seeing nothing, *Trends in neurosciences* **22**:497–504.

- Sherry DM, Bui DD, and Degrip WJ (1998) Identification and distribution of photoreceptor subtypes in the neotenic tiger salamander retina, *Visual Neuroscience* **15**:1175–1187.
- Singer JH (2007) Multivesicular release and saturation of glutamatergic signalling at retinal ribbon synapses, *J. Physiol. (Lond.)* **580**:23–29.
- Singer JH and Diamond JS (2006) Vesicle depletion and synaptic depression at a mammalian ribbon synapse, *Journal of Neurophysiology* **95**:3191–3198.
- Slaughter MM and Miller RF (1981) 2-amino-4-phosphonobutyric acid: a new pharmacological tool for retina research, *Science* **211**:182–185.
- Smirnakis SM, Berry MJ, Warland DK, Bialek W, and Meister M (1997) Adaptation of retinal processing to image contrast and spatial scale, *Nature* **386**:69–73.
- Strowbridge BW (2009) Role of cortical feedback in regulating inhibitory microcircuits, *Annals of the New York Academy of Sciences* **1170**:270–274.
- Sun QQ, Huguenard JR, and Prince DA (2006) Barrel cortex microcircuits: thalamocortical feedforward inhibition in spiny stellate cells is mediated by a small number of fast-spiking interneurons, *Journal of Neuroscience* **26**:1219–1230.
- Takahashi S and Sakurai Y (2005) Real-time and automatic sorting of multi-neuronal activity for sub-millisecond interactions in vivo, *Neuroscience* **134**:301–315.
- Thibos LN and Werblin FS (1978) The response properties of the steady antagonistic surround in the mudpuppy retina, *Journal of physiology* **278**:79–99.
- Towe AL and Harding GW (1970) Extracellular microelectrode sampling bias, *Experimental Neurology* **29**:366–381.
- Tranchina D, Gordon J, Shapley R, and Toyoda J (1981) Linear information processing in the retina: a study of horizontal cell responses, *Proc. Natl. Acad. Sci. USA* **78**:6540–6542.
- Tsodyks MV and Markram H (1997) The neural code between neocortical pyramidal neurons depends on neurotransmitter release probability, *Proc. Natl. Acad. Sci. USA* **94**:719–723.
- Victor JD (1988) The dynamics of the cat retinal y cell subunit, *Journal of Physiology* **405**:289–320.
- Victor JD and Shapley RM (1979) The nonlinear pathway of y ganglion cells in the cat retina, *The Journal of General Physiology* **74**:671–689.

- Victor JD and Shapley RM (1987) The dynamics of the cat retinal x cell centre, *Journal of Physiology* **386**:219–246.
- Warland DK, Reinagel P, and Meister M (1997) Decoding visual information from a population of retinal ganglion cells, *Journal of Neurophysiology* **78**:2336–2350.
- Watkins S, Shams L, Josephs O, and Rees G (2007) Activity in human v1 follows multisensory perception, *NeuroImage* **37**:572–578.
- Watson AB, Barlow HB, and Robson JG (1983) What does the eye see best, *Nature* **302**:419–422.
- Weick M and Demb JB (2011) Delayed-rectifier K channels contribute to contrast adaptation in mammalian retinal ganglion cells, *Neuron* **71**:166–179.
- Werblin FS (1972) Lateral interactions at inner plexiform layer of vertebrate retina: antagonistic responses to change, *Science* **175**:1008–1010.
- Werblin FS (1974) Control of retinal sensitivity. ii. lateral interactions at the outer plexiform layer, *Journal of general physiology* **63**:62–87.
- Werblin FS (2010) Six different roles for crossover inhibition in the retina: correcting the nonlinearities of synaptic transmission, *Visual Neuroscience* **27**:1–8.
- Werblin FS and Dowling JE (1969) Organization of the retina of the mudpuppy, *necturus maculosus*. ii. intracellular recording, *Journal of Neurophysiology* **32**:339–355.
- Wässle H (2004) Parallel processing in the mammalian retina, *Nature Reviews. Neuroscience* **5**:747–757.
- Wu SM (1991) Input-output relations of the feedback synapse between horizontal cells and cones in the tiger salamander retina, *Journal of Neurophysiology* **65**:1197–1206.
- Wu SM (1994) Synaptic transmission in the outer retina, *Annu. Rev. Physiol.* **56**:141–168.
- Wu SM (2010) Synaptic organization of the vertebrate retina: general principles and species-specific variations: the Friedenwald lecture, *Invest. Ophthalmol. Vis. Sci.* **51**:1263–1274.
- Wu SM, Gao F, and Maple BR (2000) Functional architecture of synapses in the inner retina: segregation of visual signals by stratification of bipolar cell axon terminals, *Journal of Neuroscience* **20**:4462–4470.
- Yang XL and Wu SM (1997) Response sensitivity and voltage gain of the rod- and cone-bipolar cell synapses in dark-adapted tiger salamander retina, *Journal of Neurophysiology* **78**:2662–2673.

Zaghloul KA, Boahen K, and Demb JB (2005) Contrast adaptation in subthreshold and spiking responses of mammalian y-type retinal ganglion cells, *Journal of Neuroscience* **25**:860–868.

Zaghloul KA, Manookin MB, Borghuis BG, Boahen K, and Demb JB (2007) Functional circuitry for peripheral suppression in mammalian y-type retinal ganglion cells, *Journal of Neurophysiology* **97**:4327–4340.

Zhang AJ and Wu SM (2009) Receptive fields of retinal bipolar cells are mediated by heterogeneous synaptic circuitry, *Journal of Neuroscience* **29**:789–797.

FIGURE ACKNOWLEDGMENTS

Figure 1.1 reprinted by permission from Macmillan Publishers Ltd: Nature Reviews. Neuroscience, Martinez-Conde et al. (2004), copyright 2011.

Figure 1.2 reprinted by permission from Macmillan Publishers Ltd: Nature Reviews. Neuroscience, Wässle (2004), copyright 2011.

Figure 1.3 reprinted by permission from Elsevier: Trends in Neurosciences, Wässle (2004), copyright 2011.

Figure 1.4 reprinted from the Journal of Neurophysiology, Zaghloul et al. (2007), no permission required.